2014

A STUDY OF THE LITHIUM IONIC CONDUCTOR $Li_5La_3Ta_2O_{12}$: FROM SYNTHESIS THROUGH MATERIALS AND TRANSPORT CHARACTERIZATION

Brian M. Ray
University of Kentucky, brayky@gmail.com

STUDENT AGREEMENT:

I represent that my thesis or dissertation and abstract are my original work. Proper attribution has been given to all outside sources. I understand that I am solely responsible for obtaining any needed copyright permissions. I have obtained needed written permission statement(s) from the owner(s) of each third-party copyrighted matter to be included in my work, allowing electronic distribution (if such use is not permitted by the fair use doctrine) which will be submitted to UKnowledge as Additional File.

I hereby grant to The University of Kentucky and its agents the irrevocable, non-exclusive, and royalty-free license to archive and make accessible my work in whole or in part in all forms of media, now or hereafter known. I agree that the document mentioned above may be made available immediately for worldwide access unless an embargo applies.

I retain all other ownership rights to the copyright of my work. I also retain the right to use in future works (such as articles or books) all or part of my work. I understand that I am free to register the copyright to my work.

REVIEW, APPROVAL AND ACCEPTANCE

The document mentioned above has been reviewed and accepted by the student's advisor, on behalf of the advisory committee, and by the Director of Graduate Studies (DGS), on behalf of the program; we verify that this is the final, approved version of the student's thesis including all changes required by the advisory committee. The undersigned agree to abide by the statements above.

Brian M. Ray, Student

Dr. Joe Brill, Major Professor

Dr. Tim Gorringe, Director of Graduate Studies

A STUDY OF THE LITHIUM IONIC CONDUCTOR $Li_5La_3Ta_2O_{12}$: FROM SYNTHESIS THROUGH MATERIALS AND TRANSPORT CHARACTERIZATION

DISSERTATION

A dissertation submitted in partial
fulfillment of the requirements for
the degree of Doctor of Philosophy
in the College of Arts and Sciences
at the University of Kentucky

By
Brian M. Ray
Lexington, Kentucky

Director: Dr. Joe Brill, Professor of Physics
Lexington, Kentucky 2014

ABSTRACT OF DISSERTATION

A STUDY OF THE LITHIUM IONIC CONDUCTOR $Li_5La_3Ta_2O_{12}$: FROM SYNTHESIS THROUGH MATERIALS AND TRANSPORT CHARACTERIZATION

The ionic conductivity of the lithium ionic conductor, $Li_5La_3Ta_2O_{12}$, is studied in an attempt to better understand the intrinsic bulk ionic conductivity and extrinsic sample dependent contributions to the ionic conductivity, such as grain boundary effects and the electrode-electrolyte interface. To characterize the material, traditional AC impedance spectroscopy studies were performed as well novel in-situ nanoscale transport measurements. To perform the nanoscale measurements, higher quality samples were required and new synthesis techniques developed. The results of these new synthesis techniques was samples with higher densities, up to 96% of theoretical, and slightly higher room temperature ionic conductivity, $2x10^{-5}$ S/cm. By combining the AC impedance spectroscopy results and in-situ nanoscale transport measurements from this study and prior reported results, as well as introducing models traditionally used to analyze supercapacitor systems, a new interpretation of the features seen in the AC impedance spectroscopy studies is presented. This new interpretation challenges the presence of Warburg Diffusion at low frequencies and the offers a new interpretation for the features that have been traditionally associated with grain boundary effects.

KEYWORDS: lithium, garnet, solid electrolyte, solid-state battery, ionic conductivity

Author's signature: Brian M. Ray

Date: May 5, 2014

A STUDY OF THE LITHIUM IONIC CONDUCTOR $Li_5La_3Ta_2O_{12}$: FROM SYNTHESIS THROUGH MATERIALS AND TRANSPORT CHARACTERIZATION

By
Brian M. Ray

Director of Dissertation: Joe Brill

Director of Graduate Studies: Tim Gorringe

Date: May 5, 2014

ACKNOWLEDGMENTS

First, I would like to thank the Department of Physics and Astronomy at the University of Kentucky for support as a teaching assistant and with travel support for research. I also wish to recognize the support of the members of my committee. In particular, Dr. YT Cheng for his immense expertise, which was invaluable, Dr. Rich Eitel for his support during the difficult task of synthesizing the material being studied here, and Dr. Joe Brill, for his mentorship in teaching and support in pursuing interdisciplinary research. Additionally, I acknowledge the support of two grants that made this research possible. The Center for Advanced Materials (CAM) provided funding via National Science Foundation Grant EPS-0814194. The Center for Nano-Materials Science (CNMS) at ORNL provided user time via User Facility Grant CNMS2012-0254. Finally, I would like to acknowledge the most significant support I received int his long process. I would like to thank my family. The support from Carrie and the inspiration from Eliot helped me to finish my work here.

TABLE OF CONTENTS

LIST OF TABLES

LIST OF FIGURES

1. Introduction

The challenges of energy and pollution play a significant role in today's society. This has led to increased attention in electric vehicles and variable renewable energy sources, such as wind, solar, and tidal, that require a means of storing the energy they generate to balance their generating capabilities with demand. Electric vehicles and variable renewable energy generation coupled with the increase in portable consumer electronics have created a need for efficient, safe, and reliable means of storing energy. Storing energy within electrochemical systems, such as a batteries, fuel cells, and supercapacitors, is one solution to the energy storage needs while addressing the concerns raised by pollution.[1]

Rechargeable lithium batteries represent one particular electrochemical energy storage system that have become ubiquitous in portable consumer electronics since their beginnings in research labs in the 1970s and their commercial introduction in 1991.[2] There have been improvements to them since their initial commercial introduction and some recent limited scale use with electric and hybrid vehicles, but they still do not meet the minimum specifications considered necessary for widespread adoption in the electric vehicle market.[3]

Solid state batteries aim to address the current shortcomings with the present generation of commercially available rechargeable lithium batteries in several key areas: increased specific energy density, lower cost per unit of energy stored, improved reliability and safety. A key component of a solid state battery design is a solid electrolyte.[4] To provide perspective and an appreciation for the promises of solid state batteries, a background of rechargeable lithium batteries is presented in chapter 2.

The focus of the research presented here, in chapters 5, 6 and 7, is to describe the ionic conductivity of one particular solid electrolyte from the garnet class, $Li_5La_3Ta_2O_{12}$ synthesized as a polycrystalline ceramic. This research, conducted over the course of four years, was done in laboratories at the University of Kentucky, Oak Ridge National Lab's Center for Nanophase Material Science, and at Lexmark International.

Lithium containing garnet ceramics were first reported as lithium ionic conductors in 2003, and are considered an auspicious class of lithium ionic conducting solid electrolytes.[5] The generic formula for these materials is $Li_5A_3B_2O_{12}$where the A site is normally lanthanum and the B site is pentavalent, and in the initial findings was niobium or tantalum. The promise of this class of lithium ionic conductors came not only from their relatively high ionic conductivities versus other known solid electrolytes, but also their thermal and chemical stabilities in conditions that would be encountered during the operation of rechargeable lithium battery. Since their initial discovery, this class of solid electrolytes has grown significantly with many chemical substitutions attempted, and, in particular, aliovalent substitutions on the A and B sites to increase the amount of lithium per unit formula.[5-11] Currently, the most promising candidates in this class are based on $Li_7La_3Zr_2O_{12}$.[10] Aliovalent doping of the quadravalent zirconium with pentavelent niobium or tantalum or hexavalent tellurium to fine tune the amount of lithium and lattice parameters have reported room temperature ionic conductivity on the order of 10^{-3}

S/cm.[10,11] An basic overview of the garnet class of solid lithium ionic conductors is found is chapter 3. This includes an overview of their discovery, atomic substitutions that have been tried, a summary of reported results, as well as a some prior theoretical calculations used to explain the method by which lithium ions move through the crystal lattice.

Identifying the ionic contributions to total conductivity is challenging, and a historical perspective on how this has been achieved is presented in chapter 4. This is done to help illustrate, both, the difficulty in measuring the ionic conductivity and to illuminate past experimental procedures, which may once again find relevance with new laboratory equipment and techniques.

Currently, the primary experimental method used to characterize the lithium ionic conductivity is AC impedance spectroscopy with ionically blocking electrodes.[12-15] One of the biggest challenges in determining the ionic conductivity of a sample is interpreting the impedance spectroscopy results. The common technique used today, and the one used in this research, is equating the AC impedance spectroscopy response of a system with an equivalent circuit. A background on this analysis technique and the modelling of equivalent circuits is found in chapter 5. This method of analyzing the ionic conductivity of samples is similar to methods used to characterize supercapacitors. [16-19] Interpretations of the results of this work require a basic understanding of supercapacitors, and, in particular, the double-layer capacitive aspect of supercapacitors and the multi-pore models used to explain and model it. An overview of these topics can also be found in chapter 5. Additionally, some prior results have claimed the existence of Warburg Diffusion based on the results of AC impedance spectroscopy and a background on the subject is also included in chapter 5.

Other experiments that probe the mobility of lithium in solid electrolytes have recently been performed on the nanoscale, and these techniques are used in this research as well to compliment the AC impedance spectroscopy studies.[20-22] The techniques employed and results of previous results of these experiments are included in chapter 5.

The nanoscale experiments required high quality samples that could withstand the sample preparation involved to achieve the desired surface smoothness in order to undergo these experiments. Newer synthesis techniques, similar to that reported recently, were developed to achieve higher density samples to allow for the surface preparation needed for nanoscale measurements of lithium transport.[23,24] The polycrystalline $Li_5La_3Ta_2O_{12}$ samples were synthesized using solid state techniques. The synthesis techniques, sample preparation techniques, as well as material composition characterizations are described in chapter 6. This part of the research represented the most time and resource intensive part of the results presented here. The primary experimental procedures used in this research to characterize the composition of the samples were X-Ray Diffraction Spectroscopy (XRD), X-Ray Photoemission Spectroscopy (XPS), and Scanning electron Microscopy (SEM).

The response of the samples to AC impedance spectroscopy is presented in chapter 7. The interpretation of the impedance spectroscopy results is one area where some inherent

ambiguity can, and usually does, exist. The in-situ AFM results are used to compliment the impedance spectroscopy results and help eliminate some ambiguity in the interpretation of the response of the system, and they are also presented in chapter 7.

Conclusions are drawn from the results presented here in chapter 8. Additionally, an outline of some future directions this research could lead is found in chapter 8. One unfortunate aspect to this research was the low yield of the samples used. That, coupled with time and resource limitations, has left room for future studies to be performed within the context of this research. There are also some remaining questions outside of the scope of this research that remain to be answered fully. These questions as well as potential ways of addressing them are also laid out in chapter 8. This work concludes with a list of references cited.

2.0 Rechargeable Lithium Batteries and Types of Electrolytes

Commercially available rechargeable lithium batteries have not made significant progress since their commercial introduction in 1991.[25] Today's batteries remain very similar to what was found over 20 years ago, and the active materials that control the electrochemistry in the battery have changed very little. The anode is still graphite. The cathode has gone from what was originally lithium cobalt oxide to some combination of lithium cobalt oxide, lithium nickel oxide, or lithium manganese oxide, which have similar electrochemical properties. The electrolyte is still primarily the lithium salt, lithium hexaflourophosphate, dissolved in an organic solution. At the time of presenting this research, 2014, one of the current top of the line rechargeable lithium batteries is the Panasonic NRC 18650A, which is used in many applications, included the battery packs in Tesla automobiles. These batteries still use a carbon anode and a lithium nickel oxide cathode with a liquid electrolyte consisting of lithium salts dissolved in an organic solvent. Currently, the rechargeable lithium battery industry is starting to transition to silicon anodes, which could bring initial increases in energy storage of approximately 30%, and potentially more.[1,25]

In order to store even more energy in the same size or weight package, reduce costs, or improve safety, new designs are required. One promising area of research is in the use of solid state materials as the electrolyte, replacing the liquid lithium hexaflourophosphate solutions along with the phase separating membranes.[2] There are several benefits and some drawbacks to such a design for a rechargeable lithium battery. To fully understand the motivation and tradeoffs for using a solid electrolyte it is important to first go through an overview on the operation of rechargeable lithium battery and understand its major components and the different types of electrolytes.

As a point of reference, rechargeable lithium battery is used throughout to denote any form of battery for which lithium ions are the means of charge conveyance through the electrolyte, lithium ions are an integral part of each of the half cell reactions at either electrode, and that the electrochemistry can be reversed by applying a sufficient bias to the two electrodes. More commonly used terminology is avoided due to the commercial connotations of certain terms. Lithium ion battery is a term first used by Sony and generally refers to a group of specific constituents in the battery. Lithium polymer battery is another term that has come to mean one very specific configuration since its commercialization.

This is intended to only be a brief overview of the operation of a rechargeable lithium battery and each class of electrolyte. Only some of the more prevalent or promising candidates of each class will be considered here and are used to highlight specific properties inherent to most members of that class. The study of electrolytes, particularly within the context of rechargeable lithium batteries, is quite active, with well over 1000 papers per year according search inquiries on Web of Science. Reviews of the literature are common, but can become dated even when they are only several years old.

Additionally, the field of study of electrolytes is broad, even when focusing on only solid electrolytes within the context of rechargeable lithium batteries. The researchers come from different backgrounds and fields and there can be some disagreement between papers on the properties of the same material. This can be due to variations in the samples tested, which are generally not ideal single crystals, as well as different interpretations of the results, which generally have inherent ambiguities. The results of the research presented later in Chapters 5, 6, and 7 are not immune to these problems as well, and the causes of these disparities are addressed in detail in those chapters as well as the concluding remarks of Chapter 8.

2.1 Basic Overview of the Principles of a Rechargeable Lithium Battery

There are three major components to a rechargeable lithium battery (and all batteries in general). There are the two electrodes, the anode and the cathode, as well as the electrolyte/separator. The anode is the negative electrode, the cathode is the positive electrode, and the electrolyte/separator is what physically separates, but electrochemically connects the two electrodes inside the battery. When a battery is connected to a circuit and is discharging, electrons are leaving the anode, flowing through the external circuit, and returning to the battery at the cathode. When a battery is charging, an external voltage source is now part of the circuit. When a sufficient voltage is applied to drive the electrons, they leave the cathode, flow through the external circuit, and return to the battery at the anode.

A battery is more complicated than just storing electrons by themselves at one electrode and then allowing them to flow to another. Such a simplistic setup is just a traditional dielectric capacitor, which stores very little energy, does not maintain a roughly constant voltage, and will discharge all of its energy quite rapidly if allowed.

A battery works by using electrochemical reactions at either electrode. In a rechargeable lithium battery, the electrochemical reactions allow each electron to be stored with a lithium ion in an electrode when it is not needed, and then free it to flow through the external circuit when it is needed. To maintain charge neutrality, each electron is stored with a lithium ion, either recombined as atomic lithium, or physically separated, but still treated as together from an electrochemical standpoint, even if the electron is not stored locally with the lithium ion. The lithium is stored in the electrodes of a rechargeable lithium battery by being inserted between layers of a host material, as is the case for atomic lithium, or reacting with a host material to form a new phase with a different lithium concentration, which is the case for ionic lithium. In the former case, the electron is stored locally with the lithium, and can be thought of as neutral atomic lithium. In the latter, the electron is with another atomic species, usually a 3-d transition metal within an oxide material, and the valence state of the transition metal has changed while the lithium is still ionic in nature. There is one additional case where the lithium is stored as neutral atomic lithium and that is when lithium metal is the anode.

There is a cost associated with adding a lithium atom into the host material (and a payment or negative cost with removing one). As more lithium is added into the host material, it becomes costlier to add more. Additionally, it is not just the amount of lithium already present that

determines the cost to add more. The rate that lithium atoms are added to or removed from the host material is also important. It is easier to add or remove lithium slowly. As the rate increases, the lithium doesn't have a chance to diffuse evenly through the electrode and locally there can be higher or lower concentrations. The cost of adding or removing lithium is now governed by the local concentrations, not the overall concentration of lithium. The cost of adding or removing lithium is quantified as the electrochemical potential, and is commonly expressed in units of volts. The electrochemical potential for lithium is higher at the anode than the cathode. This means than lithium would prefer to be in the cathode than the electrode. The difference in the electrochemical potentials of lithium at either electrode in a battery that is not connected in a circuit is called the open circuit potential of the battery and is what determines the voltage of the battery. This voltage will change as the state of charge or discharge of the battery changes.

When, in a rechargeable lithium battery connected to an external circuit, an electrical pathway exists for electrons to flow from the anode to the cathode and the electrochemical potentials of the two electrodes make such a flow favorable, then two electrochemical half-reactions will occur. One half-reaction involves a lithium ion leaving the anode host material and flowing into the electrolyte while simultaneously an electron leaves the anode and flows into the external circuit. The second half-reaction is at the cathode where a lithium ion leaves the electrolyte to flow into the cathode host material while simultaneously an electron leaves the external circuit and also flows into the cathode. Note that charge neutrality is maintained in the electrolyte as an ion flowed into it at the anode side and one left at the cathode side. This process will continue as long as there is an external circuit and until either the lithium is depleted at the anode or the cost of adding and removing lithium becomes unfavorable and the electrochemical potentials of the two electrodes become equal. The electrochemical reactions can then be reversed by applying a sufficient external voltage across the two electrodes such as to raise the electrochemical potential of lithium at the cathode above that at the anode and thus drive the electrons and lithium ions back to the anode.

2.2 Types of Electrolytes

With this quite simple overview of the operation of a rechargeable lithium battery, it should be easy to see the key requirements of any electrolyte. First, it must be able to conduct lithium ions. Second, it must not allow electrons to flow across it. If it did, there would be no need for an external circuit, there already is an internal electrical pathway for the electrons to get between the electrodes, and the battery would not be able to store any energy. Third, the electrolyte must prevent diffusion of atomic lithium between electrodes, which is akin to allowing ions and electrons to simultaneously flow. In addition to the aforementioned three main requirements of an electrolyte, there are other secondary requirements. Some electrolytes do not meet all of these additional requirements, but a functional battery can be designed around limitations in these areas. One is that the electrolyte should be chemically inert in the operating environment of the battery. Another is that the electrolyte should prevent electrically conductive contact, shorting, between the electrodes.

There are three main classes of electrolytes for rechargeable lithium batteries; liquid, polymer, and solid. There are a variety of electrolytes either being used, or being considered for use in each category. This overview will only touch upon a few key features and members of each class.

2.2.1 Liquid Electrolytes

Liquid electrolytes have many inherent advantages to other electrolytes. One is that, for the most part, they have a higher lithium ionic conductivity than their counterparts. Another big advantage is that there is good liquid to solid contact between the electrolyte and an electrode.[1,2] These two main advantages have allowed liquid electrolytes to remain the most common electrolyte in today's commercially available rechargeable lithium batteries, despite some drawbacks. One is that many of the liquid electrolytes used are quite toxic and require extra care in handling, manufacturing, and packaging. Another is the stability of the liquid electrolytes. When heated, the liquid electrolytes can vent gasses that cause pressure to build within the sealed batteries. Also worth noting is the flammability of the organic solvents used to dissolve the ionic salts that form the basis of most liquid electrolytes.

Amongst the liquid electrolytes, lithium hexaflourophosphate is the by far the most prevalent.[1] This electrolyte is an ionic salt solution in an organic solvent. Lithium hexaflourophosphate solutions are reactive with lithium and other materials in some environments. It depends on the host material used as well as the temperature and other parameters. Fortunately, some of the reactions can yield byproducts which create coatings around the electrodes to prevent further reactions. This multi-phase region where these reaction products exist is known as the solid electrolyte interphase. Additives are used to control these reactions. Additionally, lithium hexaflourophosphate solutions are liquid, so they do not prevent the two electrodes from touching. That is solved by placing a porous separator between the electrodes.

2.2.2 Polymer Electrolytes

Another class of electrolytes used in rechargeable lithium batteries is a polymer electrolyte. Polymer electrolytes can be thought of as an intermediary between a liquid electrolyte and a solid electrolyte. They still retain the mechanical properties of a solid, but they have lithium salts solvated into them to provide the lithium ionic conductivity necessary to function as a good electrolyte. To improve ionic conductivity, the polymer may also have the entire liquid electrolyte including the organic solvent with the lithium salts added to it, creating a polymer gel.[26]

The polymer gel electrolytes have been commercially available since at least 1997 and are marketed as lithium polymer batteries.[1,2] Their design uses the same lithium salts, primarily lithium hexaflourophosphate, as the liquid electrolyte, as well as organic solvents incorporated into a polymer matrix. The advantages of this design are that there is no need for a separator

between the electrodes and the solid form of the electrolyte allows for the use of lithium metal as the anode.[26]

In regards to maximizing the specific capacity of the battery, lithium is the ideal anode to use. To reinforce that the anode is entirely lithium, not lithium moving into a host material, the terms metallic lithium, lithium metal, and bulk lithium are commonly used, with the term lithium metal used here. Lithium metal as an anode is the one special case where a host material is not needed in the electrode. The electrochemical potential of lithium in lithium metal remains constant, regardless of the amount of lithium present, or the rate it is being inserted or withdrawn. The entire electrode is lithium, and there are no variances in lithium concentration. Additionally, the electrochemical potential of lithium metal is higher than any other electrode material, which allows for the greatest potential difference between other electrodes. If a material had a higher electrochemical potential for lithium than lithium metal, the lithium in that material would phase separate to then be in the more favorable lithium metal phase. This would preclude such a material from being an electrode, because it wouldn't function as a host material to store lithium.

Lithium metal anodes have been shown to not work with current liquid electrolytes, which has caused increased attention to other types of electrolytes in order to utilize the benefits of a lithium metal anode.[27] There are drawbacks to using lithium metal as the anode. Lithium traditionally does not form a smooth surface when it is deposited. Instead, it has a tendency to form dendrites, which are branch like projections. These dendrites can grow as lithium is being deposited at the anode and bore through the electrolyte to reach the cathode material. Should that occur, the battery will rapidly discharge, with the possibility of catastrophic overheating resulting.[28]

An intrinsic drawback to using a gel polymer is the thermal stability of the polymer composite. The electrolyte has been shown to begin to breakdown at elevated temperatures, which can occur if the battery is short circuited. When this happens the solid polymer will start to produce gases, raising the pressure inside the sealed battery cell. Additionally, as the polymer degrades, the potential for lithium dendrites to internally short the battery increases, which compounds the problem. Overheating to the point of combustion of the polymer material has been reported. This problem is addressed with circuitry that limits the operating current and voltage of the battery.

Another drawback to the use of gel polymer electrolytes is that there is a solid-solid interface between the electrolyte and the cathode. A good solid-solid interface is difficult to achieve, and care in the design is taken to ensure the battery has a good initial contact between the electrolyte and the cathode. As the cathode swells and contracts with lithium insertion and withdrawal, the quality of the interface degrades. Circuitry is used that limits the electrochemical potential difference between the two electrodes. This prevents too much lithium from being inserted into the cathode host material, which, in turn, prevents the cathode material from swelling too much, thus preserving the good solid-solid interface.[26]

Finally, it is worth mentioning again that the primary lithium salt used in the gel polymer electrolytes, lithium hexaflourophosphate, is the same one used in the liquid electrolytes, and it is considered toxic.

2.2.3 Solid Electrolytes

Solid electrolytes represent the third class of electrolytes in rechargeable lithium batteries. Limited commercial activity exists with solid electrolytes, primarily with research, and as of the spring of 2014, no mass commercial rechargeable lithium batteries use a solid electrolyte. There are two main benefits to using solid electrolytes. One is the wider range of electrode materials available as their use would eliminate the instability of certain electrode materials with liquid electrolytes. The second is the possibility of designing a solid state thin film battery which could significantly reduce manufacturing challenges.

The solid electrolytes considered here are either amorphous or polycrystalline, both primarily synthesized as ceramics. Other means of synthesis have been employed to yield thin films and single crystals grown via flux methods or with deposition techniques as epitaxial grown crystals. The ionic conductivity is promising in some of the amorphous electrolytes, but they are not stable with lithium metal.[26] The same is true for solid polycrystalline electrolytes within the perovskite crystal class.[26] The garnet class represents one promising class that is stable with lithium metal and exhibits relatively high ionic conductivity for a solid electrolyte. This class of solid electrolytes is the focus of the research presented here and is detailed further in chapter 3.[29]

Quite recently, a new class of sulfide solid electrolytes has been showing significant promise.[30-32] This class includes both amorphous and crystalline electrolytes, as well as some combinations of both. This includes $Li_3P_7S_{11}$, $Li_{10}GeP_2S_{12}$, and several other sulfur containing chemistries.[31]

3. Garnet Class of Solid Lithium Ionic Conducting Electrolytes

The samples that were studied in this research are closely related to and thus are considered part of the garnet crystal group. They are often referred to as garnet lithium ionic conductors or garnet solid electrolytes, or simply lithium garnets. The classic garnet has the general formula $A_3B_2C_3O_{12}$, where the A site is occupied by a divalent atom, the B site is occupied by a trivalent atom, and the C site is quadrivalent and is usually silicon. The crystal structure of the traditional garnets is body-centered cubic with 8 unit formula per unit cell.[29] Many possible atomic combinations exist within the classic garnet general formula, as well as many aliovalent substitutions that deviate from the garnet's general formula.

A solid electrolyte that conducts one ionic species must contain an appreciable concentration of that ion. This allows for high ionic conductivity as a hopping mechanism occurs. As the ion enters the electrolyte at one electrode, nearby ions react and migrate away, and so on for the next ones, until an ion leaves the electrolyte at the opposite electrode. To achieve a high enough concentration of lithium to maximize ionic conductivity, the mobile ionic species should be part of the general composition of the crystal structure, and not simply a dopant added. Therefore, aliovalent substitutions must be used to accommodate the monovalent lithium within the garnet class of crystals.

3.1 Initial Discovery and Original Compositions

The crystal structure of materials belonging to the garnet class of lithium ionic conducting solid electrolytes was first reported in 1988 with $Li_5La_3Ta_2O_{12}$ and $Li_5La_3Nb_2O_{12}$, and the ionic conductivity was first reported in 2003.[5,33] This class of materials has the general formula of $Li_5B_2C_3O_{12}$ and in this configuration the B site is pentavalent instead of trivalent, the C site is trivalent instead of quadrivalent, and the number of A sites increased from 3 divalent atoms to 5 monovalent lithium atoms.[29] These two materials showed high ionic conductivity that was comparable to other solid electrolytes, while also showing high chemical stability with lithium and thermal stability. Soon, many substitutions on the B and C sites, including aliovalent substitutions with the number of lithium atoms adjusted accordingly, were attempted with mixed results. Some showed remarkably higher (by an order of magnitude) improvement in the ionic conductivity, while other substitutions suppressed the ionic conductivity.

Table 3.1 below summarizes the reported ionic conductivities of a few of more successful attempted substitutions by March of 2014. There are on average 20 papers per year being published on this class of ionic conductors, many with novel substitutions. This is still an active area of research, and new compositions are being tried continuously. It should be noted that, with few exceptions, the samples generated and tested are polycrystalline ceramic samples, and there is some sample variation and fluctuation in the reported ionic conductivities between different research groups. Additionally, it should be noted, and is further expanded upon in chapters 5 and 7, that there can be some ambiguity in interpreting the conductivity response of the system and thus assigning an intrinsic ionic conductivity to the sample being tested.

Table 3.1: Summarized Results for a few of the reported Lithium ionic Conductors in the Garnet Crystal Class

Unit Formula (* means concentration was adjusted)	Max Room Temperature Bulk Ionic Conductivity (10^{-5} S/cm)	Activation Energy Associated with Max Bulk Ionic Conductivity (ev)	Year	Lead Author	Reference
$Li_5La_3(Ta,Nb)_2O_{12}$	.1	.56	2003	Thangdurai	[5]
$Li_6BaLa_2Ta_2O_{12}$	4	.40	2005	Thangdurai	[34]
$Li_6BaLa_2Ta_2O_{12}$	7.4	.40	2007	Murugan	[8]
$Li_7La_3Zr_2O_{12}$	.2	.54	2009	Awaka	[35]
$Li_7La_3Zr_{2*}O_{12}$	96	.29	2011	Murugan	[6]
$Li_{7*}La_3Zr_{2*}Nb_*O_{12}$	80	.30	2011	Ohta	[11]
$Li_{7*}La_3Zr_{2*}Ta_*O_{12}$	100	.35	2012	Li	[7]
$Li_{6.75}La_3Zr_{1.75}Ta_{.25}O_{12}$	74	.33	2012	Allen	[24]
$Li_{7*}La_3Zr_{2*}Ta_*O_{12}$	87	.22	2014	Li	[23]

Initially, there was some debate about the crystals structure with evidence being presented for both a cubic phase and a tetragonal phase.[5,6,8,11,24,29,34,35] More recent findings suggest that the high ionic conductivity is a result of the cubic phase, and that dopants can stabilize the structure in the cubic phase. [24,29] Conversely, other recent findings point towards a stable cubic phase.[29,36]

The orientation of the atoms in the cubic phase depends on the particular unit formula, and how many lithium atoms are present. Recent density functional theory calculations have provided good agreement with experiment and provide a glimpse into the lithium occupation and modes of conduction for different concentrations of lithium.[36] There are two different site the lithium atoms can occupy, a tetrahedrally coordinated site and an octahedrally coordinated site. There are 24 tetrahedral sites and 48 octahedral sites per unit cell, with 8 unit formula per unit cell. For low lithium concentration, the tetrahedral sites are preferentially occupied. For increasing lithium concentration, the octahedrally sites start to get occupied, and it is these lithium atoms that are thought to account for the ionic conductivity. For even higher lithium concentrations, the tetrahedral sites are no longer fully occupied, and the octahedral sites are preferentially occupied, resulting in higher lithium ionic conductivity.[36] Fig. 3.1 below from the density function theory calculations shows the different ionic conduction pathways for different lithium concentrations. The results shown in Fig 3.1 are in agreement with lithium coordination and relative occupancies found with neutron diffraction and NMR.[29]

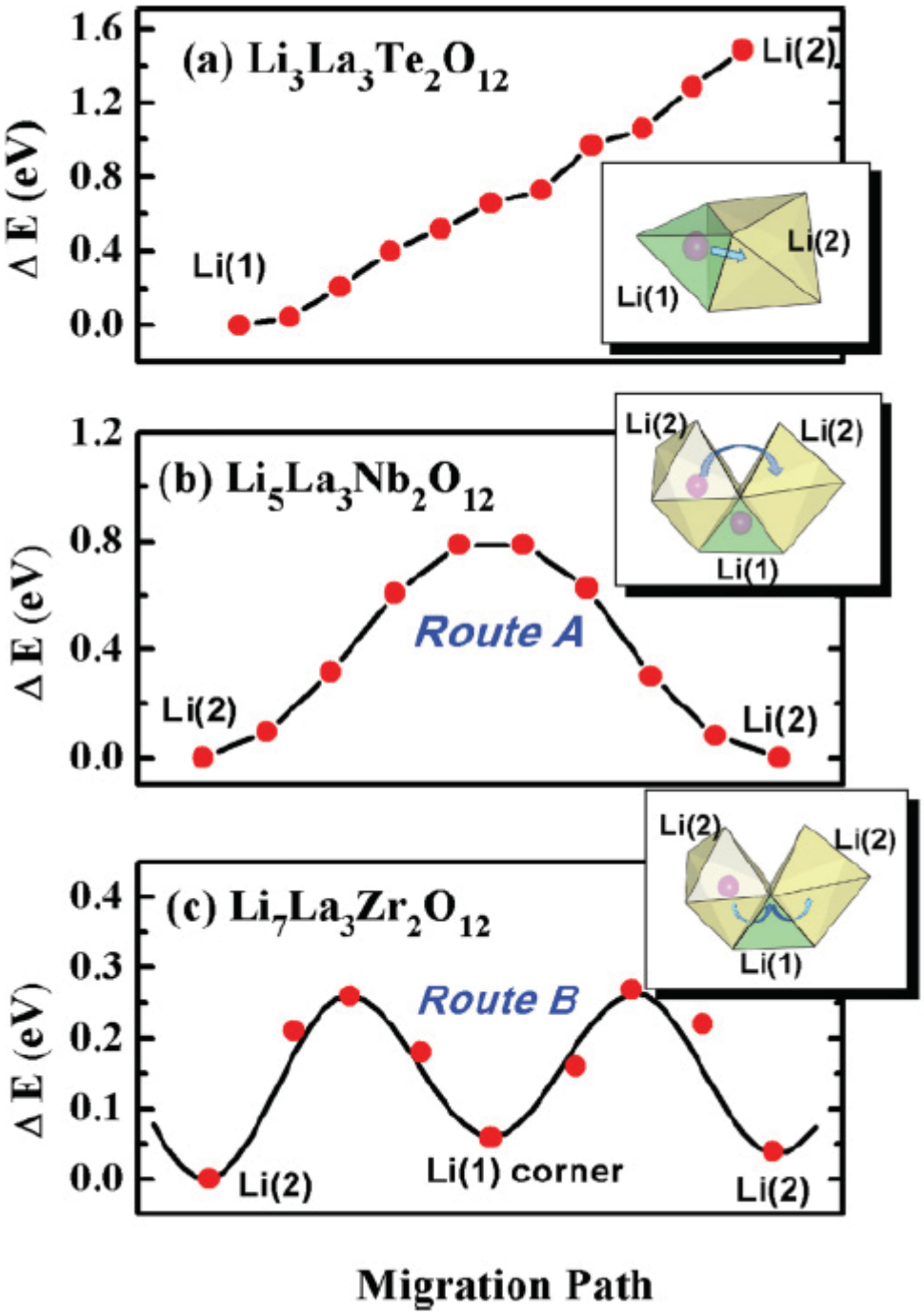

Figure 3.1: Migration pathways for Li ionic conduction for three different lithium concentrations, **a)**24 Li per unit cell all in the tetrahedral site, **b)** 40 Li per unit cell, with the tetrahedral site full occupied and the octahedral site 1/3 occupied, **c)** 56 Li per unit cell with the tetrahedral site ½ occupied and the octahedral site 5/6 occupied [36]

4.0 History of Measuring Ionic Conductivity

Michael Faraday pioneered the first reported studies of ionic conduction in the 1830s. Though he didn't realize it at the time, he discovered the first solid state ionic conductors, Ag_2S and PbF_2, when he found that their conductivity significantly increased as they were heated with a lamp.[37-39] The exponential increase in conductivity with increasing temperature that Faraday witnessed and described with quite remarkable prose is a hallmark of ionic conduction. Walther Nernst found the first practical application of an ionically conducting solid by exploiting that feature. In 1897 he developed a more efficient alternative to the carbon filament incandescent lamps by using yttria stabilized zirconia as the filament. These new lamps, which came to be known as Nernst lamps, had a short run of commercial appeal until they were replaced by the more efficient tungsten filament lamps.[39,40] The advantages of not needing the glass bulb to protect the filament were ultimately outweighed by the loss of efficiency inherent in preheating the ceramic filaments enough to allow for sufficient conductivity to then be capable of self-heating.

Quantitative measurements of the ionic conductivity of solid electrolytes eventually followed these initial discoveries and applications. The study of ionic conduction therefore has a long history. This review is not intended to be an authoritative study of the field, but rather to illustrate some of the different techniques used to measure the ionic conductivity of solids. The aim is to present a background of the challenges inherent in studying the ionic conductivity of lithium in solids.

Some of the early pioneering work of note was done by Carl Tubandt in Germany from the early 1900s through 1930s. Tubandt examined the ionic conductivity of several metal halides using new experimental methods to measure the ionic and electronic contributions to conductivity. He achieved this by using electrodes that allowed the mobile ion(s) to enter and leave the sample – in essence a source and sink of ionic charge carriers. This allowed him to use simple DC measurements to find the total current that passed through the sample, and then to use the change in masses of the two electrodes to calculate the number of ions that transferred, and thus the ionic and electronic contributions to the total conductivity.[39,41]

As newer ionic conductors were identified with higher and higher values of ionic conductivity, research into measuring the Hall Effect for ionic motion started in the 1960s. Initially, these measurements were done at significantly elevated temperatures to exploit the Arrhenius nature of ionic conductivity. [41] Later, improved measurement techniques as well as ionic conductors with higher room temperature ionic conductivity allowed for these measurements to be extended into lower temperatures, eventually getting into room temperature measurements by the 1980s.[42-44] To date, no Hall Effect measurements have been reported for lithium ionic conductors, and the measurement technique has only rarely been extended to polycrystalline samples.[43]

The earlier work of Tubandt of characterizing bulk samples was carried on by Carl Wagner in the early 1930s and again in the 1950s. His focus switched to the thermodynamics of the fuels used

in the V2 rockets and later work for the American rocket programs in the build-up and immediate aftermath of World War II. Wagner's work was then carried on by Malcolm Hebb in the 1950s and the 1960s. Initially Wagner had developed a technique of using one electrode that was ionically blocking, and one that was reversible. By applying the correctly polarized DC bias, the ionic charge transport was blocked, but the electronic charge transport was not.[39,45-46] Hebb built upon this technique, by trying to correct for the compositional dependence of the ionic conductivity by blocking the electrons and using Tubandt's setup with reversible electrodes, thus creating a more uniform ionic concentration in the sample.[39,47] Their techniques are known today as the Hebb-Wagner polarization method, and are still used to this day, particularly with measuring the ionic transport in solid oxide fuel cell membranes.

One unfortunate drawback to the above techniques is the requirement to use electrodes that allow for the free transport of the mobile ionic species into and out of the electrode. Though the interface of the sample and electrodes was not trivial, this proved feasible for the early pioneering work described above where the silver halides were primarily studied and silver electrodes were applied. This has also proved manageable for working with oxygen ionic conductors common in solid oxide fuel cells. For work involving lithium as the mobile ionic species, the design and implementation of these experiments becomes significantly more problematic.

A solution to this problem is found by using AC impedance spectroscopy. Prior work with solid ionic conductors used AC voltage sources, though the experiments were usually run at around 500Hz to 1000Hz. Some frequency dependence was observed, but not well understood. The experiments would occasionally be run at higher frequencies to check for significant, usually greater than 10%, changes in the measured impedance of the samples. If significant changes were seldom encountered, then the ionic conductivity was reported.[48-50]

One of the first instances of using AC impedance spectroscopy to characterize ionic conductivity in electrochemical systems was in 1969 by James Bauerle.[12] This new techniques was made possible by the introduction of phase sensitive detection techniques in the 1960s and has proven to be a powerful technique for characterizing ionic transport since. This technique initially was used for oxygen conductors and was later extended to sodium ionic conductors, lithium ionic conductors, as well as many other systems.[13,14] An extension of the technique to simplify the study of ionic conductivity within the context of solid electrolytes was put forth in 1971 by D Raleigh.[15]

AC impedance spectroscopy helps address the problems of working with lithium electrodes as sources and sinks for the mobile ionic species or uneven compositions that result from DC measurements with ionically blocking electrodes. Unfortunately, it introduced new challenges. Chief amongst these was in equating the results of AC impedance spectroscopy with specific physical processes occurring in the samples being studied. This arises from an inherent ambiguity to the results, especially in regards to isolating the ionic conductivity from double-layer capacitive effects that result from the AC biases used. The work presented here addresses

these concerns and introduces a new measurement technique to address some of the ambiguity.

5. Measuring Ionic Transport

Two different methods were used in this research to characterize the ionic transport of solid electrolytes and backgrounds on the techniques are presented here with AC impedance spectroscopy in section 5.1 and in-situ nanoscale transport measurements in section 5.2. The material property of the solid electrolyte can then be characterized further once the bulk resistance associated with ionic conductivity is determined from AC impedance spectroscopy, and is outlined in section 5.3.

5.1 AC Impedance Spectroscopy

AC impedance spectroscopy is the most common way to characterize solid electrolytes today, and is the method used in all the ionic conductivity studies reviewed in section 3.2. It can be a powerful technique that reveals multiple transport related properties of the material being studied, but it is also quite complex.

The complexity of the technique stems from an inherent ambiguity in interpreting the results, which is done by comparing the response of the system being tested with equivalent circuit models. The equivalent circuit models can try to model different aspects of the systems response, and use different physical justifications for their underpinnings. Two commonly used equivalent circuit models used to interpret solid electrolyte systems as well as two models used to interpret the responses of supercapacitors are presented in section 5.1.3. To put the models into context, prior AC impedance spectroscopy results of solid electrolytes are presented in section 5.1.4, as well as additional circuit elements used and an extension of one of the supercapacitor equivalent circuits introduced previously. The equivalent circuit introduced in 5.1.4 and further extensions of it are the models that ultimately provided the best fits when analyzing the AC impedance spectroscopy responses of the solid electrolyte systems tested in this work and presented in Chapter 7.

5.1.1 Experimental Setup

The premise behind AC impedance spectroscopy is to modulate the frequency of a low amplitude sinusoidal voltage source varying with time and measure the response of the system at each frequency. For the purpose of the measurements done in this research, the system consists of the sample prepared with ionically blocking electrodes. The term ‘system’ is used here because the impedance spectroscopy response is determined not just by the sample, but by the electrodes used and the quality of the interface between the two. A typical, yet basic, two-probe experimental setup is shown in Fig. 5.1 below.

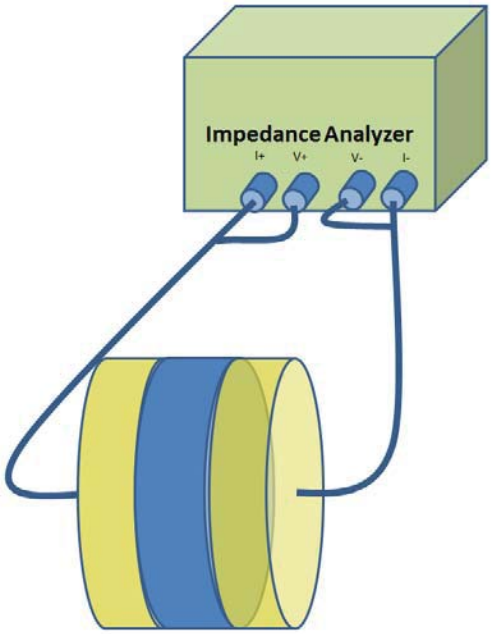

Figure 5.1: Schematic of 2-probe measurement technique commonly used for AC impedance spectroscopy on ceramic pellets

5.1.2 Double Layer Capacitance

Using ionically blocking electrodes to prevent diffusion and Faradaic charge transfer has been attempted before, but the significant dependence of the response of the system to the applied frequency was not well understood.[48-50] This frequency dependence is the result of the capacitance of electric double layers that build up at the sample-electrode interfaces, resulting in supercapacitance. A basic overview of capacitors and supercapacitors is presented here in order to introduce supercapacitors. Supercapacitors are of interest to this research in that a solid electrolyte with electrodes on either side can be viewed as a supercapacitor, and therefore models used in the analysis of supercapacitors become pertinent to interpreting some of the results of experiments involving solid electrolytes.

5.1.2.1 Capacitors

Capacitors are basic circuit elements and their response to an applied signal is characterized by a value known as the capacitance. The capacitance of an object is not an intrinsic property of a material, but rather it is a function the entire setup of a system. It is quite sensitive to the physical sizes, geometrical layout, and material properties of the different components of the system. The simplest system to consider would consist of two electrodes physically separated from each other such that there is no conductive pathway between them. If there exists a voltage difference between the two electrodes, then negative charge will accumulate on the electrode held at the lower voltage and an equal in magnitude positive charge will accumulate on the other electrode. The magnitude of the amount of charge present on an electrode is a

function of the applied voltage. For many systems, the geometry and separation distance of the electrodes, the non-conductive material separating the electrodes and the magnitude of the applied voltages are such that there is basically a linear relationship between the magnitude of the charge that accumulated on an electrode and the applied voltage. The ratio of the accumulated charge to the applied voltage is therefore constant, and is defined as the capacitance of the system. If the applied voltage is an alternating source with frequency, ω, this ratio is relatively constant over a wide range of frequencies. The limits to the frequency independent and linear with voltage behavior of the system are at high voltages where the separating material may start to breakdown and at high frequencies where the frequency of the applied voltage, ω, approaches the polarization response of the separating material.

A very basic solution for the capacitance of a simplified system is presented to help illustrate how a supercapacitor functions later. This simplified setup for a capacitor is two parallel conductive planar electrodes, separated by a non-conductive medium known as the dielectric. In the limit where the surface area, A, of an electrode is much larger than the distance, d, between them, the capacitance can to good approximation be expressed as equation 5.1 below, where ε is the dielectric constant of the separating material.

$$C = \frac{Q}{V} = \frac{\varepsilon A}{d} \quad \text{equation 5.1}$$

5.1.2.2 Supercapacitors and the Helmholtz Double Layer

The most basic form of a supercapacitor, known as a double layer capacitor, has a similar geometry to the basic capacitor described above. The only difference is that the dielectric is replaced with an ionically conductive electrolyte. An overly simplified picture of this system when connected to voltage source, shown in Fig. 5.2 below, would then have a layer of negative charge existing on the surface of one electrode adjacent to the electrolyte and a layer of positively charged ions an atomic layer away inside the electrolyte. The corresponding positive charge would be on the other electrode and a layer of negative ions an atomic distance away inside the electrolyte. The two layers of opposite charge that now exist on either side of an interface are referred to as a Helmholtz double layer, and the physical spacing between them is now on the atomic level and can be less than an angstrom. The increased capacitance of the supercapacitor is now evident by the significant reduction of the distance, d in the denominator of equation 5.2 above, that separates the two layers of charge.

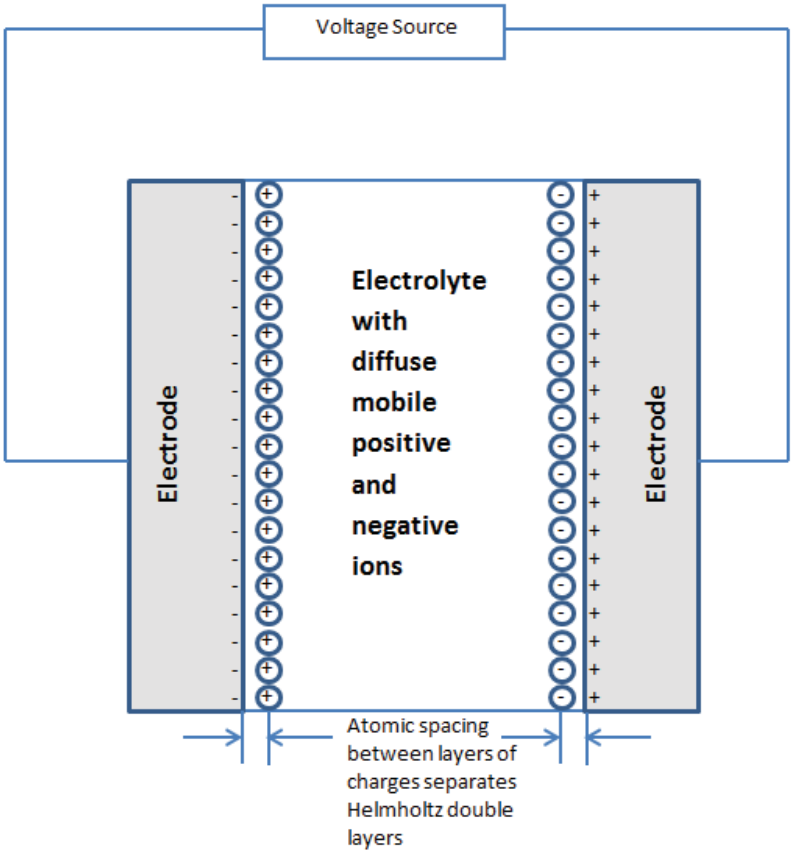

Figure 5.2: Schematic of Supercapacitor with Planar Electrodes

It should be noted that the capacitance described here is more complicated than the simplified picture present above. There is a nonlinear response to applied voltage as well as a diffuse region between the Helmholtz double layers that contributes to the capacitance as well. For the purposes of the research presented here though, the picture of the Helmholtz double layer as the primary source of capacitance, and the inversely proportional dependence of the capacitance on the average separation of the mobile ions or vacancies from the electrodes will suffice. More accurate models have been proposed by Gouy in 1910, Chapman in 1913, Stern in 1924, and many more researchers since.[16]

5.1.3 Equivalent Circuits

Modeling and interpreting impedance spectroscopy results is highly dependent upon the equivalent circuit chosen and oftentimes there can be an inherent ambiguity between multiple circuit models that can have similar responses. Below are presented the equivalent circuits commonly used to model solid electrolyte systems and supercapacitor systems.

Some of these equivalent circuits will appear very similar, and as expected, they would have similar responses. The motivation for including the equivalent circuits presented below and

solving them later is not just to demonstrate that they can have similar responses, which is a trivial exercise, but to construct competing physical interpretations for the system being studied from the basis of how these equivalent circuits were put together. Despite the similarity of the schematics for these equivalent circuits, and the obvious similar responses, the interpretation of the spectroscopy responses and assigning different circuit elements to different physical phenomena is quite different between these equivalent circuits. Eventually, additional types of experiments were performed in order to try to gleam more information about which physical interpretation was correct. The whole point of using the equivalent circuits is not to try to model the impedance spectroscopy results exactly, because that could be done with increasingly more complicated circuits, but rather to gain insight into the physics of the charge transport through the solid electrolyte system.

5.1.3.1 Equivalent Circuits Traditionally Used for Solid Electrolytes

Two common equivalent circuits that are used to model the response of solid electrolyte systems with and without the effects of grain boundaries and with negligible leakage current and contact resistance are introduced here.[51]

The most basic equivalent circuit model used to interpret the results of impedance spectroscopy is shown below in Fig. 5.3. This model has two conduction channels. One channel has a resistor, R, which represents the resistance to the flow of ions within the bulk of the solid electrolyte in series with a traditional capacitor, C. This capacitor, C, is the equivalent supercapacitance of the system at low enough frequencies to allow for ionic response. The supercapacitance can simplistically be thought of as two Helmholtz double layers, one at each of the electrode-electrolyte interfaces. The second conduction channel only has a capacitor, C_1 that is expressed as ξ C with ξ equal to the dimensionless ratio of C_1 to C. The motivation for introducing this unitless parameter will become apparent in Chapter 7 when the responses of the various equivalent circuits are analyzed.[51]

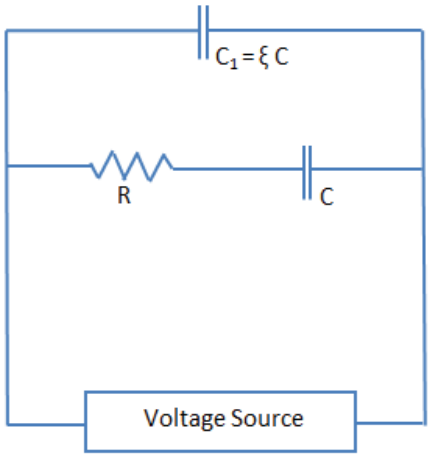

Figure 5.3: Simplest Equivalent Circuit Used to Model the Impedance Spectroscopy Response of a Solid Electrolyte with Blocking Electrodes [51]

As a point of simplification, future references to equivalent circuits introduced earlier will simply be called equivalent circuit 5.XX, where XX represents the figure number that corresponds to where that equivalent circuit was introduced. Therefore the equivalent circuit in the above figure will simply be referred to as equivalent circuit 5.3.

There is a characteristic of a resistor and a capacitor in series known as the time constant, equal to the product of R and C, with units of seconds. The time constant is the time it would take the current from the capacitor to decay to $1\text{-}e^{-1}$, or 63%, of its peak value flowing in a simple series through the resistor when the capacitor is removed from the voltage source. The equivalent circuits that will be presented throughout will get increasingly more complex, and the original concept of the time constant does not apply, but it will be helpful to assign values to different branches to help recognize at which frequencies they will represent a significant component of the circuit's response. Therefore a term will be introduced as the characteristic frequency of a conductive pathway and will be the inverse of two pi times the time constant.

There is no electronic resistance in the leads and electrodes in this model, as it is several orders of magnitude smaller than the ionic resistance and can be neglected. The result of this is to effectively have the characteristic frequency for the high frequency channel of equivalent circuit 5.3 go to infinity. Because the highest frequency channel represents only electronic motion, its resistance is almost negligible, on the order of Ohms, its capacitance is quite low, on the order of 10 picoFarads, and its characteristic frequency, on the order of 10GHz, is above the practical maximum frequencies applied in the laboratory setting, which are typically of the order of 1MHz to 100MHz. Therefore, the characteristic frequency of the high frequency conduction channels that represent only electronic motion is not reached, and the simplification of neglecting the electronic resistance when analyzing these models is supported. Later equivalent circuits introduced within the context of the multi-pore models include this resistive element so that

they match the circuits proposed for supercapacitive modeling in prior literature, but this element is not included when these circuits are analyzed further here and in Chapter 7, as its effects are negligible and removing it simplifies the analysis.

Because the conduction channel that models the effects of the two Helmholtz double layers includes supercapacitance it can be thought of as the lower frequency response, analogous to the low frequency response in the multiple conduction channels circuit used in the multi-pore models for supercapacitance. The magnitude of the resistance in this channel can vary from tens of Ohms to tens of thousands of Ohms, depending on the inherent ionic conductivity of the sample, the temperature of the experiment, and the geometry of the sample. A setup with two circular planar electrodes with a diameter of 1cm, ideal contact between the sample and the electrodes, and a charge separation of 1 angstrom equates to a capacitance of 7 microFarads. Two of these in series, one for each electrode-electrolyte interface, would then reduce that by half. The exact value is quite sensitive to the separation distance of the ions, the surfaces of the electrodes and the sample, which in turn depends on the quality of the contact of the electrode and the surface of the sample. In practice, the capacitance could be several orders of magnitude less. This would yield a characteristic frequency that ranges in order of magnitude from 10 Hz to 10 MHz. The higher frequency would result from samples with high ionic conductivity and low supercapacitance and with the experiments performed at elevated temperatures, thus increasing the ionic conductivity even further.

Another equivalent circuit model used to analyze solid electrolytes builds upon the equivalent circuit 5.3. This model attempts to account for the contributions to the ionic resistance by including the effects of grain boundaries traditionally encountered in a poly-crystalline ceramic sample. The model is represented in Fig. 5.4 below. This model assumes the ions preferentially flow through the bulk grains, and only transfer across grain boundaries when they encounter grain boundaries transverse to the flow. If ionic conduction were much easier along grain boundaries relative to through the grains, there would be an alternate lower impedance conduction channel representing the web of conduction paths along grain boundaries and this would be the preferential mode of ionic conduction.[51]

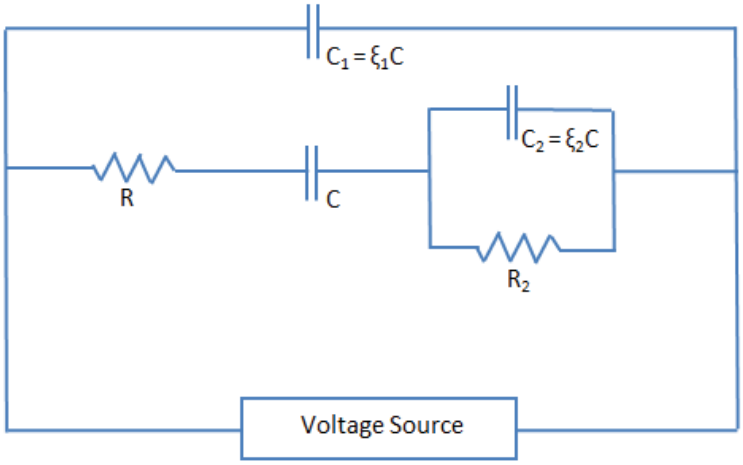

Figure 5.4: Equivalent Circuit Used to Model the Effects of Grain Boundaries[51]

Equivalent circuit 5.4, shown above, differs from the simpler equivalent circuit 5.3 in that an additional complex impedance element is added in series to the resistor and capacitor in the low frequency conduction channel. The complex impedance element is a resistor, R_2, and a capacitor, C_2, in parallel, representing the two possibilities for charge to either accumulate at the grain boundaries or transfer across the grain boundaries. The resistor represents the physical transport of ions across the grain boundary and the resistance they would encounter in the process. The capacitor represents the accumulation of ions on one side of the grain boundary and the excess of oppositely charged ions on the other side of the grain boundary. This can be viewed as a small scale Helmholtz double layer and would result in a ionically governed capacitance, thus it would be frequency dependent and only expected to contribute at low frequencies. Sequentially, charge attempting to traverse the sample would see a capacitor at the electrode-sample interface, a resistor modeling the bulk charge transfer through a grain, a resistor in parallel with a capacitor representing the first grain boundary encountered, and then more resistors followed by resistors in series with capacitors to denote additional grains and grain boundaries respectively, followed by a resistor for the final grain and then a capacitor for the final electrode-sample interface. Note that this circuit reverts back to equivalent circuit 5.3 in the limit that R_2 goes to zero, but that circuit should not be viewed as the correct model in that instance. If R_2 goes to zero, then the grain boundaries represent a conduction pathway with significantly lower resistance than the grains, and would therefore be the primary mode of ionic conduction.[51]

5.1.3.2 Multi Pore Models and Their Equivalent Circuits

In practice, supercapacitors achieve high levels of capacitance by both reducing the distance separating the layers of charge in the denominator of equation 5.1 and maximizing the surface area term in the numerator of equation 5.1. The increase in surface area is accomplished by using porous electrodes, which significantly increases the contact area between the electrode

and the electrolyte. Furthermore, the capacitance can be increased even more with electrochemical energy storage with appropriately chosen electrode and electrolyte materials, which is referred to as pseudocapacitance. The modeling of the response of a system with porous electrodes to impedance spectroscopy is what is most relevant to the results presented here. The pseudocapacitance is not included in these models as it is a form of electrochemical energy storage that is not present with a solid electrolyte with ionically blocking electrodes. The analogy between a solid electrolyte with ionically blocking electrodes and a supercapacitor without electrochemical energy storage in the form of pseudocapacitance is quite compelling. In terms of comparing results and modeling the systems, the only remaining difference is then whether the electrolyte is liquid or solid.[51]

The charges stored in a supercapacitor are both electronic and ionic. Due to the slower response of the ions in the electrolyte with respect to the electrons in the conductive electrodes, supercapacitors have significantly more dependence on the frequency, ω , of the applied voltage. If the electrodes are considered to be porous, with variously sized pores, then the response of the system to different frequencies can be thought of as follows. At low frequencies, near the DC limit, the ions in the electrolyte have enough time to respond to the applied voltage to migrate as close to the surface of the electrode as possible, and thus enter the smallest of permissible pores in the electrode to get as much ionic charge as close to the surfaces of the electrode as possible. As the frequency of the applied voltage is increased, eventually frequencies are reached such that the ions no longer have sufficient time to migrate into the smallest and deepest of pores, but still are accumulated near the surfaces of the electrodes. The average distance of the charge to the surface of the electrode has now increased relative to the low frequency limit, and thus the capacitance has decreased. At higher frequencies, the ions no longer have enough time to respond to the applied voltage and remain diffuse throughout the electrolyte without any ionic charge separation. The electrons are still able to respond to the applied signal, and the system behaves as a traditional capacitor with two parallel electrodes.[51]

The response of the system at varying frequencies can then be modeled with an equivalent circuit with multiple conduction channels. Each channel would have a resistive element for the resistance to the transport of charges, both ionic and electronic, and a traditional capacitive element representing the capacitance. The distribution of pore sizes and shapes determines the number of conduction channels chosen to model the behavior of the ions. Two potential equivalent circuits used in the analysis of supercapacitors are presented below. [16,17]

An equivalent circuit that captures the frequency dependence of the multi-pore model is shown in Fig. 5.5, and is a simplified version of one proposed by Conway and Miller in the 1990s in the context of supercapacitors.[16,17] This model is similar to models used for transmission lines that have been around since the 1800s. The simplest way to consider this equivalent circuit model is start with a resistive and a capacitive element in series. This is the high frequency response of the circuit, and is shown as R_e and C_1 in equivalent circuit 5.5, shown below. At lower frequencies, the ions have enough time to start to respond to the applied signal, and they

encounter resistance, R_2, and contribute capacitance, C_2, as they do so, but there is still the original resistance that the electrons encountered, R_e. This new conduction pathway must therefore still go through R_e, but now is an alternative to the lower capacitance of the system due to just electronic response at high frequencies, and thus an alternate pathway to C_1. At even lower frequencies, the ions now have a chance to respond even further to the applied signal, and they encounter even more resistance, R, and contribute even more capacitance, C, as they do so. This additional response would be an alternative to the ions being located where they were at higher frequencies, and therefore is an alternative conduction channel to C_2. There is still the resistance of R_e to go through for the electrons and R_2 of the ions for their initial response to go through. The original multi-pore models had five or more levels of further response to lower frequencies. This was done to model complicated porous electrodes and liquid electrodes where the ions were freer to travel into these variously sized pores. The interface between a solid electrolyte and an ionically blocking electrode is not envisioned to have as wide of a dispersion of pores, and three channels are used in these analyses in an attempt to keep the equivalent circuits no more complicated than they need to be.

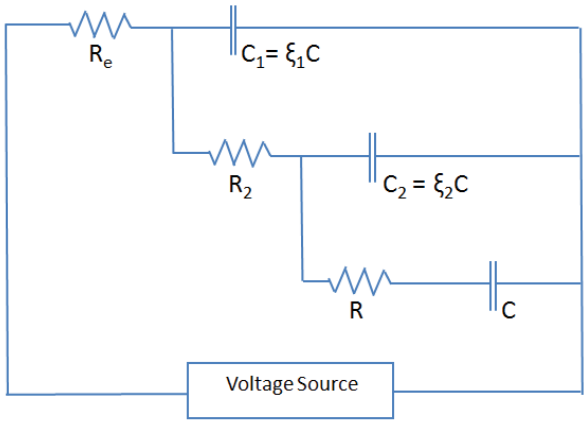

Figure 5.5: Circuit Diagram of Equivalent Circuit of a Supercapacitor with Three Conduction Channels in the Multi-Pore Model proposed by Conway and Miller[16,17]

A second equivalent circuit that has been proposed for the multi-pore model was put forth by Zubieta and simplified by New is shown in Fig. 5.6.[18,19] This equivalent circuit is similar to the one proposed by Conway and Miller, but it is simpler to analyze, but more difficult to describe physics behind the layout of the circuit. Equivalent circuit 5.6, shown below, simply has three parallel RC branches. Each one has different resistive and capacitive elements, which govern the higher frequency limit for response of that branch.

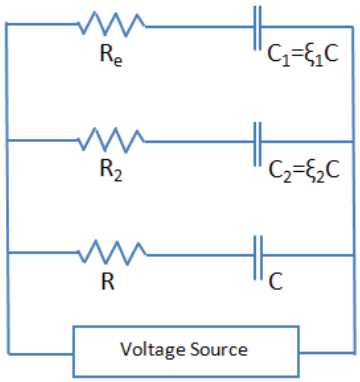

Figure 5.6: Circuit Diagram of Equivalent Circuit of a Supercapacitor with Three Conduction Channels in the Multi-Pore Model proposed by Zubieta and New[18,19]

The magnitude of the resistance in the low frequency channel should be higher than the resistance in the intermediate channel, which in turn should be higher than the resistance in the high frequency channel. This is because the ions do not move as far in higher frequency channels than they do in a lower frequency channels. Likewise, the magnitude of the capacitance should also decrease between a lower frequency channel and a higher frequency channel for reasons mentioned previously.

5.1.4 Correlating AC Impedance Spectroscopy Responses of Solid Electrolyte Systems with Equivalent Circuits

The responses of the equivalent circuits are highly susceptible to the magnitudes of the individual circuit elements. This is illustrated as solutions to these circuits are presented in Chapter 7. Before the solutions to the equivalent circuits are presented though, it is important to check the validity of these models against real data, and some concerns these comparisons raise. To help form a better comparison with the real data, Nyquist plots are presented in Fig 5.7 for the equivalent circuits 5.3, 5.4, 5.5, and 5.6. To simplify the circuits, R_e was set to zero, where it appeared. Again, it bears repeating, that the responses of the equivalent circuits are highly susceptible to the magnitudes of the individual circuit elements. The responses presented here are for circuits with carefully chosen elements such that all the potential features in the circuits' responses are present and of comparable orders of magnitude for better illustration. These responses are solved for a wide range of frequencies, and as will be shown in Chapter 7, the magnitude of the capacitance term, C, couples with the frequency term, and the responses are solved as a function of ωC. The responses of these equivalent circuits are displayed for ωC equal to $2x10^{-5}$ Ω^{-1} to 10^{6} Ω^{-1}, which allows the full response to fit and for the higher frequency features to be seen. Note that in all Nyquist plots presented here, and throughout this research, the magnitude of the complex impedance will always tend towards zero with increasing frequency.

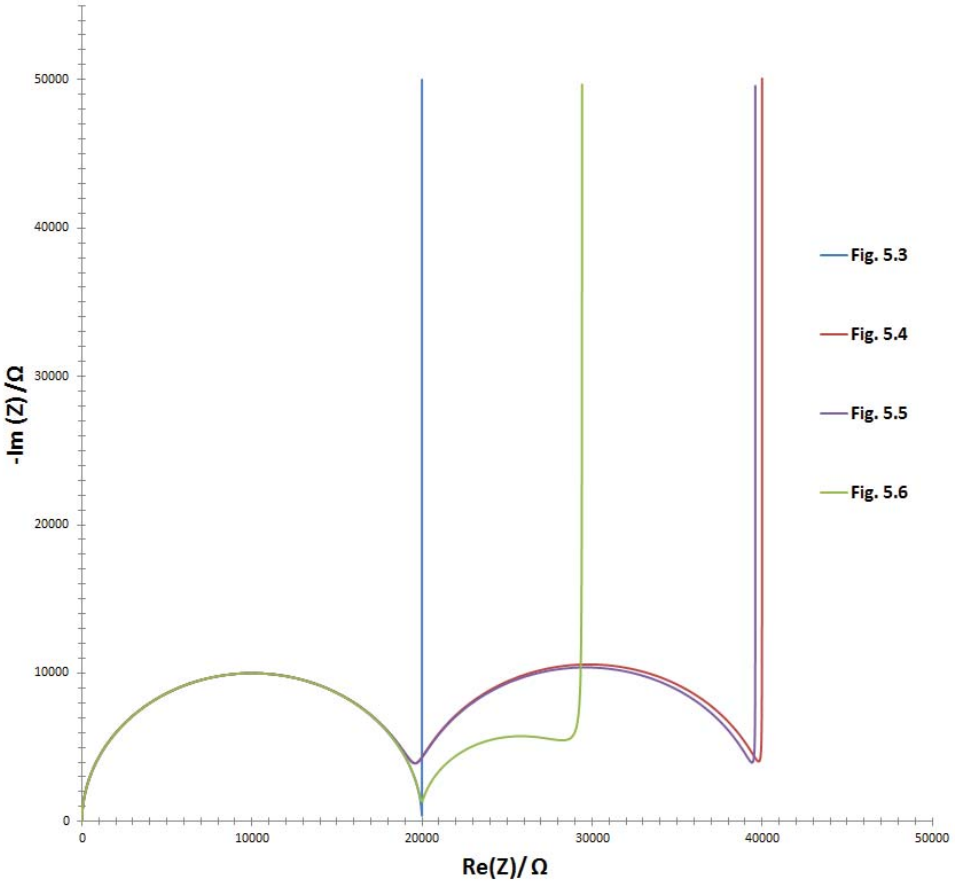

Figure 5.7: Nyquist Plots for Equivalent Circuits Figs. 5.3, 5.4, 5.5, and 5.6. Magnitudes of circuit elements in Figure 5.3 are R = 20,000 Ω and ξ = 0.0001, in Figure 5.4 and Figure 5.5 are R_1 = R = 20,000 Ω, ξ_1 = 0.0001, and ξ_2 = 0.01, and in Figure 5.6 are R_2 = 30,000 Ω, R = 60,000 Ω, ξ_1 = 0.0001, and ξ_2 = 0.01

Below, for comparison with Fig 5.8, are presented some results of the solid electrolytes from the garnet class of solid electrolytes to impedance spectroscopy in Figs 5.8-5.11.

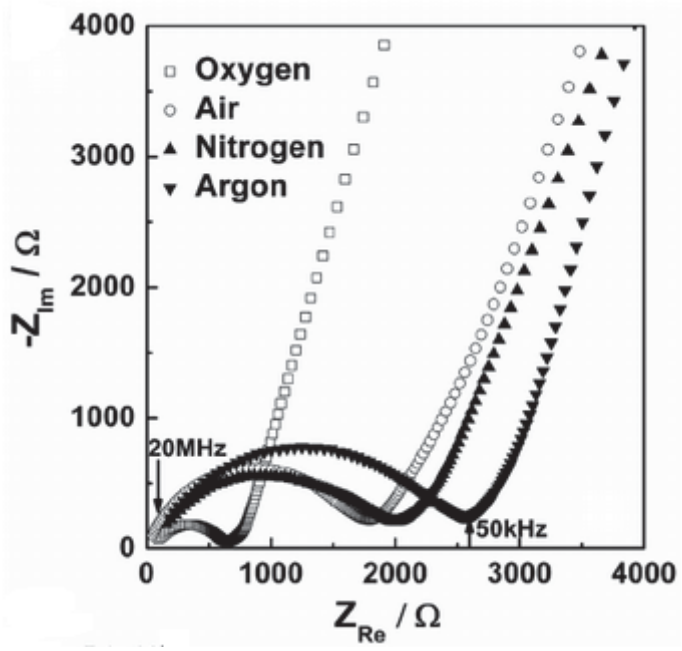

Figure 5.8: Nyquist plot for the response of a solid electrolyte system to AC impedance spectroscopy showing a more vertical low frequency tail and without a second minimum. Shown are LLTZO samples with Al doping sintered in different atmospheres at 25C [23]

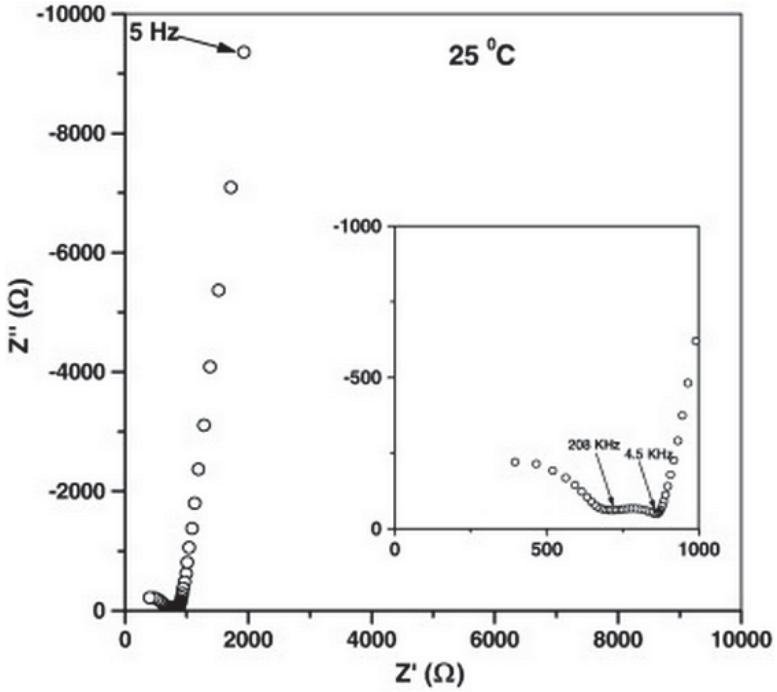

Figure 5.9: Nyquist plot for the response of a solid electrolyte system to AC impedance spectroscopy showing a more vertical low frequency tail and with a second minimum. Shown is $Li_7La_3Zr_2Ta_xO_{12}$ with yttrium doping at 25C [10]

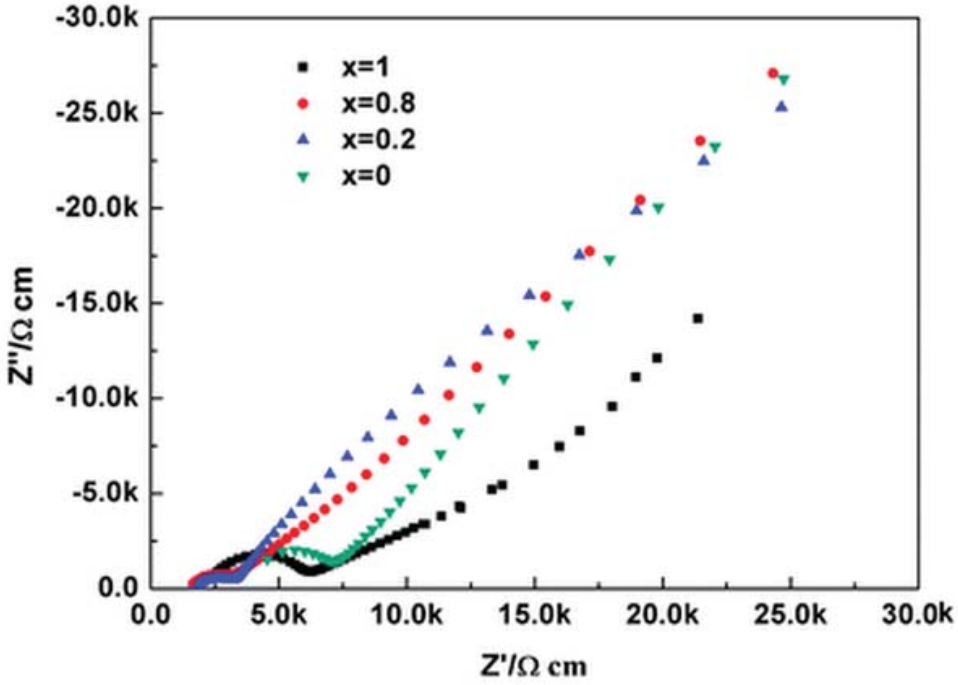

Figure 5.10: Nyquist plot for the response of a solid electrolyte system to AC impedance spectroscopy showing a more inclined low frequency tail and without a second minimum. Shown are $Li_{7-x}La_3Zr_{2-x}Ta_xO_{12}$ at 25C with x=0, 0.2, 0.8, and 1[7]

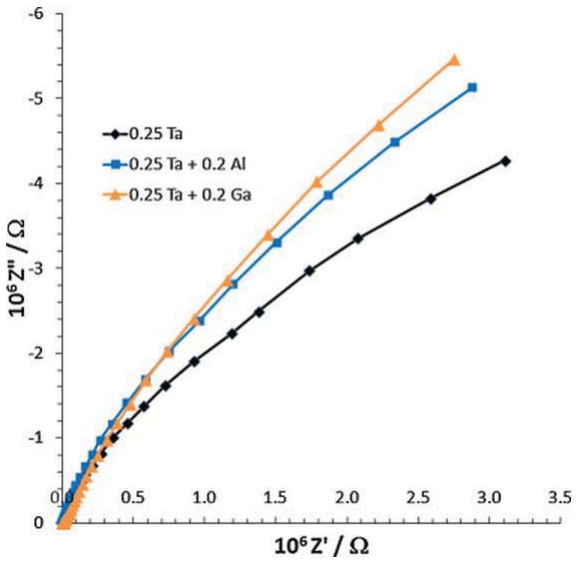

Figure 5.11: Nyquist plot for the response of a solid electrolyte system to AC impedance spectroscopy showing a more inclined low frequency tail and with no minimums. Shown are $Li_7La_3Zr_2Ta_xO_{12}$ with Ta, Al, and Ga doping at 25C [24]

To fully correlate all the features seen in the response of a system to AC impedance spectroscopy may sometimes require more complicated equivalent circuits. Equivalent circuits 5.4, 5.5, and 5.6 exhibit a maximum of two local minima and two local maxima on a Nyquist plot. Modeling a system with a more complex response with an equivalent circuit requires a more complicated circuit with additional conduction pathways. As such, an equivalent circuit with 5 conduction channels representing the original multi-pore model proposed by Conway and Miller is shown in Fig. 5.12 below. There is relevance in introducing a more complicated model, and it is referenced in Chapter 7 as a possible explanation for some impedance spectroscopy responses.[16,17]

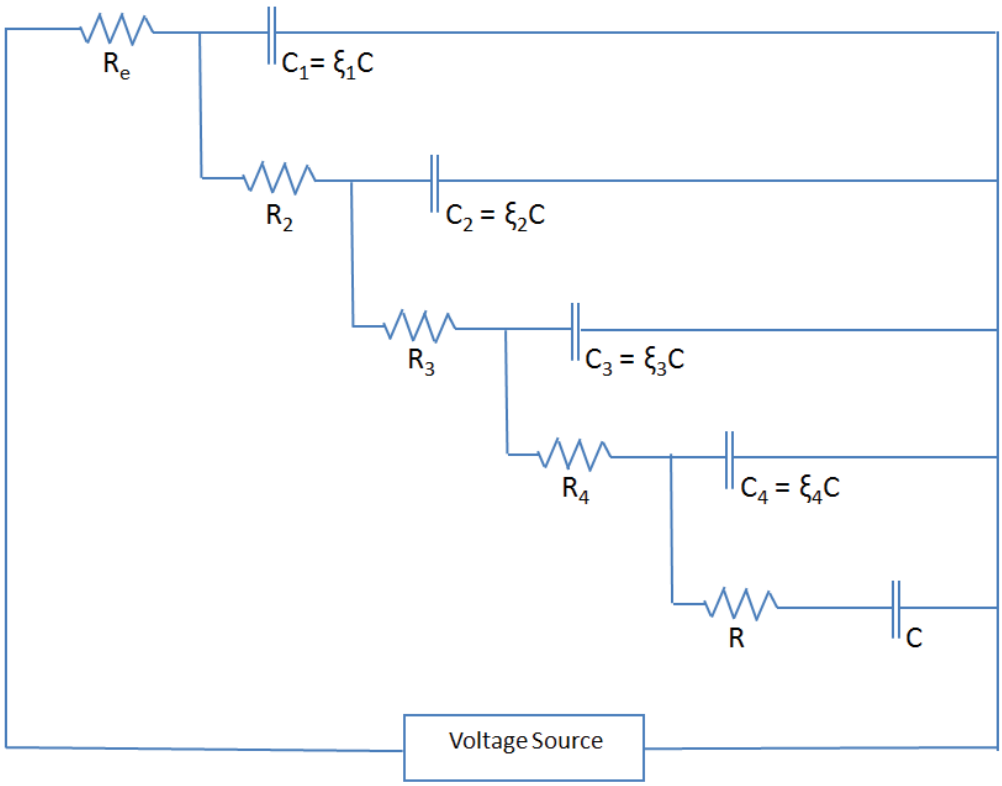

Figure 5.12: Equivalent Circuit 5.12 within the context of the multi-pore model with 5 conduction channels, extension of the 3 conduction channel model shown in equivalent circuit 5.5 [16,17]

5.1.5 Ionically Blocking Electrodes and Semi-Infinite Diffusion

The equivalent circuit models assume that the electrode-sample interfaces completely block the flow of electrons into the sample and lithium ions into the electrodes. This assumption is quite valid for the blocking of electrons. If there was a conductive pathway for electrons through the sample, the imaginary component of the low frequency response of the complex impedance would tend to zero, as opposed to the significantly larger negative values that is repeatedly seen in Figs. 5.8-11.

The assumption that the electrodes block the ions appears quite valid at high frequencies, due to the similar response between the models shown in Fig. 5.7 and the responses of solid electrolyte systems shown in Figs. 5.8-11. This is in agreement with the traditional equivalent circuits used to model solid electrolytes, 5.3 and 5.4, and the multi-pore models for supercapacitors, 5.5, 5.6, and 5.12, as the short time scales do not allow much, if any, physical movement of the ions. At low frequencies, if the ions can physically diffuse into and out of the electrodes, a real component of the impedance could be added to the circuit, as charge is physically moving into and out of the electrodes.

In the lower frequency regime of the impedance spectroscopy response of the system, it has been proposed that there is some diffusion into and out of the electrodes. The motivation for these claims is the vertical tail tilting more towards the real axis, which is seen to varying degrees in Fig. 5.9 through 5.12 and other experimental data. One solution to the potential diffusion in this low frequency regime is where the electrode is modelled as a semi-infinite planar electrode with diffusion across the boundary and is known as Warburg diffusion, and the impedance of the Warburg element is shown in equation 5.2 below. The low frequency solution to Warburg Diffusion would result in the tail tilting to an angle of 45 degrees.[15,52] The corresponding element added to equivalent circuits is called a Warburg element, commonly denoted with a W on circuit diagrams.

$$Z_{Warburg} = \frac{A}{\sqrt{i\omega}} \qquad \text{equation 5.2}$$

The constant A in equation 5.2 depends on the kinetics of the diffusion process as well as low frequency impedances of the system. The impedance of the Warburg element tends to zero at high frequencies.

Another circuit element that has been suggested to be used in equivalent circuits for electrochemical systems is called a constant phase element. The constant phase element comes from a generalized mathematical treatment of circuits which expresses the voltage in terms of fractional derivatives of the current with corresponding coefficients. With one fractional derivative and a constant coefficient used, the circuit element is said to have a constant phase angle, and the impedance of the circuit element is expressed in equation 5.3 below.[15,53,54] The corresponding element added to equivalent circuits is called a CPE element, noted with a CPE or a Q on circuit diagrams, often with the value for α noted.

$$Z_{constant\ phase\ element} = \frac{Q}{(i\omega)^{\alpha}} \text{ equation 5.3}$$

The constant B in equation 5.3 depends on the value of α. For α = o, the impedance of the constant phase element is purely real and is equal to B, so B would be a traditional resistive circuit element. For α = 1, the impedance of the constant phase element is purely imaginary and is that of a capacitor and B would have units of inverse Farads. For other values of α, the units of B would change correspondingly.

The fits these circuits provide can be quite impressive, though the physical interpretation of the elements is not obvious. It is for that last reason that they are avoided in the context of this research. Nevertheless, there are two aspects of the constant phase elements that are of notice here. One is that equation 5.3 reduces to equation 5.2 when α is 1/2. Thus, Warburg Diffusion can be thought of as a special case of the more general constant phase element. Because the special case of α = 1/2 does have a physical interpretation in the context of Warburg Diffusion, it is included in the analysis of the results presented in Chapter 7.

The second one is contrasting the constant phase element with an extension of the multi-pore model of equivalent circuit 5.12. This extension of equivalent circuit 5.12 can be used to show a tilting of the low frequency tail, and by adding more conduction channels, the fit can be made to approximate a straight line with improving degrees of accuracy. The extension can be thought of as a circuit consisting of a lot of nested copies of equivalent circuit 5.3. The total impedance from one equivalent circuit 5.3 becomes the capacitive term for the next level up equivalent circuit 5.3. The total impedance of this new circuit becomes the capacitive term in equivalent circuit 5.3 for one more level up, and so on. This entire equivalent circuit with many nested levels has been described as a multi-pore model with fractal geometry describing the different pore geometries. Constant phase elements have been proposed as alternatives to these models to generate the same tilting of the low frequency tail.[15,54] Again, it is worth noting that there is a clear physical interpretation to the multi-pore models and not one with the constant phase elements, so constant phase elements are not used in analyzing the results presented here.

The interpretation of the tilting of the vertical tail in the impedance spectroscopy responses of the systems here, to be shown in Chapter 7, as well as in prior published results, Figs 5.9 through 5.12, and how it relates to the equivalent circuit models and possible diffusion into the electrodes is expanded upon further in Chapter 7.

5.2 In-Situ Nanoscale Ionic Transport Measurements

Recently, ionic transport on the nanoscale has been explored by using an atomic force microscope, AFM, with a biased tip on electrochemically active samples.[20-22,55,56] These measurements were done on lithium conducting solid electrolytes and were performed in an inert environment provided by an argon glove box. A basic schematic of the experimental setup is shown in Fig. 5.14 below.

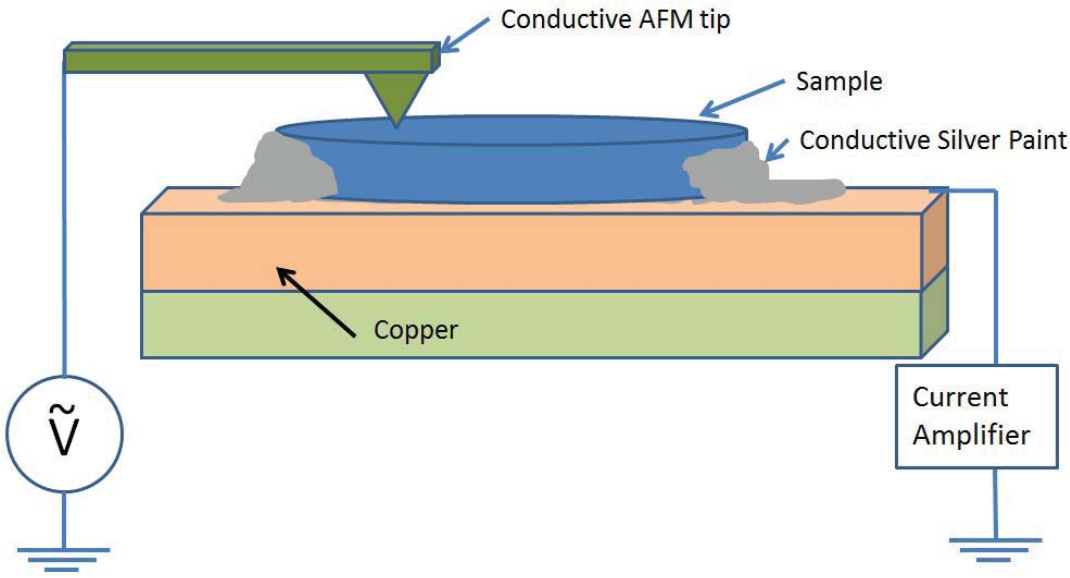

Figure 5.13: Experimental setup for the in-situ nanoscale ionic transport measurements detailed here and in Chapter 7

The premise behind these measurements is that a voltage source is varied, providing a bias to the conductive tip, which is in contact with the surface of the sample. The counter surface of the sample is conductively contacted with conductive backing. With the AFM tip in one location, the bias of the tip is varied and the tip height and current measured through the current amplifier are recorded as a function of the tip bias. For an electronically conductive sample, there would be a current for small biases, which would follow a linear relationship with the applied bias, the slope of which would represent the bulk resistance of the sample and the tip contact resistance as well as other resistances in the circuit. For a purely insulating sample, you would not expect any current to be measured, provided the applied bias was not strong enough to breakdown the sample. For increasing biases, a strain would be recorded as a change in the tip height as the increasing applied bias of the tip induces electrostatic responses in the sample.

Interesting results occur when the sample is ionically conductive, but electrically insulating. Assuming the tip remains inert in the process, when a large enough negative bias is applied to the tip, a positively charged ion (or negative ion with a positive bias) will leave the ionic conductor to be reduced (or oxidized) on the surface of the sample and a corresponding oxidation (or reduction) occurs at the reverse electrode. Current has now flowed through the sample and this detectable current can be measured through the current amplifier. The bias of the tip can then be reversed, and the reverse reaction can occur, with an oppositely signed current now measured. Additionally, there will be detectable strain before particles nucleate on the surface, as the bias on the will interact with the mobile charge ionic species in the sample. This process is detailed in Fig. 5.14 below. It is worth pointing out that this is a local process on the sample's surface, but also a bulk process through the sample. The current being measured

has travelled through the entire sample. Further details of the experimental setup can be found in recent literature.[20-22,55,56]

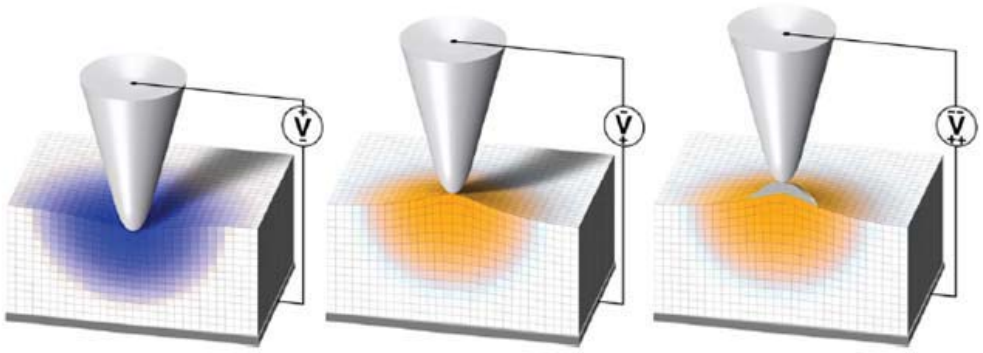

Figure 5.14: Reaction of an ionically conductive sample to different tip biases. The first two images represent strain from ionic deficiencies and abundances below the biased tip respectively. The third image represents particle nucleation once a sufficient negative bias has been applied to the tip, assuming a positive mobile ionic species [20]

If the mobile ionic species is lithium, care must be taken to ensure that the lithium does not encounter ambient conditions after it is reduced on the surface, or it will react, and the feature on the surface can no longer be correlated with lithium, nor can the reversibility of the process be explored. Therefore, experiments that have probed the mobility of lithium in the past, as well as experiments done here and detailed in Chapter 7 were performed in a controlled argon environment inside a glove-box.

Several experimental parameters can be varied to probe the ionic transport properties of the sample, such as: the applied bias required for particle nucleation, the reversibility of particles as a function of their size or the applied bias, the rate the bias is swept, the waveform of the applied signal, the applied bias versus different counter electrodes, and correlation of the nucleated particles with metallic lithium are a few that have tried. Results of these experiments are shown in Figs. 5.15 through 5.20 below.[20-22,55,56] These only represent a few of the results this new technique has offered towards measuring the ionic transport properties in solid electrolytes. For all of these results, the material being tested was LICGC model AG01, an amorphous lithium ionic conductor made by Ohara, Inc. The purpose of including the results chosen here is that they correlate with the work presented in Chapter 7 and will be referenced in regards to interpreting those results as well as they provide an overview of this technique and its potential.

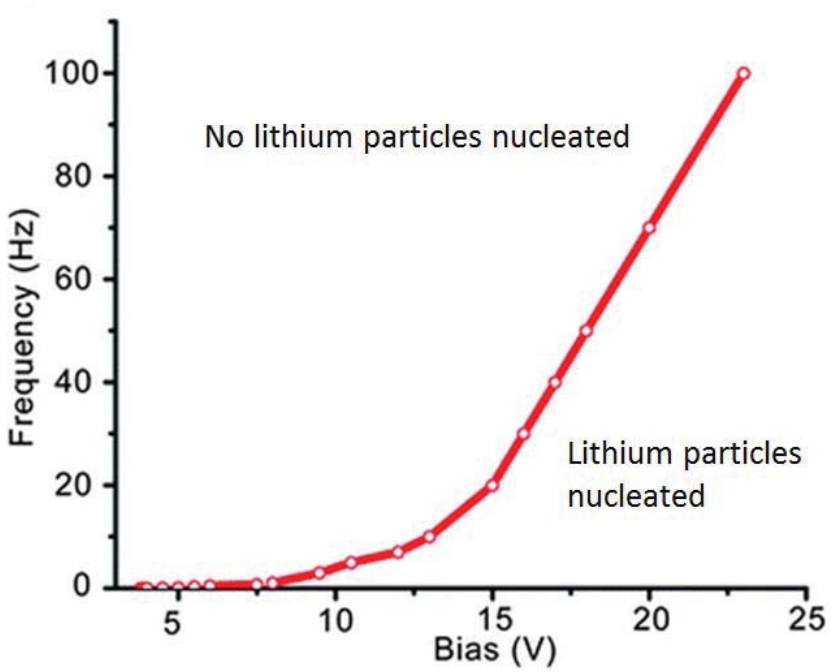

Figure 5.15: Maximum applied frequency of an AC sinusoidal waveform versus applied bias required for lithium particle nucleation on LICGC. [22]

The waveform of the applied bias plays a large role in the nucleation of lithium particles. With a sinusoidal waveform, the lithium particles did not nucleate for frequencies above 1Hz for biases below 5 volts, but with a triangular waveform, lithium particles nucleated at 5 volts at 10Hz, and at 4 volts at 5Hz, see Fig. 5.16 below. Possible reasons for this are discussed in chapter 7.[20,22]

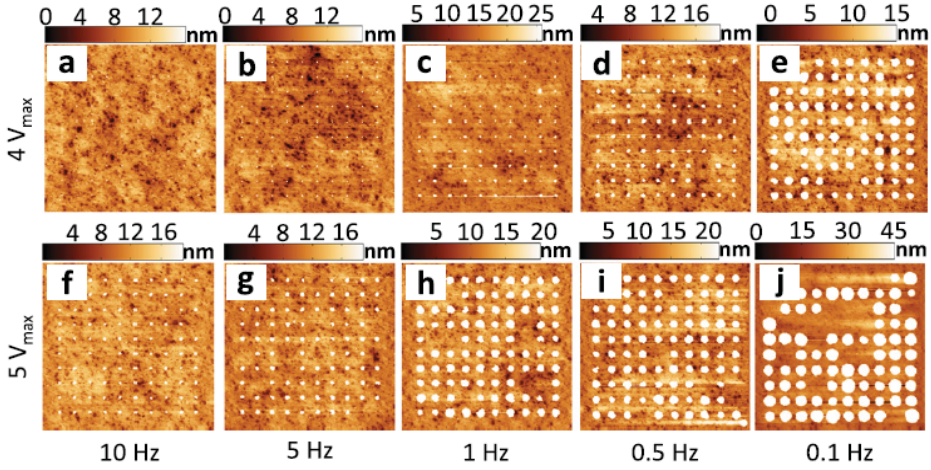

Figure 5.16: Topographical AFM images of Lithium nanoparticles formed on LICGC for applied biases of 4V and 5V with AC triangular waveforms applied at different frequencies [20]

One of the challenges with nanoscale measurements is correlating the nanoscale phenomena and their corresponding parameters with macro parameters. This problem persists for many

fields of nanoscale measurements, and is not unique to these nanoscale ionic transport measurements presented here. To address that disconnect, simulations were run to model the physical electrical field throughout the sample at different distances from the biased conductive tip. These results are shown in Fig. 5.17 below. [22]

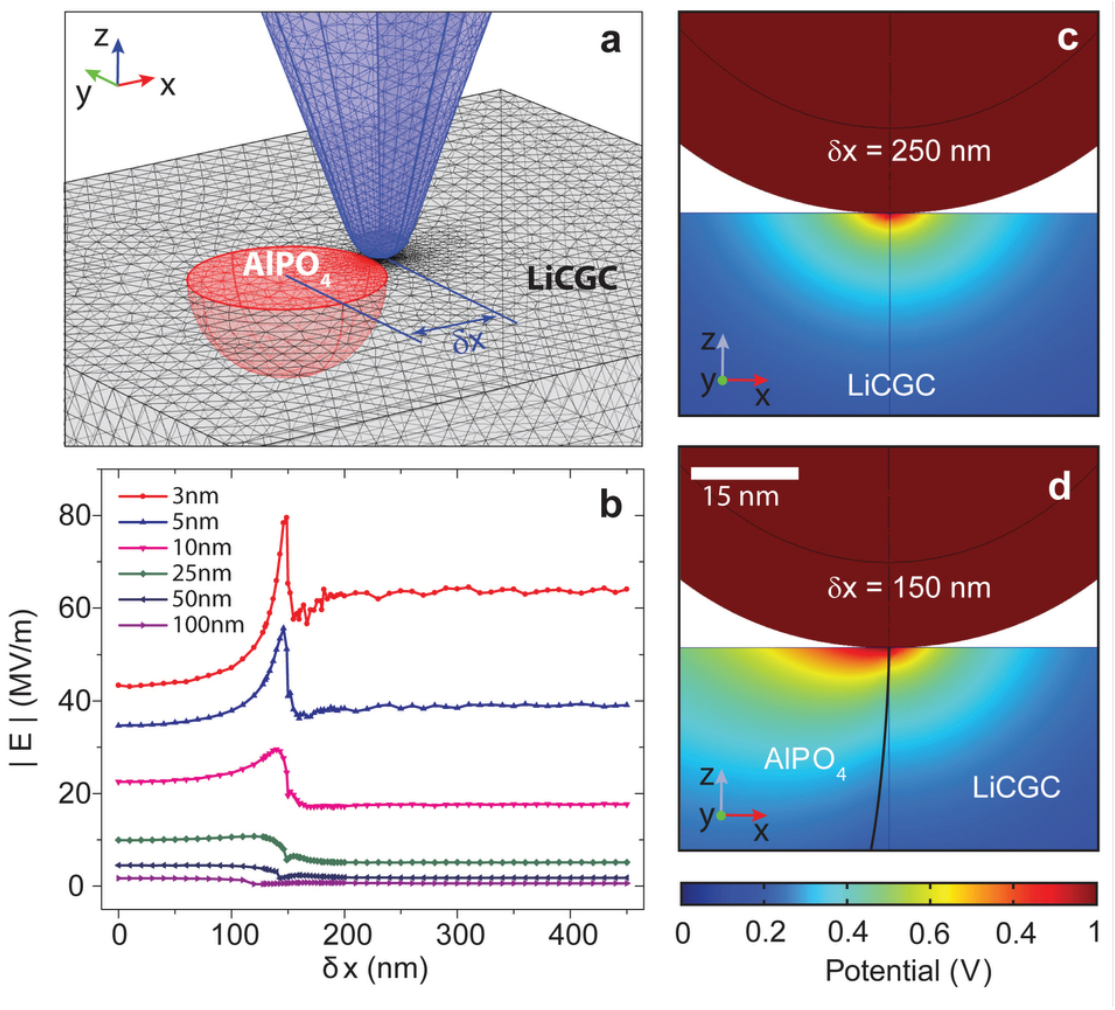

Figure 5.17: Calculated electric potential and electric field below conductive tip inside solid electrolyte, LICGC. **a)** schematic of the tip a distance δx from a ferroelectric impurity in LICGC, **b)** electric field strength at various depths inside LICGC versus distance δx, **c)** distribution of the electric potential in a cross section of the conductive tip and LICGC with δx = 250nm, **d)** distribution of the electric potential in a cross section of the conductive tip and LICGC with δx = 150nm. Note, the scale bar in d) is common to a), c), and d). [22]

To demonstrate potential scalability of the initial measurement technique, results are presented in Fig 5.18 that show a microscale electrode is biased by placing the conductive tip on it, and the entire electrode is biased, lithium reduced on the surface, corresponding current and tip heights measured, and then process is reversed and cycled.[21]

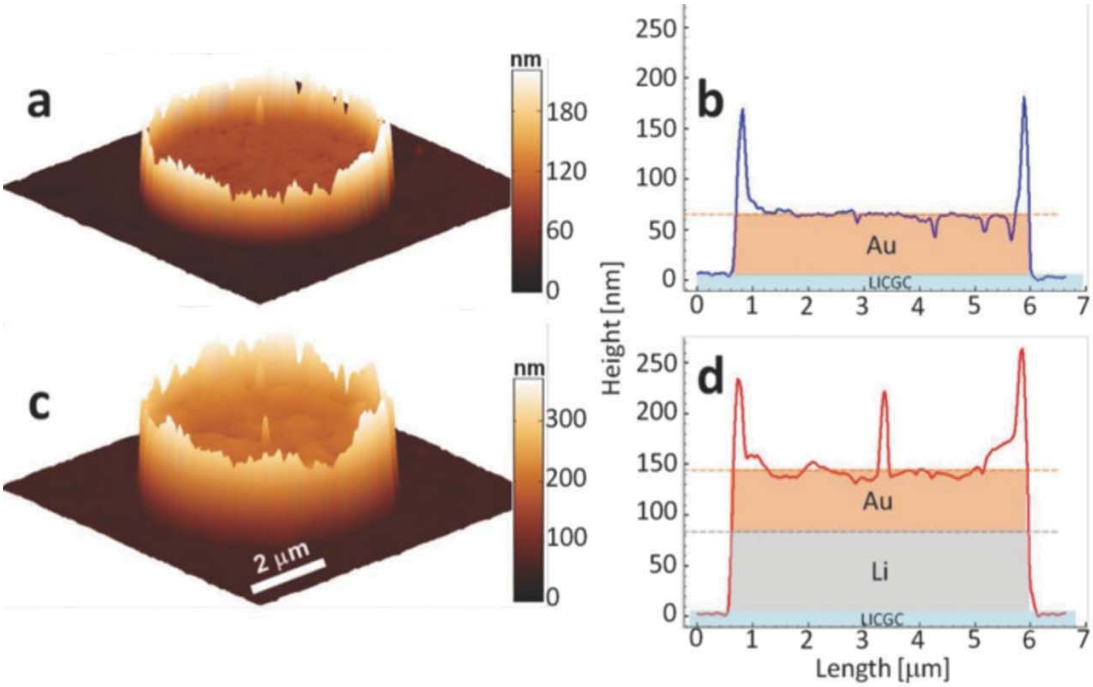

Figure 5.18: AFM topography of gold electrode on LICGC before and after cyclic voltammogram studies
a)prior to potentiostatic cycling, **b)**cross section through approximate center of a), **c)**after 1000 cyclic voltammogram cycles from -5V to +5V vs Cu counter electrode, **d)** cross section through approximate center of c)[21]

To confirm the presence of lithium particles on the surface of the solid electrolyte, and not another species being reduced which would account for the particles, three methods are used. First, shown in Fig. 5.19 below, the volume of the particles divided by the density of metallic lithium is correlated with the integrated current associated with that particular particle. Second, a solid electrolyte was cover with hundreds of particles and placed in a sealed quartz tube and then analyzed via Electron Paramagnetic Resonance (EPR). The spectra are shown in Fig. 5.20 below and the peaks at 332mT correspond to metallic lithium. The third method, not shown, was to analyze the results via Raman spectroscopy, where correlation with bulk metallic lithium was also demonstrated.[20,22]

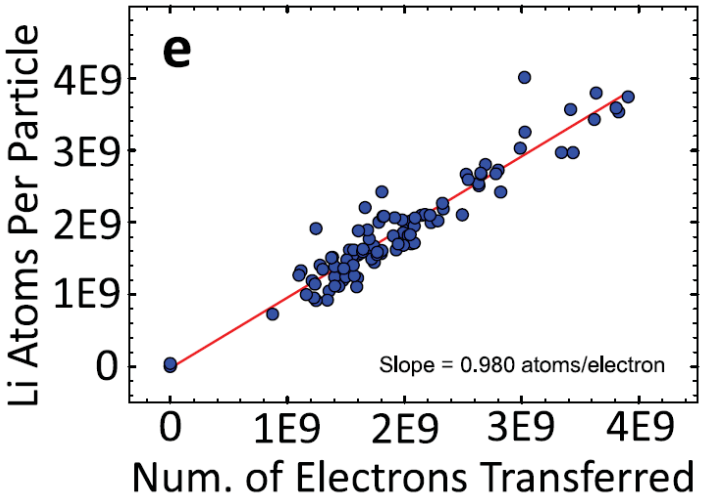

Figure 5.19: Correlation between number of electrons transferred (integration of current) and number of lithium atoms transferred (volume of the particles created) [20]

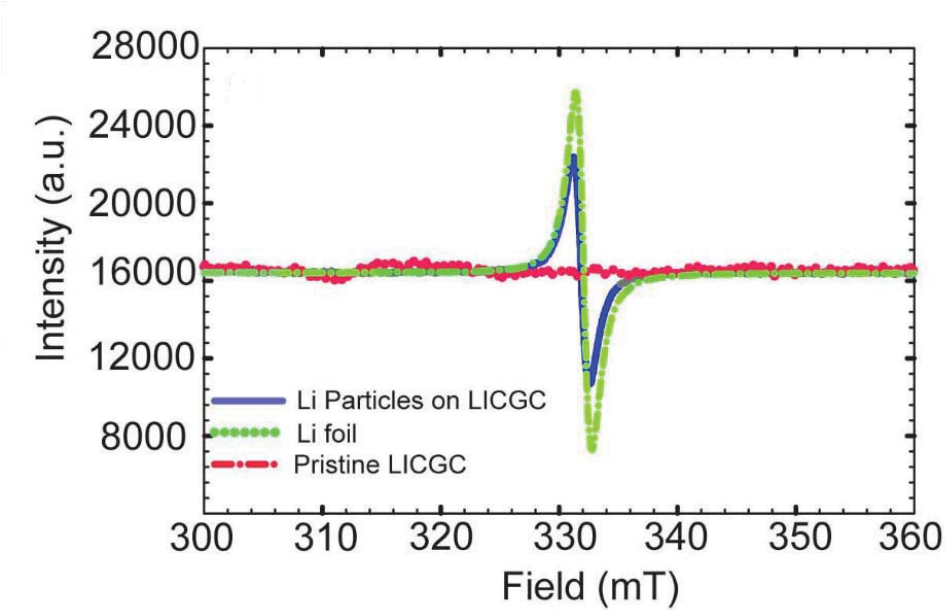

Figure 5.20: Correlation between particles nucleated on surface and metallic lithium [56]

5.3 Determining Ionic Transport Properties of the Material

Once the features on the AC impedance spectroscopy are associated with the resistance due to ionic transport inside the sample being tested, then the magnitude of the resistive value can be equated with the ionic conductivity of the material. If multiple semi-circular regions are seen and depending on the equivalent circuit used, there can be several resistive values from which to choose. In the case of multiple semi-circular regions or even the potential for multiple resistive elements, published reports usually report both the bulk ionic conductivity as well as the total ionic conductivity of the sample. The solutions to the equivalent circuits and the associated features on the Nyquist plots with which the magnitudes of the elements in the circuits are determined are provided in Chapter 7.

There are two properties that can be calculated once the magnitude of the resistance associated with ionic conductivity is determined - the ionic conductivity for the material, σ, and the activation energy for the temperature mediated process of ionic conductivity, E_a.

Once the value for the bulk ionic resistance that is associated with ionic conductivity is determined, the ionic conductivity, σ, is the thickness of the sample, t, divided by the product of the bulk ionic resistance, R, with the cross sectional area of the sample transverse to the flow of ionic current, A. This can be slightly modified to account for the fact that the sample is not 100% dense, by then dividing by the specific gravity of the sample, γ, relative to the theoretical maximum density of the sample, shown in equation 5.4 below. It should be noted that a simple Ohmic response is assumed, and therefore, the impedance of the system should not vary when the applied voltage is changed.

$$\sigma = \frac{t}{R\,A\,\gamma} \qquad \text{equation 5.4}$$

The activation energy is determined by associating the temperature dependence of the ionic conductivity with the Arrhenius equation. Two different methods are used to determine the activation energy and the current literature appears split on the correct method. One is to assume a basic Arrhenius dependence given in equation 5.5 below.

$$\sigma(T) = \sigma_o e^{-E_a/(k_B T)} \quad \text{equation 5.5}$$

The constant, k_B, in the exponent is Boltzmann's constant. In this equation, the pre-exponential factor, σ_o, is not temperature dependent. Taking the natural log of both sides yields a linear relation between ln(σ) and 1/T, with the slope equal to E_a/k_B, given in equation 5.6 below.

$$\ln(\sigma(T)) = \ln(\sigma_o) - \frac{E_a}{k_B}\frac{1}{T} \text{ equation 5.6}$$

The exact value of the pre-exponential factor, σ_o, is not required to calculate the activation energy.

The second method arrives at a similar equation from basic principles, with the exception of a temperature dependence of the pre-exponential factor that goes as 1/T. The derivation starts with the Nernst-Einstein expression which relates the ionic conductivity to the diffusion coefficient, D, given in equitation 5.7 below.[37]

$$\sigma(T) = \frac{nq^2D}{k_BT} \quad \text{equation 5.7}$$

In equation 5.7, *n* is the number of ions per unit volume and q is the ionic charge. The diffusivity of the ions, D, is given by equation 5.8 below.[37] Note, than an extra dependence on temperature found in the denominator for the expression for diffusivity is omitted, in-line with the traditional exponential dependence of diffusivity on temperature.

$$D(T) = zNc(1-c){a_l}^2v \qquad \text{equation 5.8}$$

In equation 5.8, z is the number of nearest neighbor sites, N is the density of the nearest neighbor sites, c is the concentration of ions, a_l is the distance between sites and v is the jump frequency which assumes a classical Arrhenius dependence on temperature and is given by equation 5.9 below.[37]

$$v(T) = v_o e^{-E_a/(k_BT)} \quad \text{equation 5.9}$$

In equation 5.9, v_o is a non-temperature dependent pre-exponential factor controlling the jump frequency. Equations 5.7, 5.8 and 5.9 can be combined to yield equation 5.10 below.

$$\sigma(T) = \frac{nq^2zNc(1-c){a_l}^2v_o}{k_BT} e^{-E_a/(k_BT)} = \frac{\sigma'_o}{T} e^{-E_a/(k_BT)} \qquad \text{equation 5.10}$$

In equation 5.10, there is now temperature dependence in the pre-exponential factor. Note that this is method is similar to how, in Chapter 3, the researchers were able to equate the activation energies calculated from density functional theory with ionic conductivities. The activation energy is found by multiplying both sides by T, and then taking the natural logarithm of both sides to yield a linear relation between ln(σ T) and 1/T, with the slope equal to E_a/k_B, shown in equation 5.11 below.

$$\ln(\sigma(T)T) = \ln(\sigma'_o) - \frac{E_a}{k_B}\frac{1}{T} \qquad \text{equation 5.11}$$

6.0 Sample Synthesis and Compositional Characterization

The goal of the sintering study initially was to synthesize materials with a dispersion of grain sizes. Ultimately, as new measurement techniques became available, this study became focused on synthesizing dense samples that could withstand the sample preparations necessary to achieve the finished surfaces required to perform nanoscale transport measurements on the surface.

The synthesis route outlined here differs from prior reported synthesis of this material in that the sintering temperatures were higher, the resulting density was higher, and the secondary variables that affected the sintering results were documented.

6.1 Experimental Procedures

Solid state synthesis was done using the precursor materials, Li_2CO_3 (99% Alfa Aesar), La_2O_3 (99.99% PIDC), and Ta_2O_5 (99.999% PIDC), which were added with stoichiometric ratios to yield 50 gram batches of $Li_5La_3Ta_2O_{12}$. Between 5 and 15 percent excess of lithium carbonate was added to the initial starting mixture. The batch was then initially ball-milled with zirconia grinding media and 100mL of deionized water for 24 hours. Following initial ball-milling, the batch was dried at 70C for 48 hours, and crushed to a fine powder in a pistol and mortar to re-mix the solid solution to account for uneven precipitation during drying. The batch was then placed in an alumina crucible and heated to 700C and held for 8 hours with heating and cooling rates of 1C/min.

A second ball-milling for 24 hours then followed with zirconia grinding media and 100mL of isopropanol. The batch was then dried for 72 hours at 70C. Once dried, the batch was crushed with pistol and mortar and 0.5% by weight of a copolymer binder (acrylic copolymer paraloid, B-72, Richard E. Mistler, Inc.) in acetone solution was added in 2 parts acetone 1 part binder by weight solution. Then the batch and binder mixture was put into suspension with the addition of approximately 50 mL of additional acetone. The suspension was dried over a hot plate at 85C while stirring with a glass stir rod. After all the visible traces of acetone were evaporated, the batch was dried for 48 hours at 70C to remove and remnants of acetone.

Once dried, the batch was crushed with a pistol and mortar and sieved with a 200 sieve. The remnants of the batch that did go through the mesh were re-crushed with the pistol and mortar and returned to the sieve. Pellets were pressed with the sieved powder in a 13mm diameter die. Nominally 0.8 grams of powder were used per pellet. The die was then compressed with 2000 lbf of uniaxial force for one minute. The binder was then burned out of the pellets by heating to 500C and holding for 8 hours with a 1C/min heating and cooling rate. Next the pellets were placed in latex bags, vacuum sealed, and placed in a cold isostatic press, which was pressurized to 30,000 psi for 24 hours.

Once removed from the isotactic press, the pellets were held in an oven at 120C for between 1 and 20 days until ready they were ready to be sintered. For sintering a tube furnace was used,

with heating and cooling rates held to 1C/min. All sintering was inside a rectangular alumina crucible with a loose fitting plate for a lid. The crucible was pre-seasoned with approximately 20 grams of powder from a similarly prepared batch at 1300C for 72 hours. Two pellets at a time were placed in the seasoned crucible and covered below and above with approximately 15 grams of powder from the same batch with the binder already removed. The pellets were sintered at temperatures from 1200C to 1360C and held at peak temperature for between 15 minutes and 4 hours.

The sintered pellets were then mounted on a sample holder using crystal bond (crystal bond 821-1, Ted Pella, Inc.) for grinding and polishing. The grinding process consisted of removing material via wet sanding on a turntable with a five step process, sequentially using P400, P800, P1200, P2400, and finally P4000 sand papers (140/0806,140/0903,30-51288,30-5108-600-102 from Buehler and #50-10040 from Allied High Tech Products, Inc., respectively). The polishing consisted of using colloidal diamond media sequentially in a 6 step process using 30um, 9um, 6um, 3um, 1um, and 0.25 um (#90-3004 and #90-30030 from Allied High Tech, Inc., 632/456307 and 633/456875 from Buehler, #90-30015 from Allied High Tech, Inc., and 40-8240 with 40-6016 suspension from Buehler respectively). Final polishing was achieved using 0.02 um colloidal silica (3180-40015 from Allied High Tech, Inc.).

X-ray Diffraction (XRD) measurements were taken at room temperature on a Bruker D-8 at the University of Kentucky. X-ray Photo-spectrometry (XPS) measurements were performed on a K-Alpha at Lexmark International. Scanning Electron Microscope measurements were made on a Hitachi SEM 4300 at the University of Kentucky.

6.2. Sintering Results and XRD Characterization

This method of synthesizing $Li_5La_3Ta_2O_{12}$ samples was done at higher temperatures than previously reported, but is close to the reported sintering conditions of recent literature.[5-8,23,24,34,35] The motivation for this was two-fold - to achieve high density pellets that could then undergo significant surface polishing for the in-situ nanoscale transport measurements detailed in Chapter 5 as well as an attempt to vary the grain sizes. The in-situ nanoscale transport measurements required pellets with minimal surface roughness in order for the AFM tip to be able to be able to properly characterize the grains and to confidently assume the surface is free from contaminants, as well as to facilitate the measurements. Ultimately, the synthesis routes attempted proved successful in regards to synthesizing dense enough samples for the nanoscale transport measurements. The attempts to vary the grain sizes of the samples did not yield samples with mechanical properties sufficient to undergo any processing for further characterization that had an appreciable variation in grain size. The samples that were used for further characterization presented here and in Chapter 7 were low-yield and required significant processing to achieve a sample of good phase purity and quality.

An XRD scan of the powder after calcination at 700C is shown in Fig. 6.1. The peaks of this X-ray scan do not fit entirely with a single phase, but most of the peaks do fit $LiLa_2TaO_6$ with the remaining peaks unidentified. This synthesis route of calcining to the intermediate phases of Fig.

6.1 was found to be a successful route to final synthesis of high quality ceramic pellets. Attempts to sinter the samples from a precursor powder that had undergone calcination to the correct phase proved unsuccessful, as well as calcination to other intermediate phases. It is believed that the high temperatures needed to approach the successful sintering of this material were sufficient to allow for too much lithium loss to achieve the desired final phase. Therefore, an alternative approach of calcination to the intermediate phases was employed, with the phase(s) displayed in Fig. 6.1 proving to be the successful intermediary to high quality samples. The conditions for the calcination to the intermediate phase were chosen based on prior work on this material.[5-8,23,24,34,35]

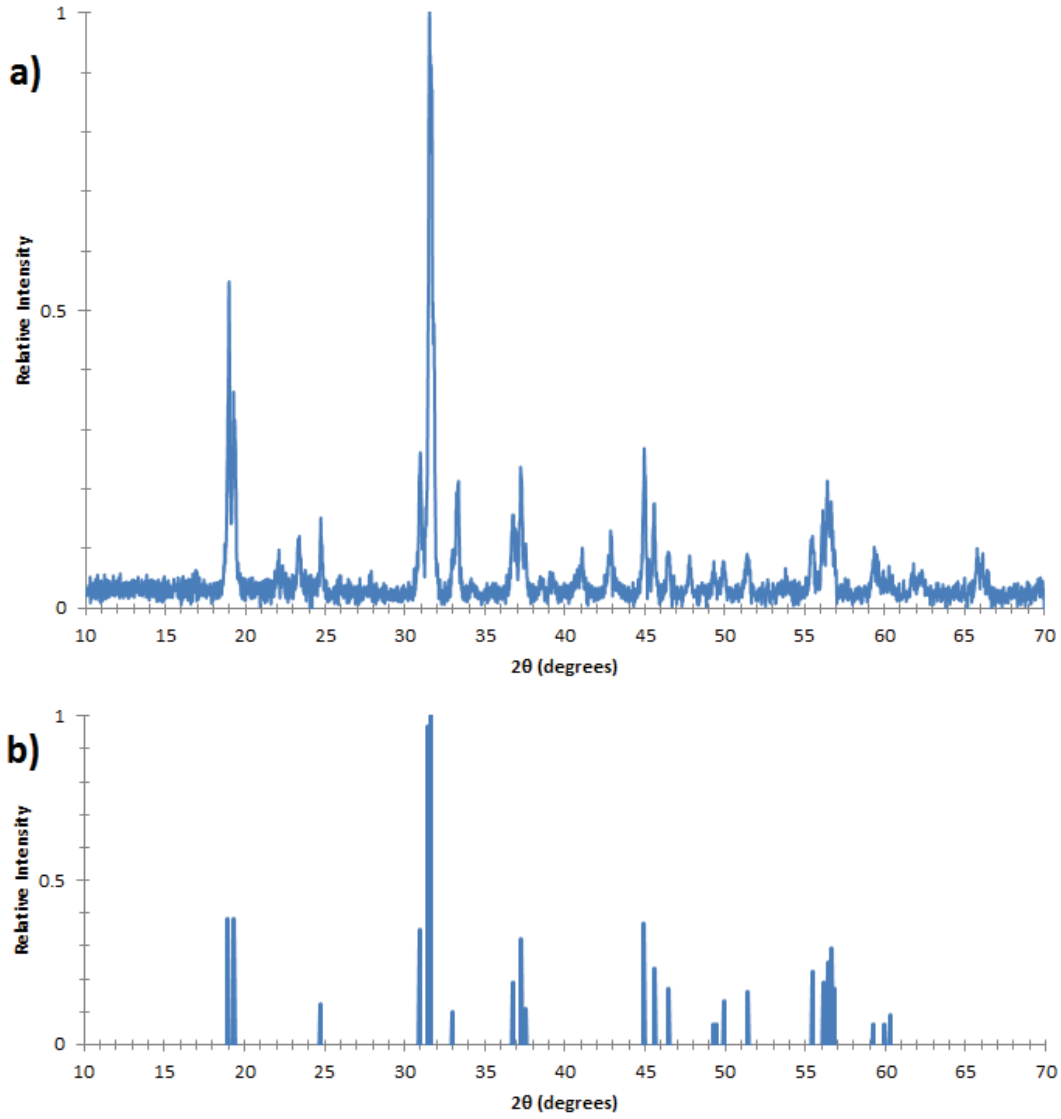

Figure 6.1:a) XRD scan of typical batch after calcination at 700C for 8 hours, plotted with relative intensity, peak intensity was 875 counts
b) ICSD pattern #00-039-0897 for $LiLa_2TaO_6$, for all peaks above 5% relative intensity for 2θ = 10 degrees to 2θ = 60 degrees

The final sintering conditions were varied from 1100C to 1380C, with melting occurring between 1365C and 1380C for this material. Upon melting, it was observed that there was significant reaction with the alumina crucible, which may have served as a flux for the melting, and so 1380C may be below the actual melting point for $Li_5La_3Ta_2O_{12}$.

An ideal mix of correct phase, high density, and suitable mechanical properties to undergo further processing was achieved at 1340C for 30 minutes with approximately 10 grams of

powder surrounding each pellet during sintering. The density of these pellets after they were polished, measured using the Archimedes method, was between 91% and 96% of the theoretical density of 6.36g/cm^3. Fig. 6.2 below shows an XRD scan of a sample.

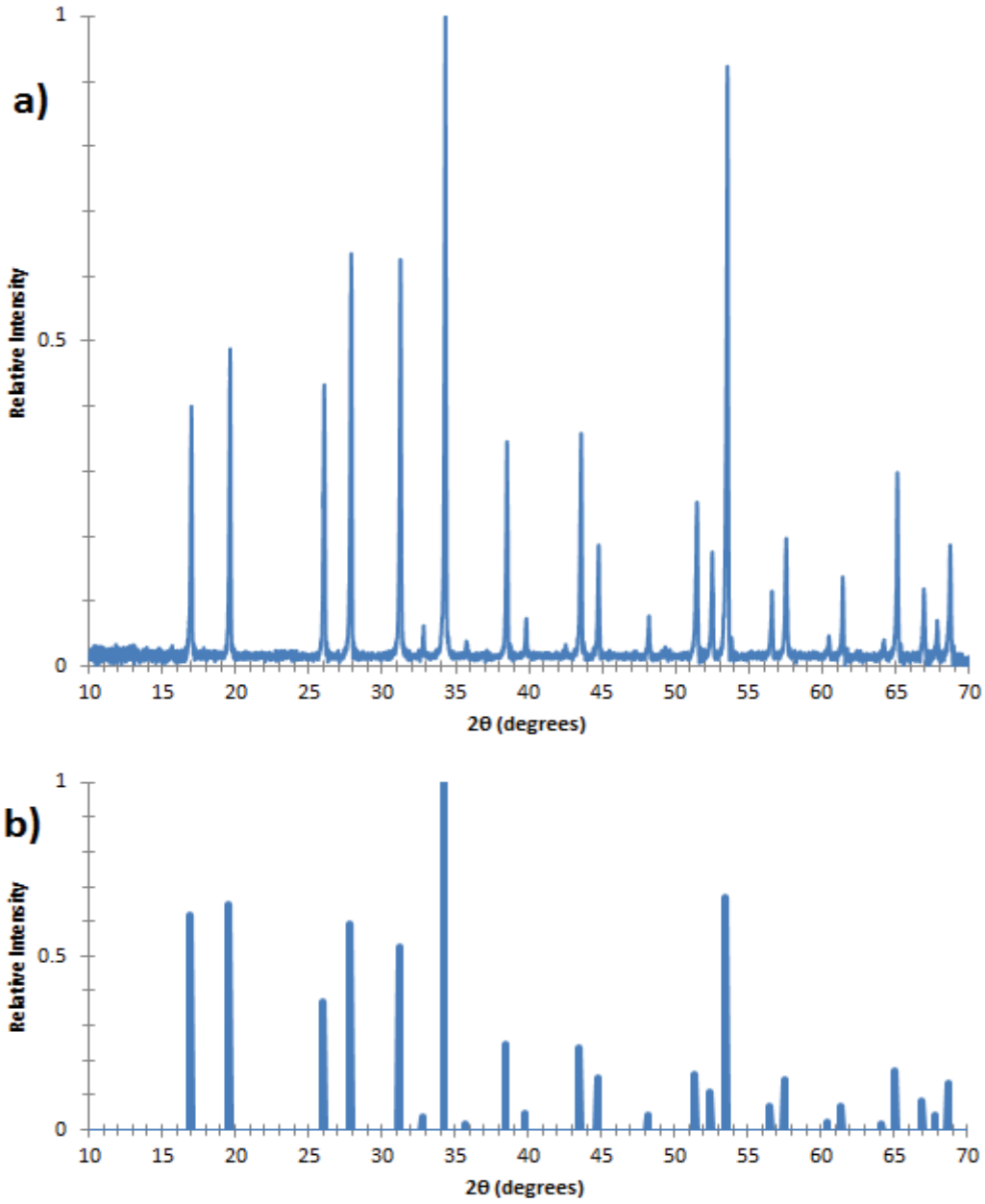

Figure 6.2:a) XRD scan of typical crushed pellet after sintering at 1340C for 30 minutes and polishing, plotted with relative intensity, peak intensity was 1577 counts
b) ICSD pattern #01-074-9856 for $Li_5La_3Ta_2O_{12}$, for all peaks above 1% relative intensity for 2θ = 10 degrees to 2θ = 70 degrees

In addition to the desired phase, an impurity phase was also present in the sintered ceramics. The distribution of this impurity phase was concentrated on the surfaces of the sintered pellet.

Grinding and polishing away the outer 25% to 70% of the sintered pellets yielded samples with only the desired phase present. The nominal pellet thickness was 1.3mm after sintering, with variation between 1.15mm and 1.45mm. Successful sintering was achieved with pellets in this range, but proved unsuccessful with other sizes of pellets. The nominal thickness of a sample with high phase purity after grinding and polishing was between 0.35 and 1.00 mm. Thinner initial pellets did not have a pure phase when the outer surfaces were ground away leaving a pellet of thickness of 300 microns, which proved to be the lower limit of pellets that could be successfully handled. Thicker initial pellets did not sinter to the correct phase and also exhibited distortion. Fig. 6.3 shows an XRD scan of the unpolished surface of a typical pellet, sample number 206-09, after sintering to 1340C for 30 minutes with the corresponding powder diffraction file. The pellet was rotated several times and did not exhibit any signs of crystallographic correlation between grains. Previous reports on the synthesis of this material have identified a lithium poor and lanthanum rich phase, $LiLa_2TaO_6$, as an impurity phase that arises from sintering at temperatures above 950C.[5] Note the significant peak between 15 and 16 degrees in Fig. 6.3a and that that peak is not identified with $LiLa_2TaO_6$, as shown in Fig. 6.2b, as well as other differences between the scan in Fig. 6.3a and the pattern of $LiLa_2TaO_6$ in Fig. 6.2b.

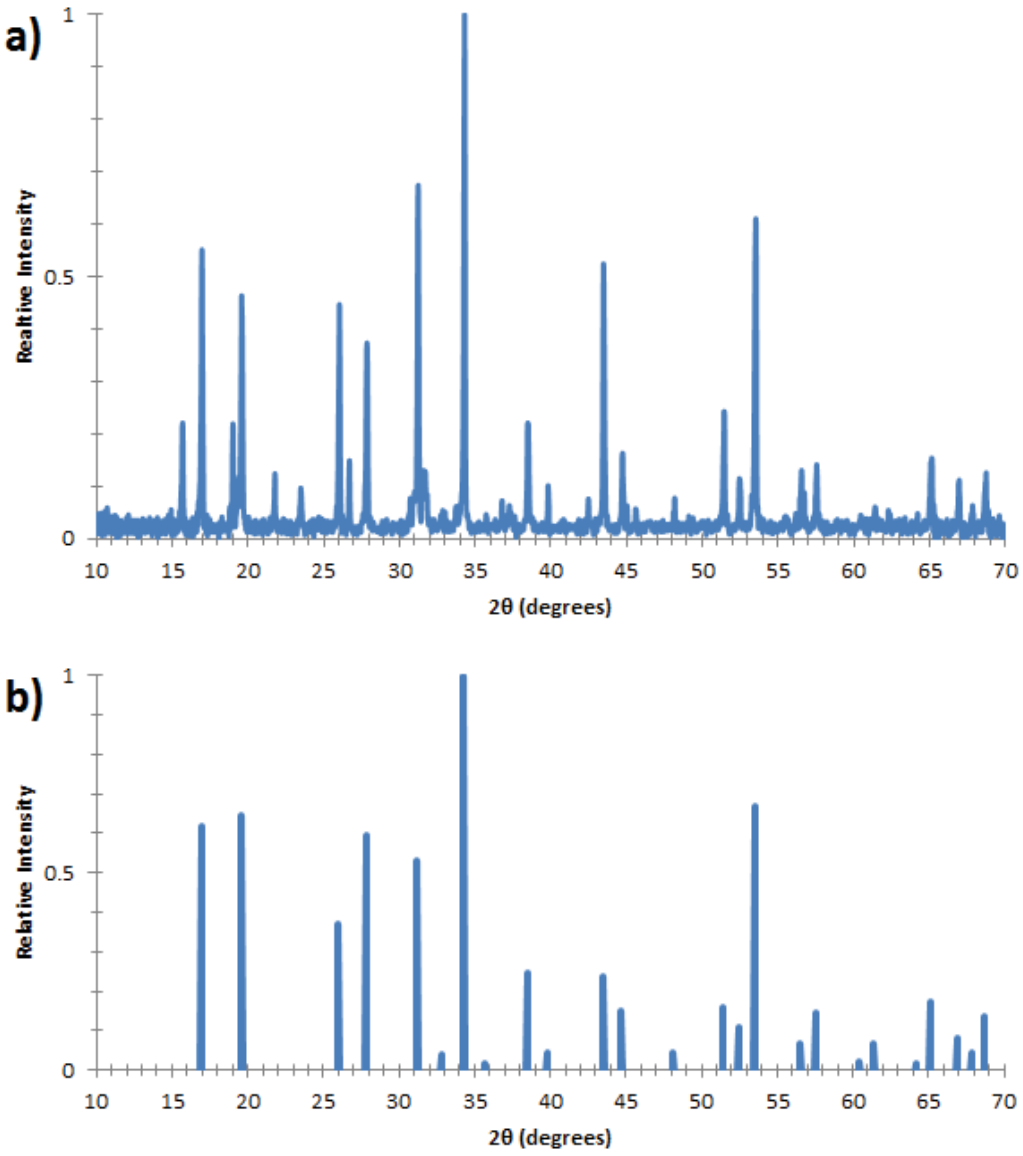

Figure 6.3:a) XRD scan of the surface of pellet 206-09 after sintering at 1340C for 30 minutes, plotted with relative intensity, peak intensity was 642 counts
b) ICSD pattern #01-074-9856 for $Li_5La_3Ta_2O_{12}$, for all peaks above 1% relative intensity for 2θ = 10 degrees to 2θ = 70 degrees

The desired phase plus an impurity phase is clearly visible in Fig 6.3a. The surface of pellet 206-09 was then ground, removing 140 microns of material, and then polished. Fig. 6.4 shows the XRD scan of the surface after this initial preparation.

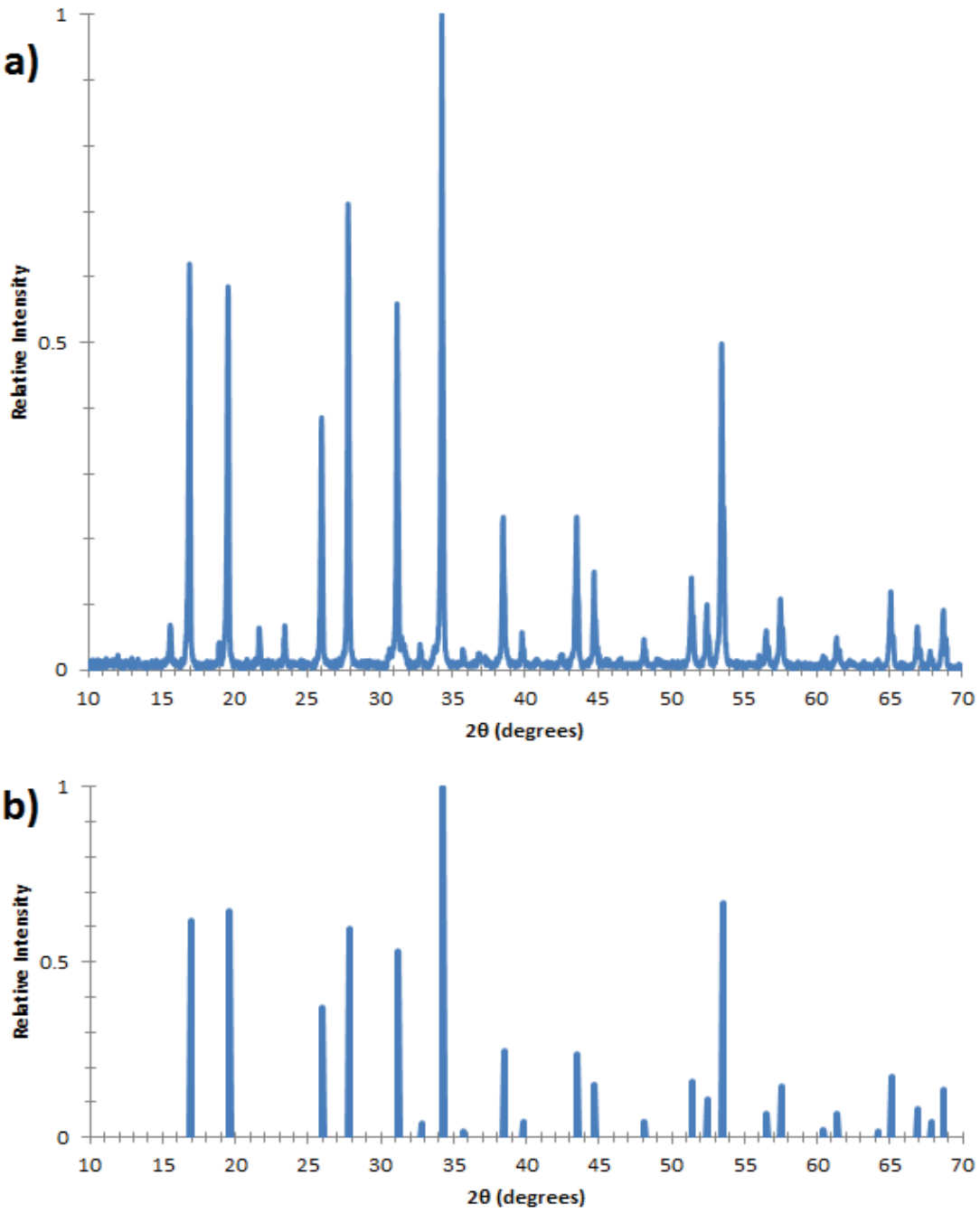

Figure 6.4:a) XRD scan of the surface of pellet 206-09 after sintering at 1340C for 30 minutes with the top 140 microns of surface ground away, plotted with relative intensity, peak intensity was 2868 counts
b) ICSD pattern #01-074-9856 for $Li_5La_3Ta_2O_{12}$, for all peaks above 1% relative intensity for 2θ = 10 degrees to 2θ = 70 degrees

The surface of the pellet was ground down an additional 160 microns and then polished. Then an XRD scan was taken, shown in Fig. 6.5a below along with the corresponding powder

diffraction file in Fig 6.5b. As can be seen in Fig 6.5, no impurity phase is detectable on the top surface of pellet 206-09. This process was repeated for the bottom surface.

A different pellet that was similarly prepared to be phase pure on both sides was then crushed and an XRD scan was taken, shown above in Fig. 6.2. This was done to verify that it was phase pure throughout, within the detection limits of XRD.

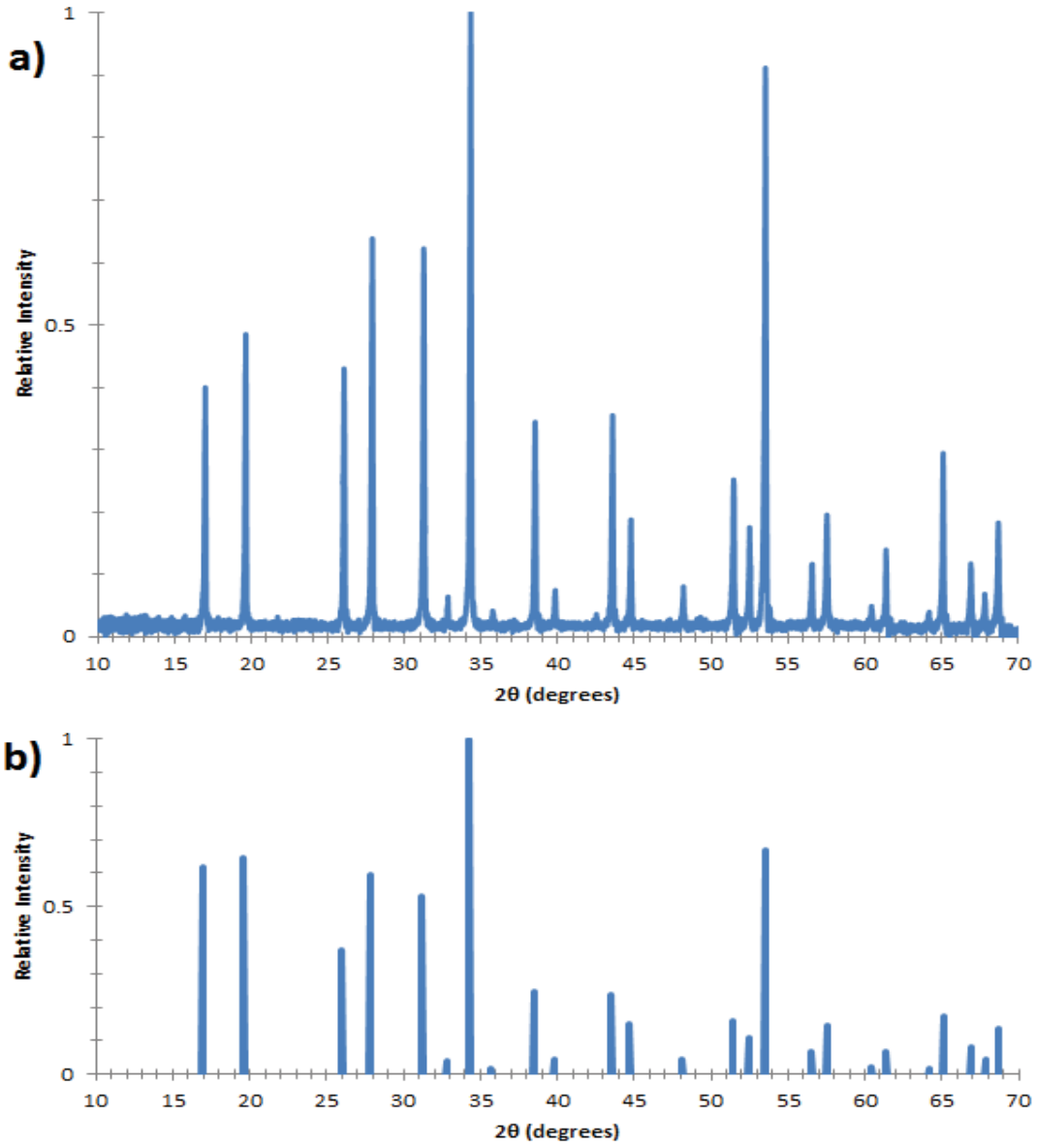

Figure 6.5:a) XRD scan of the surface of a pellet 206-09 after sintering at 1340C for 30 minutes with the top 300 microns of surface ground away, plotted with relative intensity, peak intensity was 1609 counts
b) ICSD pattern #01-074-9856 for $Li_5La_3Ta_2O_{12}$, for all peaks above 1% relative intensity for 2θ = 10 degrees to 2θ = 70 degrees

Factors that were found to affect the amount of the impurity phase present in the final sample were sintering temperature and time, the thickness of the pre-sintered pellets, the amount of powder in which the pellets were embedded, and the history of the crucible used. The alumina crucible used for sintering required high temperature curing with the parent powder to minimize the amount of lithium lost on subsequent sintering. After approximately 10 sintering cycles the crucible would need to be replaced as it would bow and distort from the lithium absorption.

The results of the sintered pellets in different environments and at varying temperatures and times were not always quantifiable. If the impurity phase present was too significant, the pellets experienced significant distortion to the point that they could not be processed and further characterized. Additionally, as the sintering conditions were varied, the mechanical properties of the pellets varied to such a degree that many samples could not be characterized beyond initial XRD analysis. At lower temperatures, the samples did not achieve enough densification during sintering and would disintegrate upon processing.

At higher sintering temperatures and/or longer dwell times, there appeared to be uncontrolled grain growth and the samples would disintegrate upon handling. Texture analysis of such pellets revealed high crystallographic orientation and optical microscopic analysis revealed some grains as large as approximately 50 microns. These samples could not undergo any handling or preparation beyond texture analysis with XRD before completely disintegrating.

6.3 SEM and XPS Characterization

Fig. 6.6 below shows an SEM image of the fractured surface of a pellet, with nominal grain size of three to five microns. Fractured surfaces gave the best resolution of grain sizes, as polished surfaces that were then thermally etched to 700C to reveal the grains also developed the impurity phase shown in Figs 6.3 and 6.4 at levels significant enough to be seen on XRD. A thin layer of gold-palladium was evaporated onto the surfaces of all samples before SEM measurements were taken to prevent electrical charge buildup on the samples.

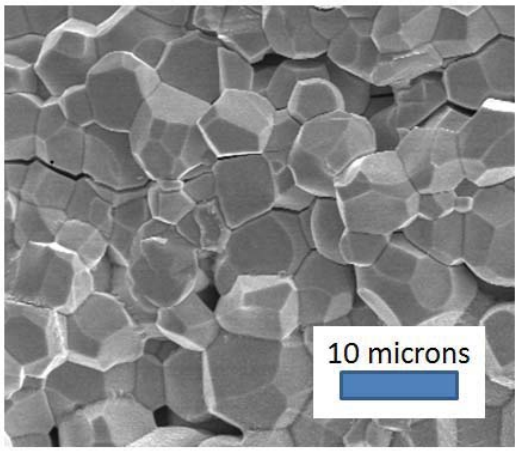

Figure 6.6: SEM image with x450 magnification of the fractured surface of pellet 204-09

A surface film was observed on several samples after final polishing, but no impurity phase was confirmed via XRD. No impurity phase was detected on the XRD scans, and the contaminant film was believed to be below the detection limits of EDX when SEM images were taken, shown in Fig. 6.7 below. The film was observed to grow within 6 to 24 hours after final polishing, and produced a characteristic diffraction of optical light when observed under low power optical microscopic resolution. Attempts to eliminate the growth of the film by preserving samples in desiccated chambers and at elevated temperatures proved unsuccessful. The only means of preventing the growth of the film was to treat the surface of the samples with acetone followed by methanol via soft abrasive while inside an argon glove-box with O_2, CO_2, and H_20 levels below the detectable limits of 0.1 ppm.

Ultimately, this contaminate film was found to be correlated with samples synthesized with 10% excess lithium in the initial batch. Samples made with 8% excess lithium did not show signs of this contaminant film. In-situ nanoscale transport measurements on the surface of these samples, detailed in Chapter 7, confirm the absence of the contaminant film on samples made with 8% excess lithium and its presence on samples with 10% excess lithium. Additionally, samples were made with 5%, 12%, and 15% excess lithium. The 5% excess batch did not have enough of the correct phase present when sintered to conditions necessary to achieve visible densification. The 12% excess lithium samples had an additional impurity phase present in significant quantity which was not identified. The 15% excess lithium samples did not achieve densification with the correct phase present.

a)

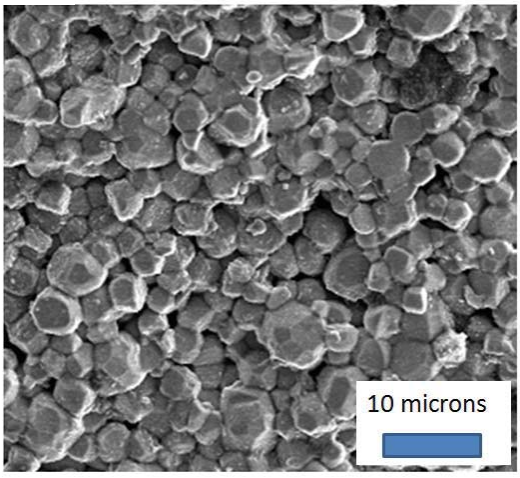

b)

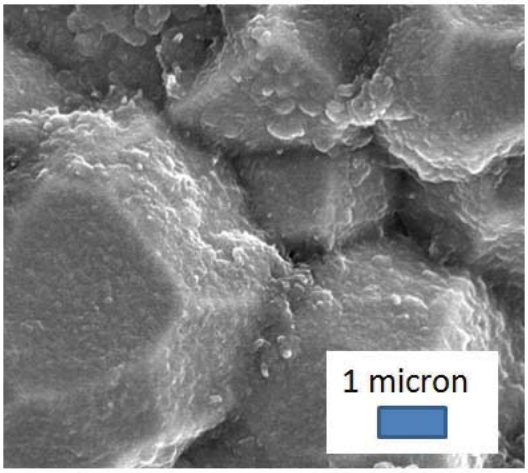

Figure 6.7: a)SEM image with x100 magnification of the fractured surface of pellet 203-10 with the presence of a contaminant film on the grains (note this sample was less dense than previous samples)
b) same sample with x4500 magnification

A sample with the film present was analyzed via XPS. The surface was initially scanned, and then an ion beam was used to etch the film away, and the surface was analyzed again. A survey scan of the surface before it was etched is shown in Fig 6.8 below.

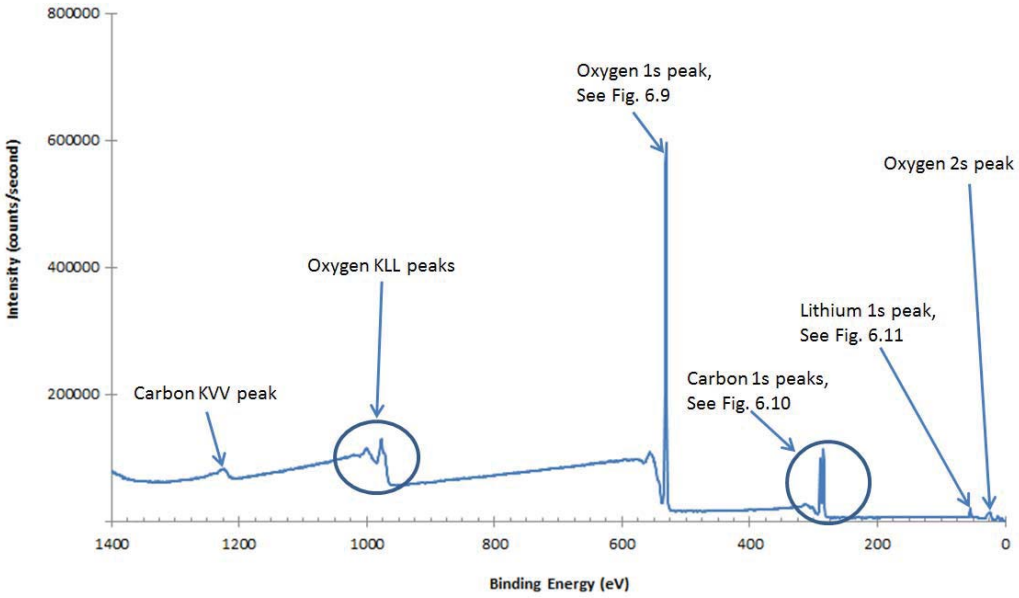

Figure 6.8: XPS survey scans of pellet 213-15 with contaminant film prior to surface etching. Peaks identified with Oxygen 1s, Carbon 1s, and Lithium 1s are shown in Figs. 6.9, 6.10, and 6.11 respectively. Sum of 5 scans in 1.0 eV steps

Note that no peaks associated with Lanthanum or tantalum are present, indicating that the entire surface with the 400 micron by 400 micron scan area is covered with the contaminate film, within the detection limits.

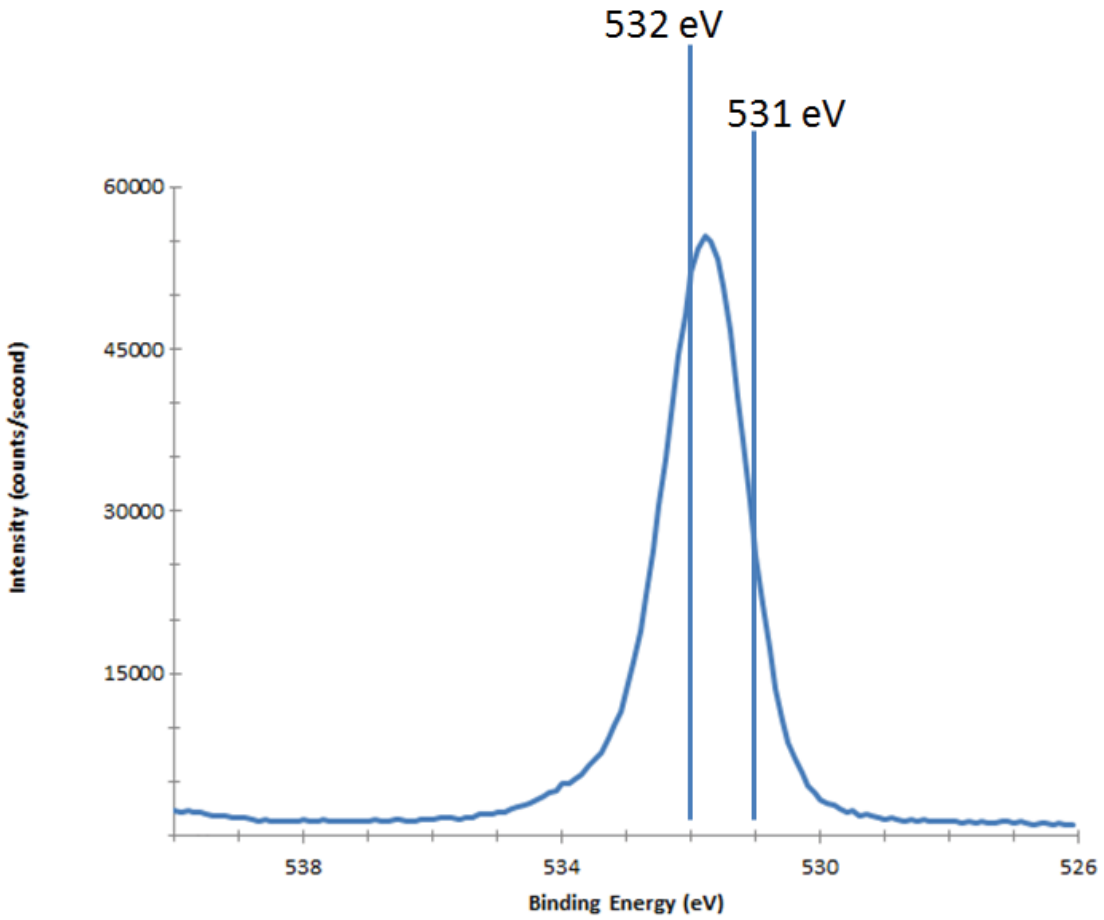

Figure 6.9: XPS scans of oxygen 1s peak of pellet 213-15 with contaminant film prior to surface etching. Sum of 6 scans in 0.1 eV steps

The peak location in Fig. 6.9 is between 531 eV and 532 eV, which is consistent with oxygen bonded with either carbonate or hydroxide.

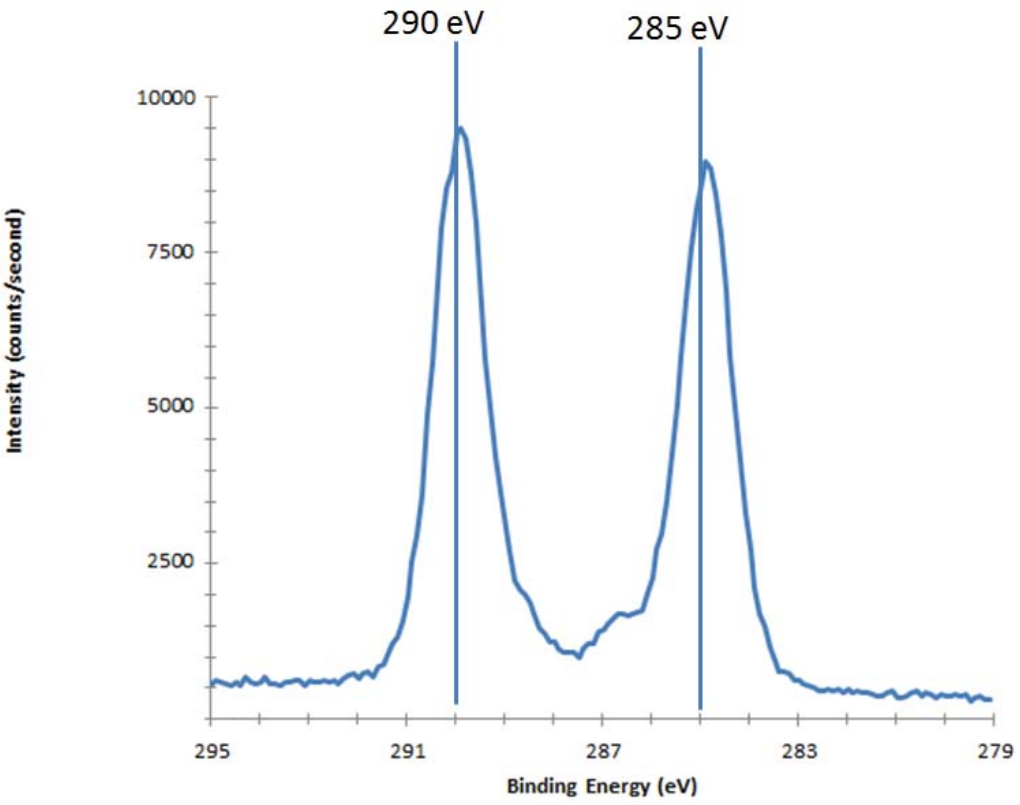

Figure 6.10: XPS scans of carbon 1s peak of pellet 213-15 with contaminant film prior to surface etching. Sum of 8 scans in 0.1 eV steps

In fig 6.10, there are two clearly resolved peaks. The peak just below 285 eV is consistent with carbon-hydrogen bonds and the peak just below 290 eV is consistent with carbonate bonds.

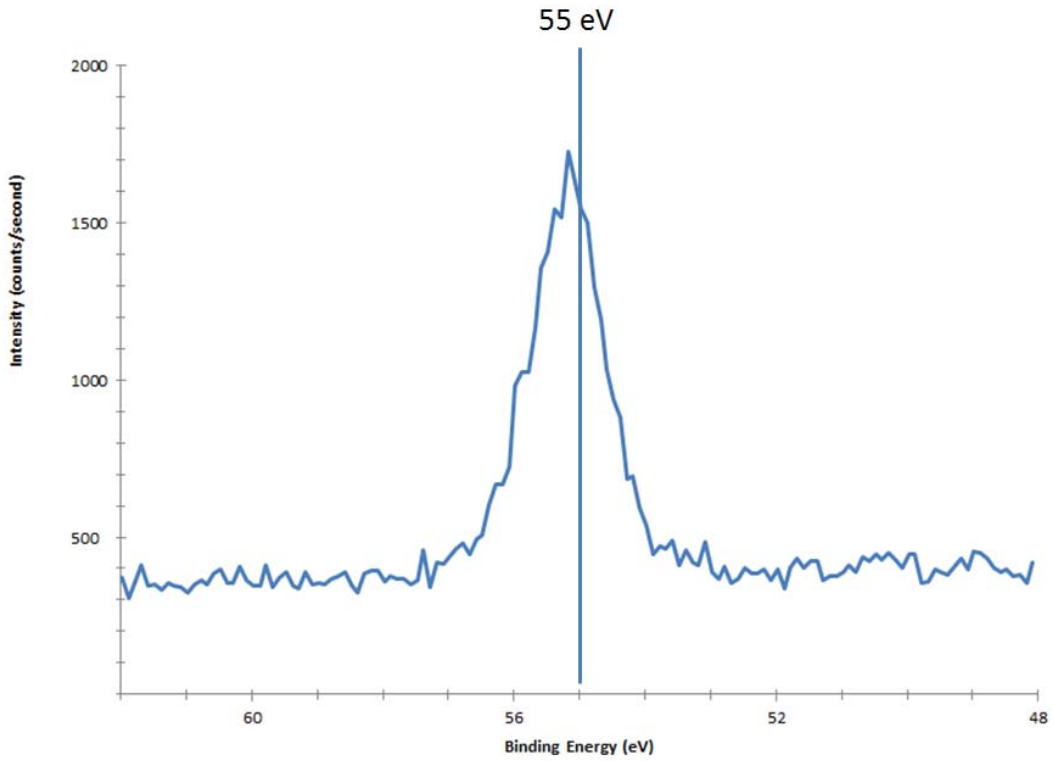

Figure 6.11: XPS scans of lithium 1s peak of pellet 213-15 with contaminant film prior to surface etching.

Note that the lithium 1s peak has shifted to a slightly higher binding energy than 55 eV, which is indicative of lithium carbonate. This peak location is at a higher binding energy than what is seen with lithium hydroxide, which peaks below 55 eV. The XPS scans in Figs. 6.8 through 6.11 identify the contaminant film as lithium carbonate. Additionally, the XPS scans of the surface with the contaminant film identify the presence of an organic alcohol. The presence of the alcohol is suspected to be the result of solvents used to remove the sample from the crystal bond used for polishing. It is worth mentioning that the contaminant film was observed on surfaces that were polished with aqueous suspensions and the sample was left bonded to the holder to preserve it from exposure to organic solvents.

The surface of the sample was then etched for 780 seconds with a focused argon beam, intensity set to medium. Fig. 6.12 shows the XPS survey scans. The argon etching versus was not calibrated with a known depth, but the etched are was found to be less than 10 microns different in height from an unetched area. Nanoscale transport measurements in Chapter 7 reveal the estimated height of the contaminate film.

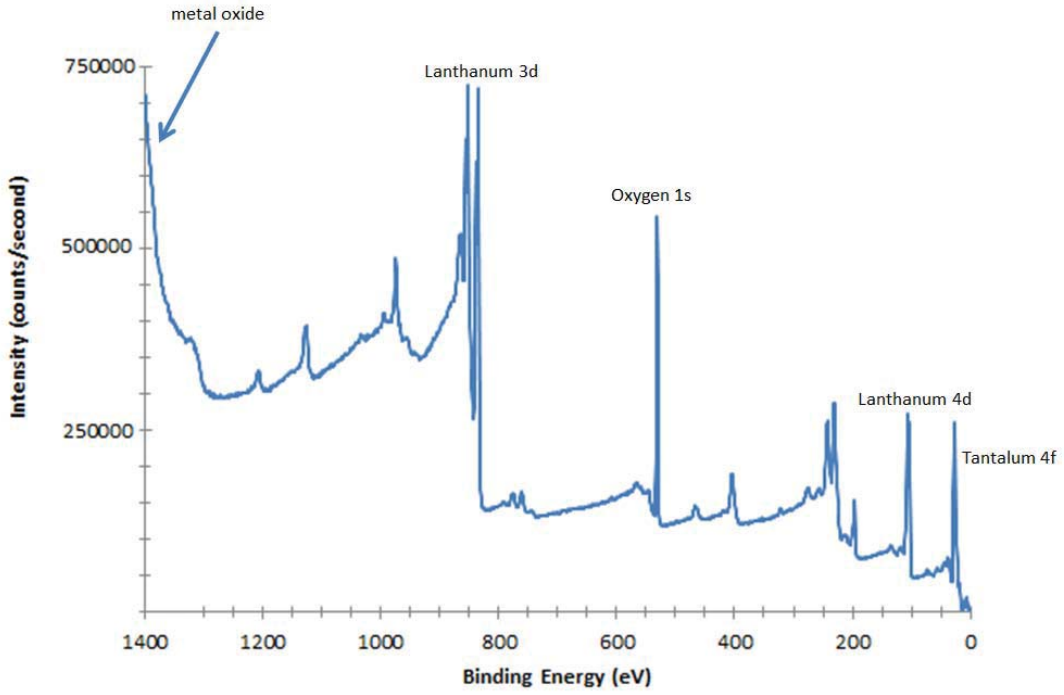

Figure 6.12: XPS survey scans of pellet 213-15 with contaminant film post surface etching. Sum of 3 scans in 1.0 eV steps

In Fig. 6.12, many new peaks emerge, when compared against fig. 6.8. Additionally, the two carbon peaks seen in Fig 6.10 are now absent. That area is analyzed further in Fig. 6.13 below.

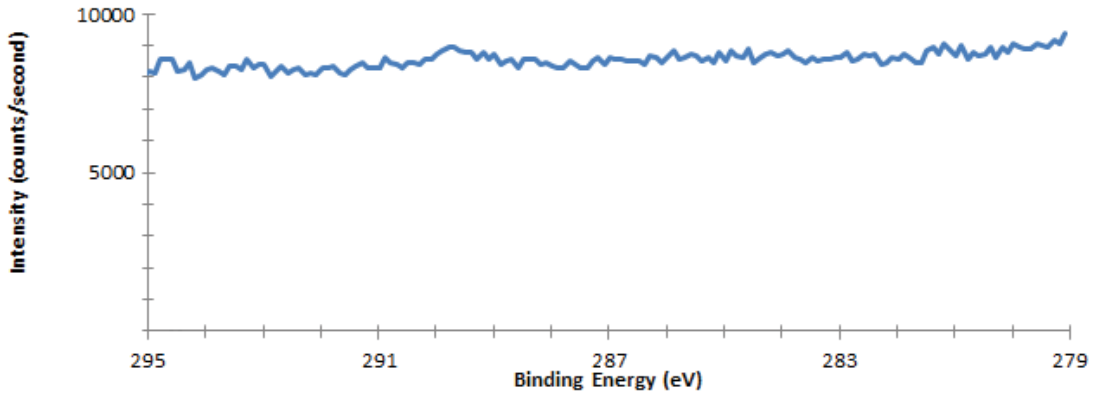

Figure 6.13: XPS scans of location of carbon peaks in Fig. 6.10 of pellet 213-15 with contaminant film post surface etching. Sum of 8 scans in 0.1 eV steps

The carbon peaks that were seen in Fig. 6.10 are no longer present in Fig. 6.13, with the potential exception of possibly a peak between 289 and 290 eV where the carbonate peak was in Fig. 6.10. This, along with the presence of tantalum and lanthanum and XRD results of the sample indicate the lithium carbonate contaminate film, as well as any organic alcohols, has been etched away and the exposed surface is $Li_5La_3Ta_2O_{12}$.

Recent literature has also confirmed the presence of absorbed carbonate species in samples of $Li_5La_3Ta_2O_{12}$ made via the traditional synthesis routes of previous reports for this material and identified it using Fourier Transform Infrared Spectroscopy (FTIR), see Fig. 6.12 below.[57]

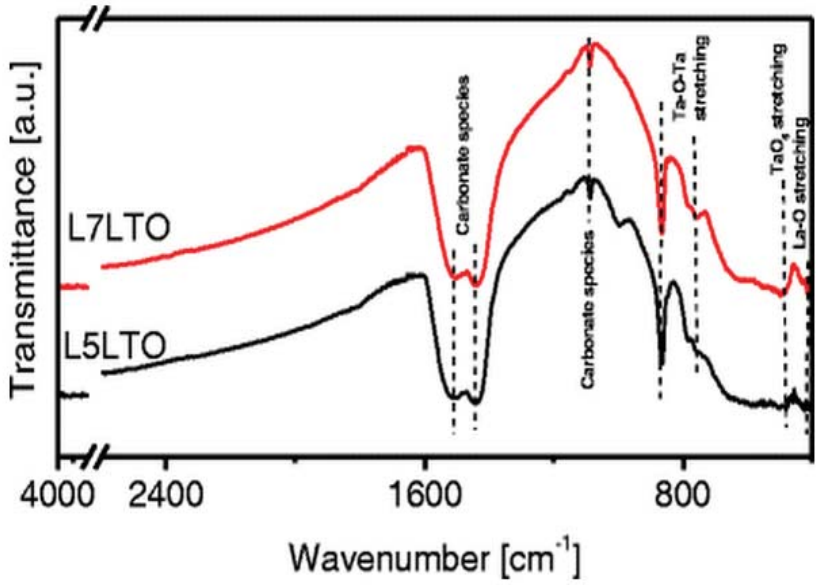

Figure 6.14: FTIR spectra of $Li_5La_3Ta_2O_{12}$(L5LTO) and $Li_7La_3Ta_2O_{12}$ (L7LTO) [57]

6.4 Summary of Synthesis and Compositional Characterization Results

In summary, a new sintering method was developed at higher sintering temperatures than previously reported. This method was low yield and required significant sample processing to achieve samples with phase purity. This synthesis route yielded samples with densities of up to 96% that could withstand the surface preparation needed for subsequent nanoscale transport measurements. Attempts to modulate the sizes of the grains did not yield samples with sufficient mechanical properties to withstand sample processing and grain sizes that significantly deviated from 4 microns. A contaminate film was identified as lithium carbonate on samples made with 10% excess lithium, but not on samples made with 8% excess lithium.

7.0 Results of Ionic Transport Measurements and Analysis of Equivalent Circuits

The results of the ionic transport measurements as well as the analytical and numerical solutions to the equivalent circuits used to interpret the ionic transport measurements are presented here in Chapter 7. This portion of the research has the most inherent ambiguity, and there can be multiple interpretations that fit within in the context of one of the models or assumptions presented. These ambiguities are pointed out whenever possible.

7.1 Experimental Setup

AC impedance spectroscopy was performed on an Agilent E4980A from 20Hz to 2MHz at the University of Kentucky. Gold electrodes (TC8101 from Heraeus, Inc.) were applied to the surfaces of a polished pellet and subsequently cured at 700C for 8 hours. For elevated temperature measurements, the samples were held at temperature for 1 hour before they were tested. Atomic Force Microscope (AFM) measurements were performed at Oak Ridge National Lab's Center for Nanophase Materials Science (CNMS) on an Asylum Research Cypher with ARC controller in an MBraun glove box with ultra-high purity argon using platinum coated on chromium conductive probes (Multi75E-G from Budget Sensors, Inc.). The current was collected on a current amplifier (DLPCA-200 by Femto, GmbH). Data was acquired using high speed data acquisition cards (NI-PXI-5412 and NI-PXI-5122 by National Instruments, Inc.) AFM topography results were analyzed with WSxM.[58] In-situ nanoscale ionic transport measurements were analyzed on codes written at CNMS in Matlab.[59]

7.2 AC Impedance Spectroscopy Results

Three AC Impedance Spectroscopy results are presented below in figs 7.1 through 7.3. Fig. 7.1 represents a sample made with 10% excess lithium and a density of 90% at 20C. Fig. 7.2 shows the AC impedance spectroscopy of a sample made with 8% excess lithium and a density of 94% at 22C. Fig. 7.3 shows the AC impedance spectroscopy of a same sample from Fig 7.2 at 75C. Additionally, Fig. 7.2 shows the response at multiple applied voltage levels to demonstrate the linearity of the response around the nominal applied voltage levels of 100mV.

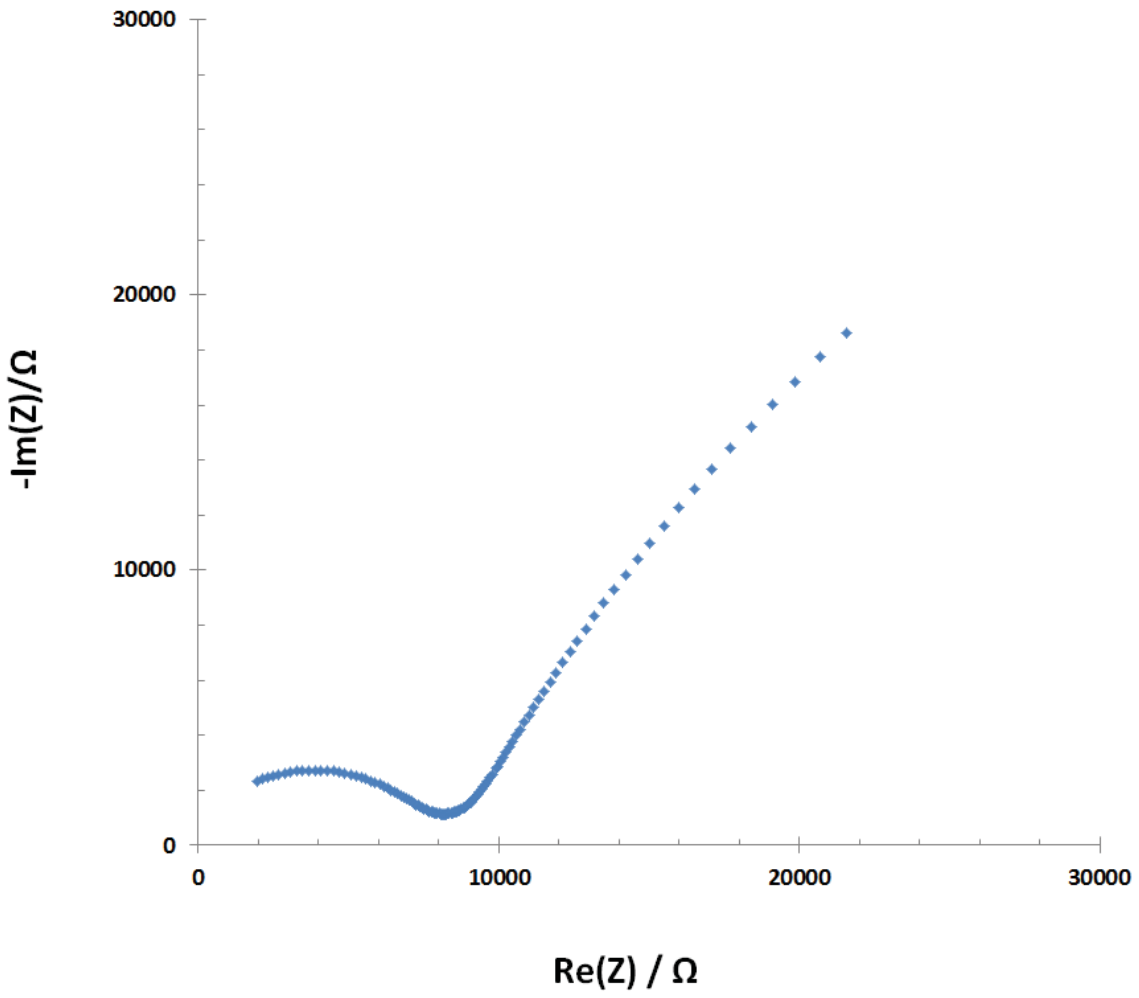

Figure 7.1: AC impedance spectroscopy response of sample 206-10 at 22C with a 100mV applied signal

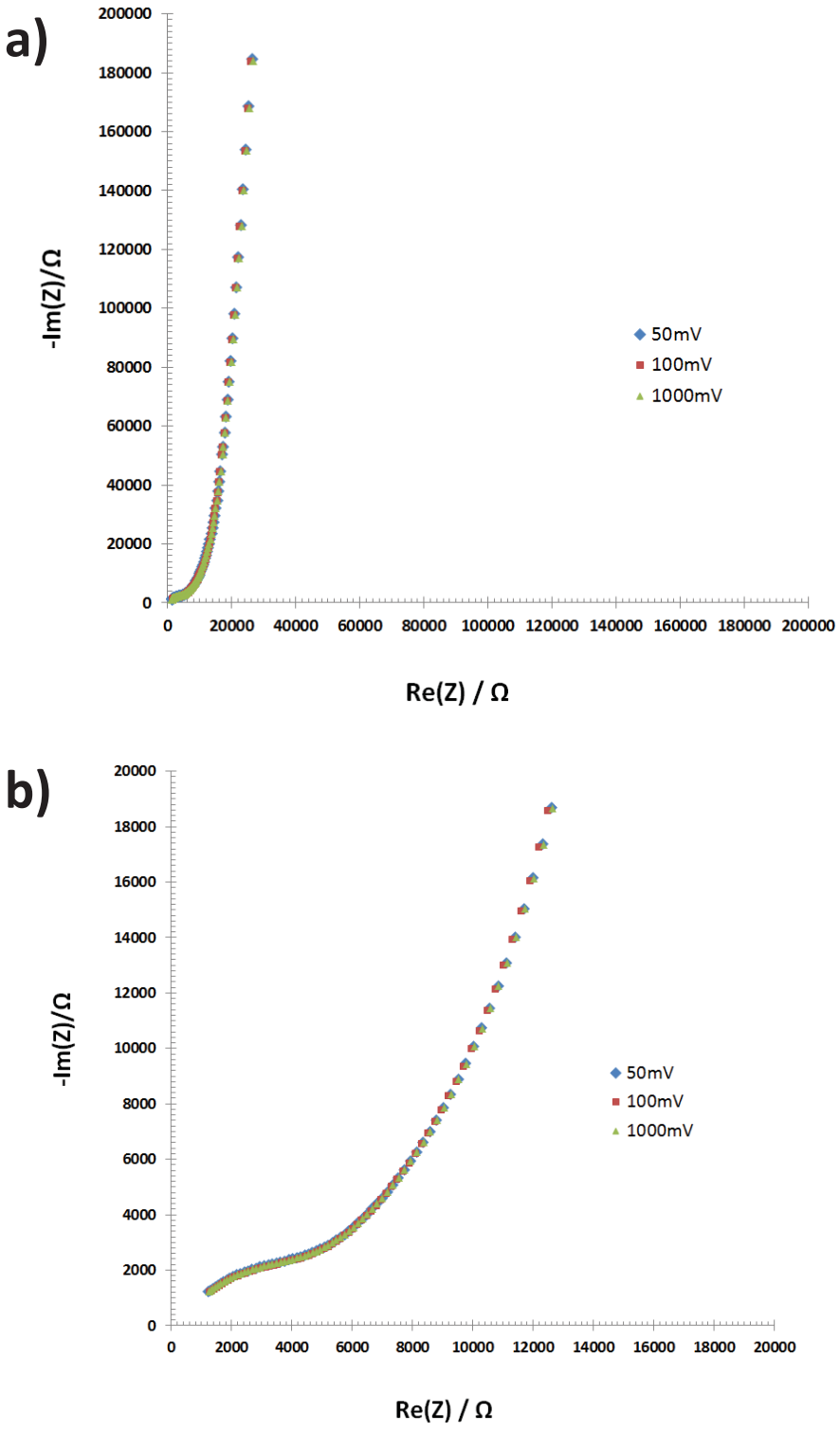

Figure 7.2: a) AC impedance spectroscopy response of sample 209-17 at 22C with a 50mv, 100mV, and 1V applied signal **b)** zoomed in view of a)

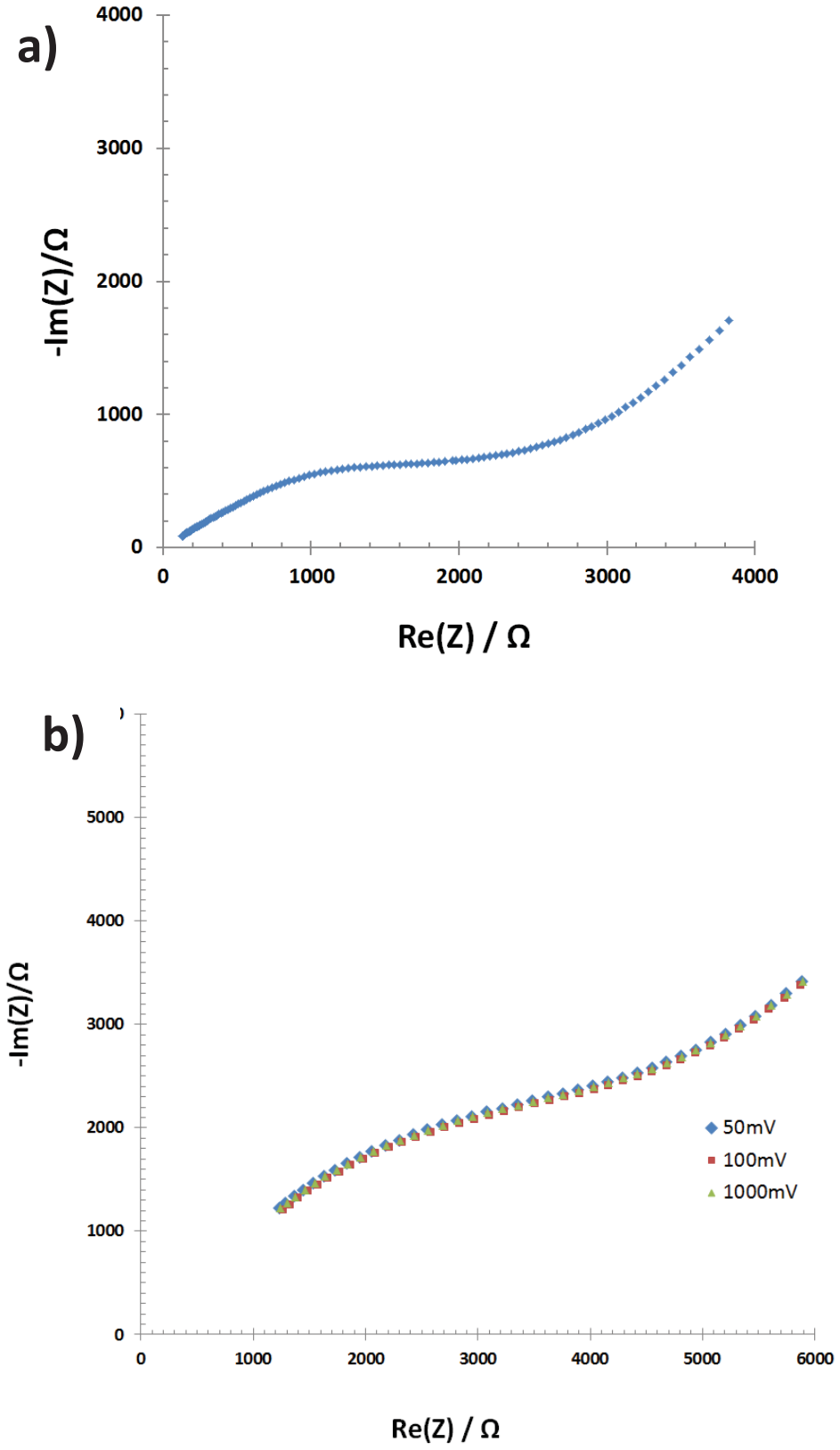

Figure 7.3: a) AC impedance spectroscopy response of sample 209-17 at 75C with a 100mV applied signal **b)** zoomed in view of Fig 7.2b for comparison

A clear minimum is present in Fig. 7.1. Figs 7.2b and 7.3a do not have a minimum in the impedance spectroscopy response. Fig7.3b is included to demonstrate the similarity of the responses of the system at 22C to the response of the system at 75C.

7.3 Responses of Equivalent Circuits

When analyzing the response of these solid electrolyte systems here and in reported data, it should be noted again that the real impedance is a monotonically decreasing function with increasing frequency, but that local minima and maxima can be observed in the negative imaginary part of the complex impedance versus frequency. As such, the response of the negative imaginary part of the complex impedance versus frequency is of particular interest in these equivalent circuits.

The response of equivalent circuit 5.3 can be solved analytically to yield equations 7.1 through 7.5 below.

$$\textbf{Re [Z}(\boldsymbol{\omega C})\textbf{]} = \frac{R}{(\xi^2 R^2)(\boldsymbol{\omega C})^2 + (1+\xi)^2} \qquad \text{equation 7.1}$$

$$\textbf{-Im [Z}(\boldsymbol{\omega C})\textbf{]} = \mathbf{g}(\boldsymbol{\omega C}) = \frac{\left(\xi R^2\right)(\boldsymbol{\omega C})^2 + (1+\xi)}{\left(\xi^2 R^2\right)(\boldsymbol{\omega C})^3 + (1+\xi)^2(\boldsymbol{\omega C})} \qquad \text{equation 7.2}$$

$$\frac{\boldsymbol{\partial g}(\boldsymbol{\omega C})}{\boldsymbol{\partial}(\boldsymbol{\omega C})} = \frac{-(\xi^3 R^4)(\boldsymbol{\omega C})^4 + (1-\xi-2\xi^2)(\xi R^2)(\boldsymbol{\omega C})^2 - (1+\xi)^3}{(\xi^4 R^6)(\boldsymbol{\omega C})^6 + 2(\xi^2 R^4)(1+\xi)^2(\boldsymbol{\omega C})^4 + R^2(1+\xi)^2(\boldsymbol{\omega C})^2} \qquad \text{equation 7.3}$$

$$(\boldsymbol{\omega C})^{\mathbf{2}}_{\boldsymbol{maximum}} = \left(\frac{1}{2\xi^2 R^2}\right)\left[(1-\xi-2\xi^2) + \sqrt{(1-6\xi-15\xi^2-8\xi^3)}\right] \qquad \text{equation 7.4}$$

$$(\boldsymbol{\omega C})^{\mathbf{2}}_{\boldsymbol{minimum}} = \left(\frac{1}{2\xi^2 R^2}\right)\left[(1-\xi-2\xi^2) - \sqrt{(1-6\xi-15\xi^2-8\xi^3)}\right] \qquad \text{equation 7.5}$$

The exact frequency that corresponds to the extremum of equations 7.4 and 7.5 depends on the value of the capacitance, C. Note that the response of the circuit depends on the frequency, ω, coupled with the capacitance, C, and not either term individually. Therefore, all solutions are against the relative frequencies, ωC, and are shown in Table 7.1 below. There will be a single local minima and maximum in the imaginary response of the impedance versus frequency if ξ is less than 0.125, a single point of inflection for ξ = 0.125, and no local extremum for larger values of ξ. The results for the local minimum and maximum are summarized in Table 7.1 below.

Table 7.1: Solutions to the local minimum and maximum for the imaginary response versus frequency of the complex impedance of equivalent circuit 5.3

ξ	$(\omega CR)^2_{max}$	$(\omega CR)^2_{min}$	$[(\omega CR)^2_{min} / (\omega CR)^2_{max}] / \xi$	$Re[Z(\omega C)_{min}]/R$
.125	Only one root			
.1	68.60	19.40	2.83	71.22%
.05	351.67	26.33	1.50	85.59%
.01	9792.79	105.21	1.07	97.03%
.005	39592.90	205.10	1.04	98.51%
.001	997992.98	1005.02	1.01	99.70%

As can be seen in Table 7.1, the value of the real impedance corresponding to the minimum of the imaginary impedance approaches R as ξ decreases. Another result that also yields the value of R is the value of the real impedance when the imaginary impedance is at a local maximum approaches R/2 as ξ decreases. One additional result to note is the frequencies at which the local minimum and maximum occur. The square of ratio of the frequency at which the maximum occurs to the frequency at which the minimum occurs can be seen to approach ξ as ξ decreases, and is a good approximation to within 5% for values of ξ less than 1/100, shown in Table 7.1 above.

The quality of the minimum of equivalent circuit 5.3 is governed by ξ alone. Fig. 7.4 below illustrates a Nyquist plot of equivalent circuit 5.3 for varying values of ξ with a resistive element of 5000 Ω, which is a close order of magnitude approximation for the resistances seen in Figs. 7.1 through 7.3. There is no clear minimum present in Figs. 7.2 and 7.3, but the impedance spectroscopy responses of Fig. 7.1 can be fit to equivalent circuit 5.3 to yield a value of ξ. For Fig. 7.1, ξ equals 1/2050.The reduction in the quality of the minimum to the point that it disappears could be due to the decreased quality of the electrode-electrolyte interfaces or it could be suggestive of a more complicated response of the system than is encapsulated with equivalent circuit 5.3.

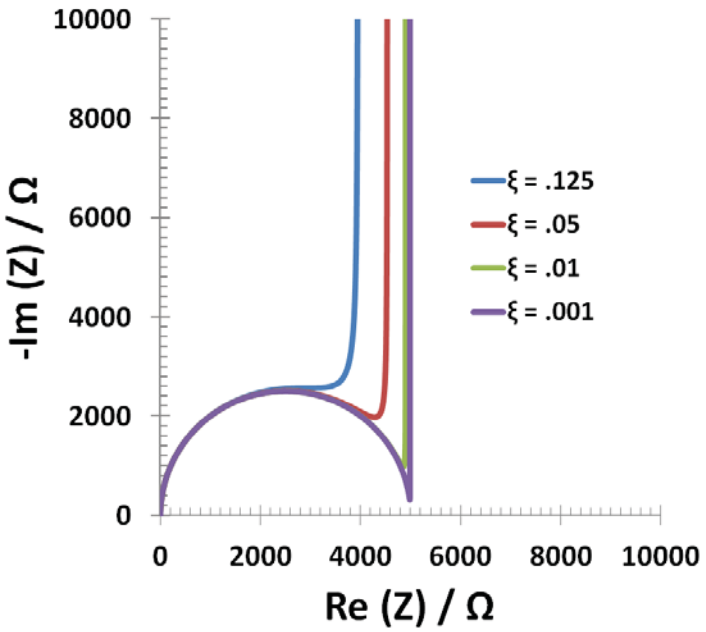

Figure 7.4: Nyquist plots of equivalent circuit 5.3 for varying values of ξ with R = 5000 Ω

The value of ξ from Fig. 7.1 would yield a deeper minimum, between the green and the purple curves of Fig. 7.4 above, than is seen in Fig 7.1. This suggests a more complicated equivalent circuit model is needed to explain the impedance spectroscopy responses of this solid electrolyte system as well, even if the low frequency tilting of the tail is ignored.

For equivalent circuits 5.4, 5.5 and 5.6, there can be up to 2 local minimum and two local maximum observed in the negative imaginary response to the complex impedance as well as the Nyquist plots. The presence of these local extrema is quite sensitive to the values of ξ_1 and ξ_2, and to a lesser extent R_2.

As an aside, one interesting feature of equivalent circuits 5.4, and 5.5, was in extending the solutions for ξ presented in Table 7.1 to these more complicated circuits. There was robustness in the relative location in frequency space of the extrema to large variations in the magnitudes of the circuit elements. These results were solved numerically. The relationship between ξ_1 and ξ_2 with the frequencies of the local extrema was not robust against changes in the magnitudes of the circuit elements for equivalent circuit 5.6. The ratio of ξ_1 to ξ_2 (which is also the ratio of the C_2 to C_1) was found to be equal to the square of ratio of ωC associated with the first minimum to ωC associated with the first maximum. This was found to be within 40% for most magnitudes of circuit elements, and most often was within 10%.

After trying to fit the impedance spectroscopy response of the solid electrolyte system shown in Fig. 7.1 with the two conduction channels of equivalent circuit 5.3, equivalent circuits 5.4 and 5.5 are now used and shown in Fig 7.5 below. The upturning of the low frequency tail in the responses shown in Figs. 7.2 and 7.3 could not be modeled with these equivalent circuits. Equivalent Circuit 5.6 proved to not be capable of modeling the response. Possibly

coincidentally, equivalent circuit 5.6 was also the one circuit with the least connection to a physical interpretation of its circuit elements.

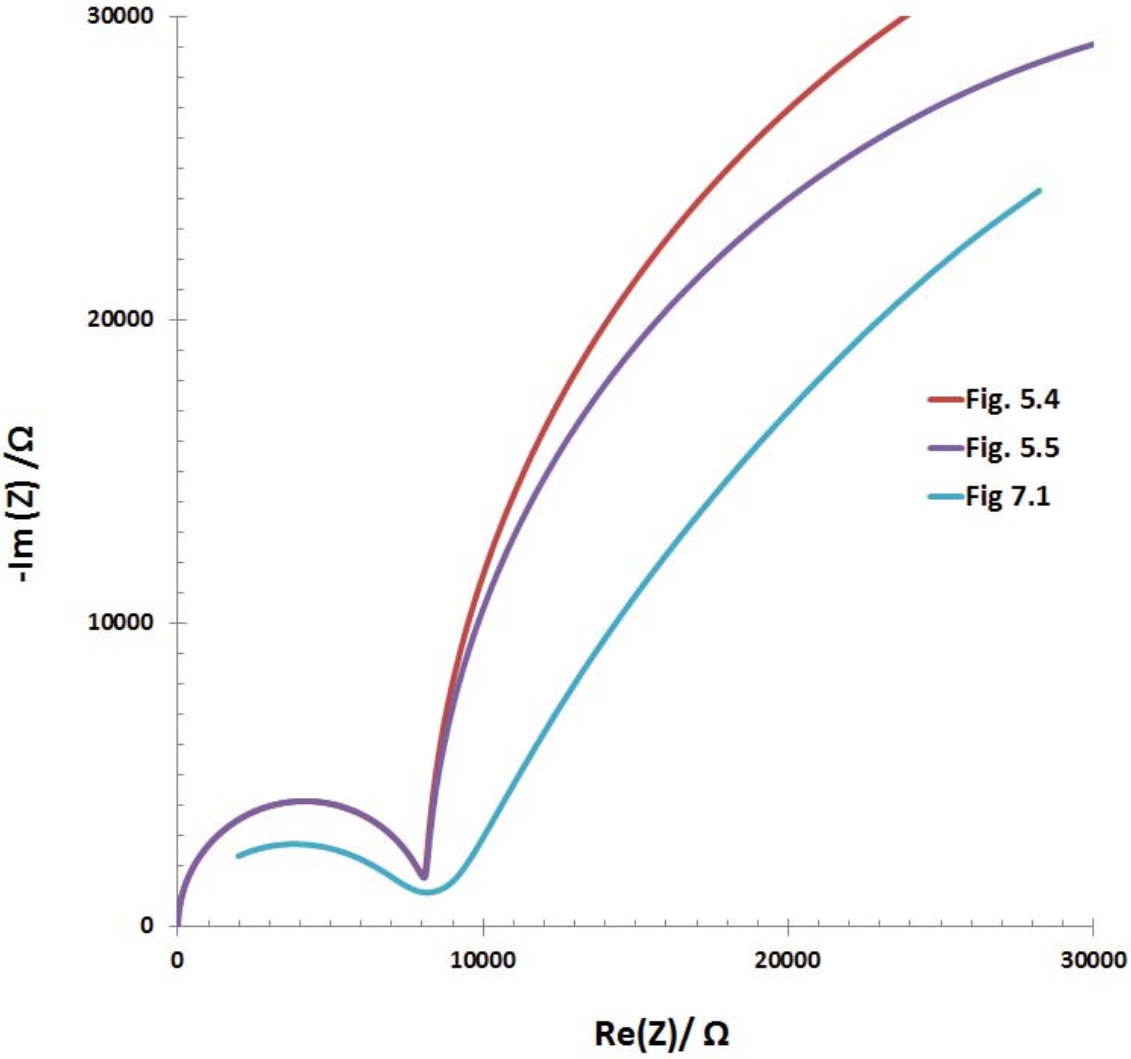

Figure 7.5: Nyquist plot of equivalent circuits 5.4, and 5.5 fitting the response of the solid electrolyte system shown in Fig. 7.1 with equivalent circuit 5.4 parameters of R = 8300 Ω, R_2 = 60000 Ω, ξ_1 = 0.001, and ξ_2 = 0.1 and equivalent circuit 5.5 parameters of R = 8300 Ω, R_2 = 60000 Ω, ξ_1 = 0.001, and ξ_2 = 0.1

As can be seen in Fig. 7.5 above, neither of the equivalent circuits are exact fits for the high frequency or the low frequency curves in the response of Fig. 7.1, but they do fit some aspects of the response with the same circuit elements. The magnitude of the imaginary impedance of the response of Fig. 7.1 is depressed about 30% to 50% from the fits of the equivalent circuits. The implications of this is in regards to the accuracy of the models is unknown. The sample in Fig. 7.1 was made with 10% excess lithium and there could have been a contaminate film present.

The five conduction channel equivalent circuit originally proposed to model supercapacitor systems by Conway and Miller was then fit with the response of Figs 7.2a and 7.3a. The AC impedance spectroscopy response of Fig. 7.2a has the same features as Fig. 7.3a, as evidenced by Fig. 7.3b. Many different circuit element parameters could be used to get varying degrees of fit, but the one constant feature was that the high frequency channel resistance, R_2, was approximately 5800 Ω for Fig 7.2a and 2200 Ω for Fig 7.3a.

By adding in the additional conduction channels of equivalent circuit 5.12, the responses of the solid electrolyte system from Figs. 7.1 through 7.3 can now be matched with an equivalent circuit, which is expected. This is akin to better fits from a polynomial by going to higher orders, and represents nothing unexpected.

7.4 Ionic Conductivity and Activation Energy

From the fits of the models above, the bulk ionic resistance term, R, can be estimated to be approximately the same value, regardless of the different models chosen. That value for the resistance is 8300 Ω for fig. 7.1, and despite the lack of clear minimums it is estimated to be 5800 Ω for Fig. 7.2 and 2200 Ω for Fig. 7.3. Using equation 5.4, these values for the bulk ionic resistance yield ionic conductivities of $1.6x10^{-5}$ S/cm at 20C for 10% excess lithium samples corrected for density, and $2.2x10^{-5}$ S/cm at 22C and $7.1x10^{-5}$ S/cm 75C for 8% excess lithium samples corrected for density. Again, note that the correct model to use cannot conclusively be identified from the impedance spectroscopy responses in Figs. 7.1 to 7.3, though as would be expected, the equivalent circuit with the most conduction pathways provides the better fit.

The ionic conductivities calculated for the 8% excess lithium samples, corrected for density, yielded an activation energy of 0.20 eV using equation 5.6 and an activation energy of 0.22 eV using equation 5.11. Both results are presented because the current literature appears equally divided on the correct form of applying an Arrhenius fit to the temperature dependence of the ionic conductivity.

7.5 In-situ Nanoscale Ionic Transport Results

The process for the in-situ measurements was the same as that detailed in Chapter 5 and in prior literature.[20] The bias was adjusted in increasing increments until current was detected with negative 7 volts of applied bias on the conductive tip . Additionally, the applied frequency was adjusted higher from 1/10 Hz to 1 Hz, where no current was detected. Systemic probing of the exact frequency of particle nucleation proved problematic due to the large voids on the surface of the poly-crystalline samples, which shortened the useful lifetime of the tips. This is in contrast with the smooth amorphous samples used in prior measurements.[20-22,55,56]

The applied waveform that generated particles is shown below in Fig. 7.11. This waveform approximates a triangular waveform with 256 DC steps, each of 40ms length for a period of 10.24 seconds. Note that the waveform starts with a negative bias, which would correspond to reduction of lithium on the surface if a particle is generated.

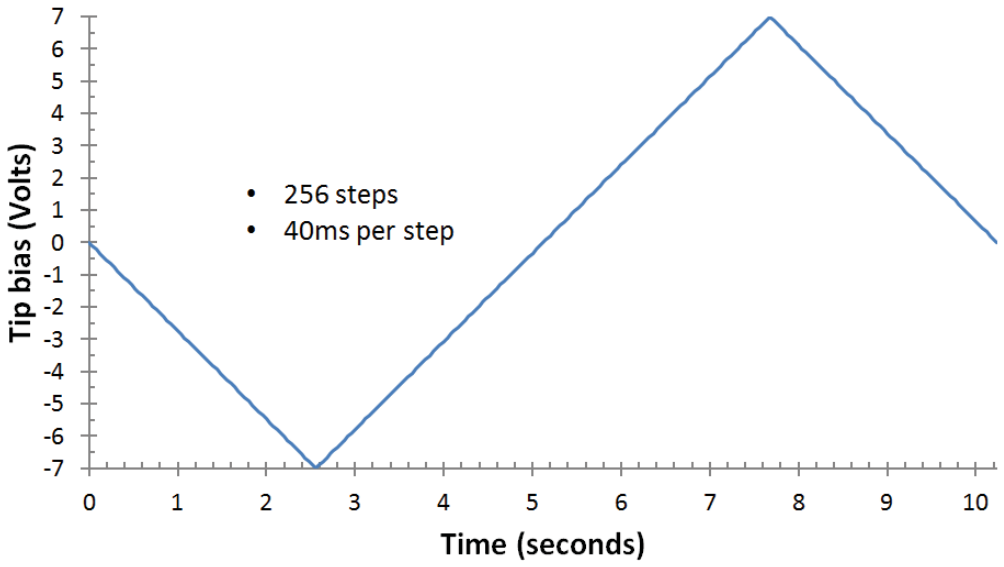

Figure 7.6: Applied waveform required for the formation of particles on the surface of pellet 210-07

The waveform shown in Fig. 7.6 was applied to each point of a 4x4 square grid, with 3 µm spacing between rows and columns. Fig. 7.7 below shows a topographical scan before and after the particles were formed. Note that 12 visible particles were formed in Fig. 7.7b. For later reference, the particles will be identified with coordinates x, y with the particle located at x = 2 µm and y = 17 µm being labeled particle 1,1. Moving to the right in the horizontal, x, direction to the next particle, will be particle 2,1, moving down in the vertical, y, direction will index the second coordinate.

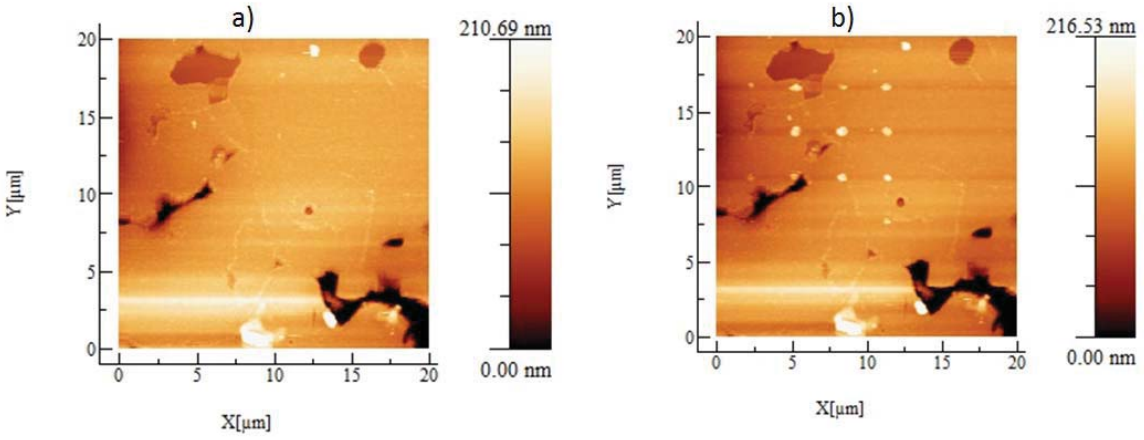

Figure 7.7: a) topographical scan before the particles were formed **b)** topographical scan after particles were formed on pellet 210-07

At each of the 16 points where the waveform was applied to bias the conductive tip, the tip height and the current collected were measured as a function of the step number, from 1 to 256. The tip height and the current were recorded twice at each step at averaged. Fig. 7.8 below displays the tip height versus step number for each of the 16 points for that area of pellet 210-07.

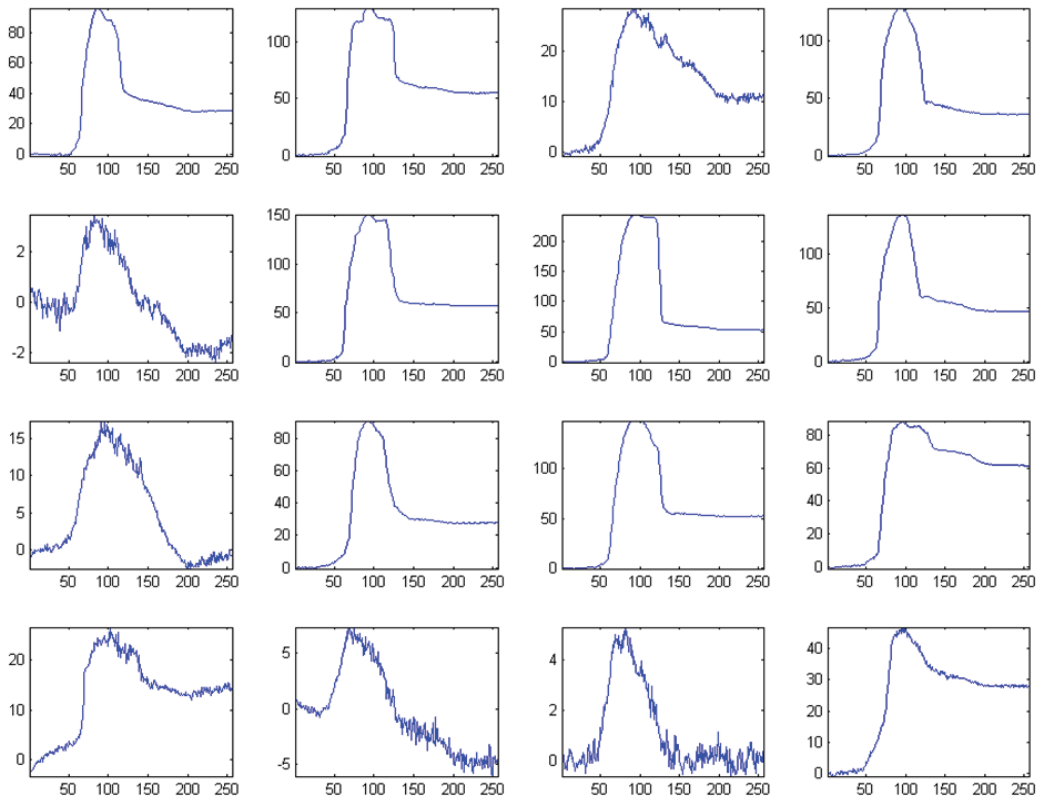

Figure 7.8: Tip height (nanometers) versus step number for the 4x4 particle formation experiment on pellet 210-07

Note that in Fig 7.8, as the polarity of the biased tip changes to positive, the tip height decreases. This is interpreted as lithium returning to the sample. Also note that point 1,2, point 2,4, and point 3,4 did not show any noticeable change in tip height beyond the periodic systemic noise present for these measurements. Point 1,4 did show an appreciable change in tip height, though it was located within a void resulting from grain pull-out during the polishing steps of sample preparation. Unfortunately, the topography of this location did not allow for accurate before and after topographical measurements of the surface, and this particle is not included in future analysis.

In addition to the change in tip height, the current was also collected at each of the 16 points, and is shown in Fig. 7.9 below.

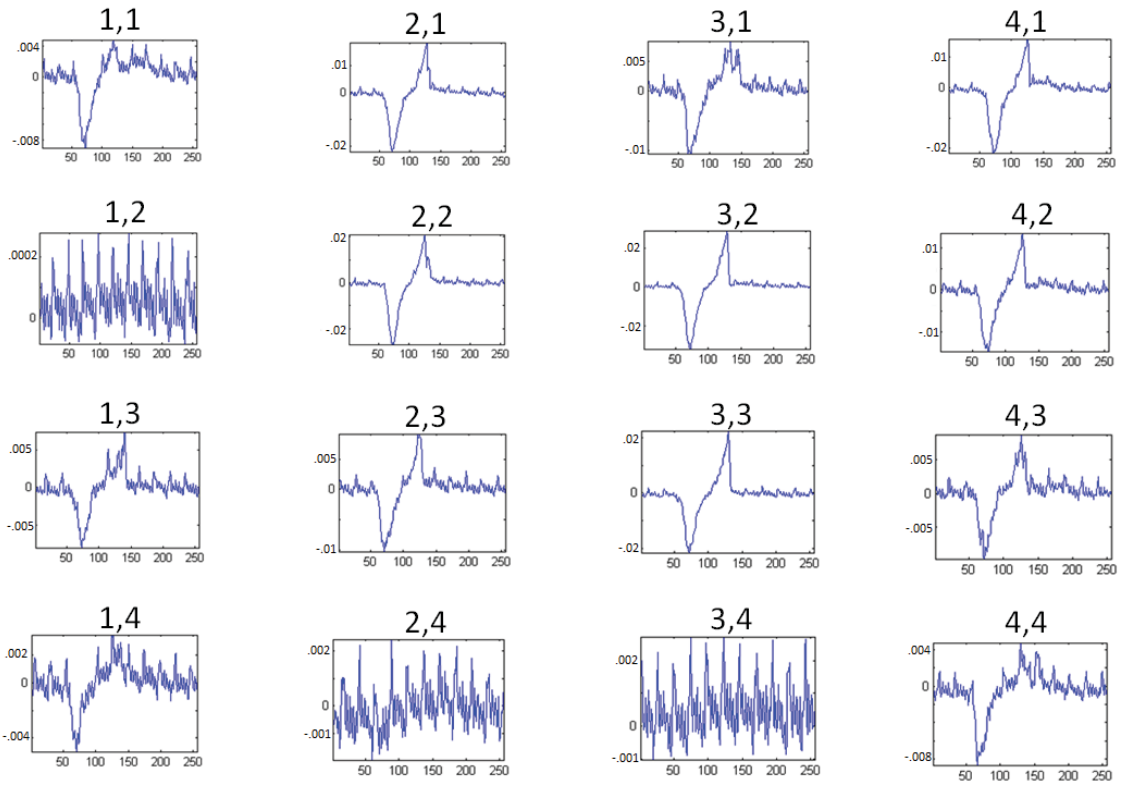

Figure 7.9: Current (10^{-8} amps) versus step number for the 4x4 particle formation experiment on pellet 210-07

Note the strong correlation with current collected, tip height change, and visible particles between Figs. 7.7 through 7.9, and that Fig 7.9 shows a current for particle 1,3 in agreement with Fig7.8, but again, due to its location, this particle is not included in future analysis.

Thirteen of the sixteen locations produced particles on the surface, which is approximately the same rate of particle formation in prior experiments.[20-22,55,56] Of the twelve that will be analyzed, they all are of approximately the same order of magnitude of current associated with each particle, between 8 and 20 nanoamps. The twelve particles showed a wider dispersion in tip height, ranging from 15 nm to 230 nm. This is attributed to the singular point location of the tip, with the three dimension particle possibly forming around the tip as well as under the tip. Additionally, the soft lithium may have allowed the tip to push into it. A better assessment of the particle's size is its three dimensional volume, shown in Fig. 7.10 below. The method for calculating the volume was to take the remainder of a particle after an area of size 2 µm by 2 µm surrounding the particle was flooded to a height such that only one island remained, the remainder of the particle. The height required to flood the topographical scan such that only one island remained versus the average height of an area 1 µm from the peak of the particle was then calculated. That difference in height multiplied with the area of the island that remained when the topographical scan was flooded yielded a good approximation of the

remaining volume of the particle. Any method of calculating the volume of the particles is assumed to have errors due to the soft nature of lithium and the inaccuracies associated with mapping it on the nanoscale.

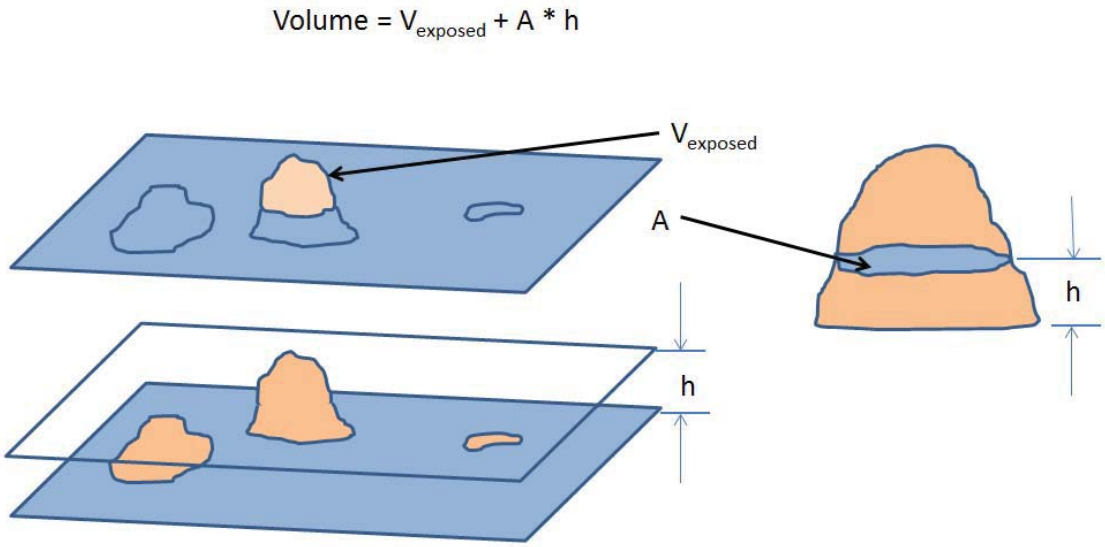

Figure 7.10: Schematic of calculating the volume of a particle on the surface of a sample after lithium particles were formed

The volumes of all twelve particles were calculated in this manner. Additionally, the current of each of the 12 particles was integrated to yield a total amount of charge transferred for each particle. If each particle were lithium, the volume can be associated with a number of lithium atoms. Fig. 7.11 below correlates the number of atoms in each particle, assuming the particle is metallic lithium, with the amount of charge transferred for each of the 12 particles being analyzed.

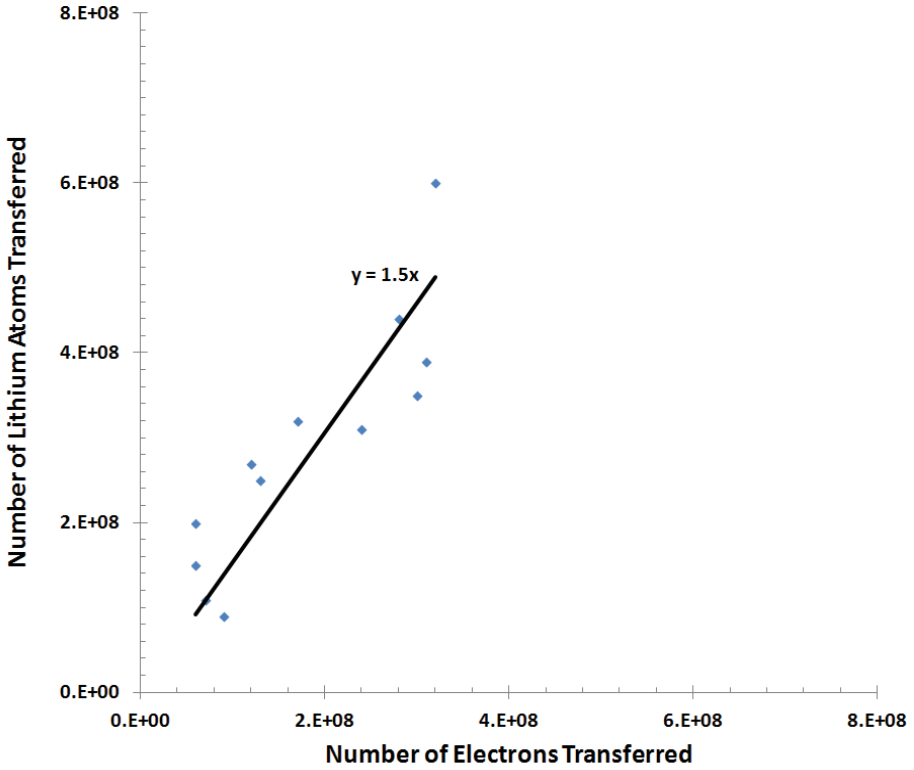

Figure 7.11: Correlation of the number of lithium atoms in a particle with the associated charge transferred for that particle for the 12 particles being analyzed on pellet 210-07

One additional calculation that can be made from these in-situ nanoscale ionic transport results is the distance of a particle from a grain boundary and the amount of charge transfer associated with that particle. To do so requires identifying the grain boundaries of the particle. This was done by using the noting the smoothness of an individual grain, with reported RMS roughness of approximately 2 nm. Note, these values are not accurate, as the radius of the tips used was nominally 20 nm. These values did demonstrate the smoothness of the sample though, to within the limits of the tip, and steps in the surface topography could be resolved with the higher resolution inherent in AFM. These steps, usually about 3 nm, were associated with grain boundaries. The shortest distance from the center of a particle to an identified grain boundary, as well as the volume and charge transfer associated with that particle, are noted in Table 7.2 below. The distance is provided in increments of 1.0 µm due to some noise in the topography scans at the nanometer scale than made precise location of the grain boundaries difficult.

Table 7.2: Volume, number of corresponding lithium atoms, total charged transferred and distance from grain boundary for the 12 particles being analyzed on pellet 210-07

particle	Distance to nearest grain boundary (μm)	Volume of particle ($x10^6$ nm^3)	# of Electrons Transferred ($x10^8$)
1,1	1.1	1.9	0.9
1,3	0.6	3.2	0.6
2,1	0.2	6.8	2.4
2,2	0.8	8.6	3.1
2,3	0.2	5.9	1.2
3,1	1.2	5.5	1.3
3,2	0.4	13.3	3.2
3,3	0.7	9.7	2.8
4,1	0.7	7.6	3.0
4,2	0.5	7.0	1.7
4,3	2.2	4.3	0.6
4,4	2.1	2.5	0.7

7.6 Summary of Results

AC impedance spectroscopy results were presented for typical samples, prepared as outlined in Chapter 6, and measured at room temperature and elevated temperatures. These results showed a decrease in the magnitude of the impedance as the temperature increased. Additionally, samples with 8% excess lithium showed a poor minimum, to the point that one was not apparent, as well as sharp upturn of the impedance spectroscopy response at low frequencies. The poor quality of the minimum may be the result of the contaminate film identified in Chapter 6, which the organic solvent used for the gold electrodes as well as the elevated temperature to cure the electrodes may have introduced, so it cannot be ruled out. Conversely, another explanation for the lack of the minimum in the context of equivalent circuit 5.12, is that there is now a better electrode-electrolyte interface without the contaminate film, and the surface effects akin to the multi-pore model play a larger role. The rationale for this is that the multi-pore model with the additional conduction channels that modeled high degrees of the electrode-electrolyte interfacial effects was the only model that could closely fit the impedance spectroscopy results. Other literature have pointed to the simpler models and then claimed other low frequency effects such as diffusion. [5,6,9,51]

Analytical and numerical solutions are presented for equivalent circuit 5.3. A means of determining the ratios of capacitive elements in the equivalent circuits is presented that is only dependent on the frequency at which a local extremum occurs, independent of the magnitudes of the resistive or capacitive elements in the circuits. This concept is extended to the equivalent circuits 5.4 and 5.5.

The ionic conductivity was found to be $1.6x10^{-5}$ S/cm at 20C for samples made with 10% excess lithium corrected for density, $2.2x10^{-5}$ S/cm at 22C for samples made with 8% excess lithium

corrected for density, and $7.1x10^{-5}$ S/cm at 75C for 8% excess lithium samples corrected for density. The activation energy associated with the temperature dependence of the ionic conductivity was found to be 0.20 eV if the pre-exponential factor from the Arrhenius fit did not have any temperature dependence, as shown in equation 5.6, and 0.22 eV if the pre-exponential factor had a 1/T temperature dependence, as shown in equation 5.11.

In-situ lithium transport on the nanoscale was demonstrated. The results were achieved with a bias of 7 volts and a frequency of 1/10 Hz. The bias was higher than the threshold bias in prior results, shown in Fig 5.16, but the sample was between 450 and 500 microns thick, compared to the 150 micron LICGC sample used in Fig. 5.16. Additionally, grain boundary effects may also have hindered the uniform propagation of the electric field at depths sufficiently far from the tip.[20]

The threshold frequency for the nucleation of particles was shown to be between 1 Hz and 1/10 Hz for a triangular waveform, which is lower than the threshold required for prior work on LICGC, shown in Fig. 5.16. This is attributed to the thicker sample and potential grain boundary effects. Comparing these results with Fig 5.15 suggests an even lower threshold voltage for sinusoidal waveforms.[20-22,55,56]

The volume of the particles was correlated with the number of electrons transferred in Figure 7.11 to yield 1.5 lithium atoms per electron, which is in rough agreement with prior work on LICGC, shown in Fig. 5.19, and in prior literature. That coupled with the compositional characterization of particles on LICGC, shown in Fig. 5.20, and prior Raman spectroscopy results strongly suggests the composition of the particles is metallic lithium.[20-22,55,56]

Particles were created with similar applied conditions and of similar size, regardless of proximity to the grains, as shown in Table 7.2. Due to the large particle created at 3,2, and its relative proximity to a grain boundary, a plot of these particles versus distance from a grain boundary would show a weak correlation. Without that particle, there appears to be no correlation. There are not enough data points to draw a definitive link between particle size and proximity to the grain boundary. To draw any conclusions on these results, the physics of the model should be checked. If there were a significantly easier pathway for ionic conduction along the grain boundaries, then anomalously high currents and correspondingly large particles would have been expected at the grain boundaries. A few particles grew to the point of overlapping a grain boundary, but no anomalous current was detected. This lack of anomalous current readings suggests there is not a significantly easier conduction pathway for lithium along the grains, and supports the assumption used to generate equivalent circuit 5.4.

The low threshold frequency for particle nucleation with a triangular waveform, and thus even lower assumed threshold frequency with a sinusoidal waveform, coupled with the relatively high electric fields present in the samples near the biased tip, shown in Fig. 5.17, versus the low electric fields of 1kV/m (100mV uniformly spread across a 300 micron thick sample) in AC impedance spectroscopy measurements, presents some evidence against Warburg Diffusion

occurring at sinusoidal frequencies still above 1 Hz and the low applied biases of 50mV or 100 mV typically used in AC impedance spectroscopy of solid electrolyte systems.[20-22,55,56]

8.0 Closing Remarks

8.1 Conclusions

A new synthesis route was shown, with similar results to other recent findings, though different synthesis conditions were used.[23,24] The higher densities achieved, up to 96% of theoretical, yielded samples with a room temperature ionic conductivity of $2x10^{-5}$ S/cm and an activation energy of 0.20 eV or 0.22 eV, depending on the pre-exponential factor in the Arrhenius fit used. The original Arrhenius equation was used to determine the temperature dependence of chemical reaction rates. Therefore, it can be viewed as traditionally being applied to single events occurring, and in that context has proven its versatility. This line of thought would then apply the Arrhenius fit for the individual action of the jump rate for ionic hopping presented in equation 5.9. Following that logic would lend more credence to equation 5.11 for the activation energy of the ionic conductivity, which is a macro scale phenomena, comprised of many individual events that each obey the Arrhenius fit.

The room temperature ionic conductivity was slightly higher and the activation energy was lower than what was reported in initial findings for this material, but follows the trend of higher room temperature ionic conductivity and lower activation energy for denser samples reported recently.

The notion of Warburg Diffusion occurring at lower frequencies that are still above 1 Hz and with a low applied bias is challenged based on the findings of in-situ nanoscale transport measurements.[20-22,55,56] There is difficulty directly correlating the biases from the in-situ nanoscale measurements with biases applied to macroscopic samples in AC impedance spectroscopy. The assumption that grain boundaries do not provide a significantly easier pathway for ionic conductivity is supported, but not definitively confirmed, with in-situ nanoscale transport measurements.

A solution to the two conduction channel model for solid electrolytes without grain boundary resistance is presented, with the introduced parameter of ξ and a way to experimentally probe its value by noting the frequencies at which the extremum in the response to AC impedance spectroscopy occur. The experimental determination of ξ is independent of the magnitudes of the capacitive and resistive elements in the circuit, and only has experimental dependence on the square of the ratio of two frequencies. The extension of ξ to more complicated circuits is solved numerically, with strong evidence for its experimental determination presented. This new parameter will allow the impedance spectroscopy responses to be checked against the physics of the equivalent circuit chosen and should allow for rough order of magnitude approximations for the capacitive elements in the equivalent circuits chosen without the need for the circuit simulation software that is commonly used. Doing so would allow for more contact between the impedance spectroscopy response and the physics used to construct the equivalent circuits.

Additional equivalent circuits are introduced and proposed as potential models for the response of a solid electrolyte system to AC impedance spectroscopy. The features of the impedance spectroscopy responses of solid electrolyte systems that have been attributed to grain boundary effects can be reproduced with models that have also successfully mimicked the response of supercapacitors and are interpreted within in the context of the multi-pore model.

The features of the impedance spectroscopy responses commonly associated with bulk ionic resistance could likewise be interpreted as only the mid to high frequency ionic resistance, where the ions do not travel all the way to the electrode-electrolyte boundary. The operational environment for batteries, even at high charging and discharging rates of 10C or 20C, is practically the DC limit. Operationally, the ions must fully traverse the electrolyte and enter and leave the electrodes. The resistance that should be associated with the ionic conductivity of an operational solid electrolyte in a battery should be the resistance encountered near the DC limit. However, if the increase in lower frequency impedance is due to surface effects akin to the multi-pore model, the lower frequency impedances are sample specific and do not accurately reflect the intrinsic bulk ionic conductivity of the solid electrolyte being tested. The net result of this is to bring into question the need to accurately measure the intrinsic ionic conductivity of a solid electrolyte when the surface effects may play the largest role in the operational ionic conductivity while simultaneously questioning the bulk ionic conductivity measurements made using impedance spectroscopy.

The solid-solid interfaces of the electrodes with the solid electrolyte is believed to have an effect on the impedance spectroscopy response of the system and it is proposed here that it may also account for lower frequency features of the responses of solid electrolyte systems within the context of the multi-pore models. Similar features in impedance spectroscopy responses have previously been associated with grain boundary effects from poly-crystalline samples.[5-11] Therefore, it cannot conclusively be determined from the impedance spectroscopy alone what the bulk and what the grain boundary resistance of a sample is. However, the intrinsic material properties should not depend on extrinsic effects like grain boundaries.

A contaminant film was observed on the surface of some samples which was determined to be Li_2CO_3. This film was associated with samples made with 10% excess lithium, similar to previous studies. This film was not observed in samples with 8% excess lithium. The role this film plays in the impedance spectroscopy responses of the systems tested here is suspected to an increase in the overall resistance, as evidenced by the higher magnitudes of impedance on Fig. 7.1 versus Fig 7.2. The amount of film present was below the threshold to be seen on XRD studies, and it is believed it may be present in other studies. The source of the carbon for the contaminant is speculated to be either ambient CO_2 or the organic solvents used in polishing and applying the gold electrodes.

8.2 Future Work

The challenges of incorporating a solid electrolyte into a complex electrochemical system are significant, and further characterization of the basic material properties of a solid electrolyte would be beneficial. In particular, more conclusive results could be beneficial for the intrinsic ionic conductivity of this class of materials which would be determined despite extrinsic effects like grain boundaries and the quality of the electrode-electrolyte interface. In order to futher characterize these materials, there are several areas where the work presented here could be continued and extended. Additionally, incorporating a solid electrolyte into a solid state battery introduces new challenges not addressed in this research that would also need to be studied.

One of the biggest challenges in this research was the low yield of the samples. This prevented many experiments from being repeated, as there were not enough samples. Another challenge was the limited lifetime of the samples. The useful range of a sample seemed to last for a month, sometimes two, but eventually, its impedance spectroscopy results would degrade. The exact mechanism for this was not investigated due to the limited resources available for these experiments. A possible cause would be the growth of Li_2CO_3 films between the gold electrodes and the samples or the potential growth of this film at between the grains. This Li_2CO_3film was found to be a contaminant on some samples and identified with XPS. The characteristic optical dispersion of light, as well as sub-micron features on the surface, that were noticed on the sample that were identified as having this film were also seen on other samples. This happened regardless of storing some samples in an oven at 120C to minimize the effects of moisture as well as others being stored at ambient conditions.

If more samples were available, these impedance spectroscopy results should be repeated, as well as carried out at lower frequencies. Unfortunately, the importance of the lower frequency results was not recognized, as initially the assumption was made that Warburg Diffusion was occurring and the initial goal was to probe the grain boundary contribution to ionic conductivity. The impedance spectroscopy responses were only run to get into that lower frequency regime, not to test its limits and validity. The conclusion that Warburg Diffusion does not play a significant role in the low frequency response of the system goes counter to other published results. To reinforce the claims made here, further investigations are warranted.

Additionally, if more samples were available, then the potential for characterizing the mechanical properties could be analyzed. The mechanical properties of this class of material are lacking in the published literature, and would play an important role in choosing a suitable solid electrolyte to use in a solid state battery. There are many different solid electrolytes being investigated with differences in their reported ionic conductivity spanning several orders of magnitude. Obviously ones with better ionic conductivity would be ideal, but that would need to be weighed against material costs, mechanical properties, chemical compatibility, and manufacturability. In the limit where the solid electrolyte is shrunk down to several microns in thickness, or possibly even less, the ionic conductivity will not be the only critical material property. Mechanical properties of the material will play a significant role in choosing the ideal

solid electrolyte. If lithium metal is the anode, the solid electrolyte will need to be able to withstand repeated cycling and the lithium's propensity to form dendrites, which would try to pierce the solid electrolyte. A trade-off between high ionic conductivity and suitable mechanical properties will be required and informed decisions in this regard will require a better understanding of these materials' mechanical properties.

Another area that warrants further investigation is controlling the grain size of the samples, which was the initial aim of this research. The initial attempts to control the grain size as a function of sintering conditions did not yield quality samples with grain sizes that differed significantly beyond approximately 4 microns. This synthesis work was extensive, continuing for almost three years, but by no means exhaustive. More resources and researchers could potentially find other synthesis routes to yield high enough quality ceramic samples with a wide enough dispersion of grain sizes to then try to characterize them and elucidate the grain boundary effects. This work would be very time and resource intensive. Synthesizing samples with a volatile element like lithium introduces many more variables into the synthesis process than traditional ceramic synthesis –with the history of the crucibles, amount of powder used to embed the pellets, and thickness of the pellets being just a few of these.

There is one potential way to investigate the grain boundary effects without going through the traditional ceramic synthesis routes. That would be to investigate the system in the limit of no grain boundaries, with single crystals grown epitaxially. High enough quality ceramic targets can be made using the synthesis route outlined in this research which could then be used to grow thin film crystals with modern deposition techniques, such as pulsed laser deposition. The cubic unit cell distance of 12.8 angstroms would be challenging to match, but substrates near 3.2 or 4.3 angstroms could suffice. A conductive, but ionically blocking, substrate would be ideal, as it would allow for the same 2-probe experimental setup used in AC impedance spectroscopy in this research. Traditional 4-probe measurements would also be warranted if such samples were grown. An intriguing extension of the 4-probe measurement would be in an inert environment where the potential exists for a 4-probe DC conductivity study with lithium electrodes for the current probes and ionically blocking electrodes for the voltage probes.

If samples are grown using modern deposition techniques, then it opens up additional areas of research with this class of materials. It has been theorized, using results from density functional theory, and seen experimentally, by using substitutions, that the ionic conductivity of these samples is significantly influenced by the atomic spacing. Different substrates could introduce different amounts of strain into these samples, and the effects of atomic spacing could be investigated on identical compositions. Another area of research that thin film crystals would facilitate would be in testing full electrochemical cells by growing this solid electrolyte on suitable substrates that could function as a working electrode. The other side of the solid electrolyte could then be coated with any suitable conductor that could function as a current collector. If the substrate/electrode is in a lithium rich phase, the cell could be cycled to extract bulk lithium metal onto the surface of the solid electrolyte, below the current collector. Cyclic voltammetry studies could then be performed.

Another area that warrants future consideration is testing this class of lithium ionic conducting solid electrolytes, as well as other lithium ionic conductors, at or near the DC limit. These experiments would be similar to the initial work on ionic conductivity carried out in the early twentieth century, and detailed in chapter 4. The benefits of probing these materials at the DC limit should make the challenges of working with lithium electrodes worthwhile. One of the main motivations for this work would be in correlating the ionic conductivity from this method with that determined from equating features in the impedance spectroscopy with the different equivalent circuit models. There is an ambiguity in determining if the features being seen can be associated with the complex electrode-electrolyte interface akin to the multi-pore models or from grain boundary effects that was shown in this research. DC conductivity studies would provide a means to determine which features in the impedance spectroscopy responses best represent the DC ionic conductivity of these materials. The DC ionic conductivity is the property which best determines how these materials would behave in typical battery operations. These tests could be done at higher voltages than the small biases used in impedance spectroscopy, which is another area where this form of testing would come closer to matching the operating conditions of an operational battery. Ideally, these, these experiments would be performed on single crystals to eliminate the effects of grain boundaries.

A final area of where this research could continue is in optimizing the solid electrolyte in regards to large-scale manufacturing of solid state rechargeable lithium batteries, but more research into the properties of the garnet class of solid electrolytes as well as other classes of solid electrolytes needs to be done before that is considered. Once one or a few candidate solid electrolytes are chosen, then research into co-fired ceramics might prove fruitful. The cathode would be cast as a thick film from a slurry and then a solid electrolyte slurry would be applied as a thin film, possibly with screen printing techniques. Additives to control the sintering profiles of both materials would be required to match the densification of both ceramics. The role these additives play in the structure, transport, mechanical properties, and chemical properties of the materials is important, and would require extensive research to optimize.

The research presented here in interpreting the impedance spectroscopy responses of solid electrolytes will assist in analyzing the transport properties of solid electrolytes. The study of lithium transport through solids is a challenging field, but one whose potential applications are significant. It is hoped that the work presented here facilitates our understanding of the ionic transport of lithium through solids and will prove useful as research in this area undoubtedly continues.

References

***translated, summarized, and/or copied sections of the original text were accessed and referenced, but not the original paper in its entirety**

1. Scrosati B, Garche J, Lithium Batteries: Status, Prospects, and Future, Journal of Power Sources, 2010, Volume 195 (9), pages 2419-2430
2. Brodd R, Bullock K, et.al., Batteries, 1977 to 2002, Journal of the Electrochemical Society, 2004, Volume 151 (3) pages K1-K11
3. Thackeray M, Wolverton C, et.al., Electrical Energy Storage for Transportation – Approaching the Limits of, and Going Beyond Lithium-Ion Batteries, Energy and Environmental Science, 2012, Volume 5 (7) pages 7854-8763
4. Winter M, Brodd R, What are Batteries, Fuel Cells, and Supercapacitors*?, Chemical Reviews,* 2004, Volume 104 (10), pages 4245–427
5. Thangdurai V, Kaack H, et.al., "Novel Fast Lithium Ion Conduction in Garnet-Type $Li_5La_3M_2O_{12}$ (M=Nb, Ta)", Journal of the American Ceramic Society, 2003, Volume 86 (3), pages 437-440
6. Murugan, R, Ramakumar S, et.al., High Conductive Yttrium Doped Li7La3Zr2O12 Cubic Lithium Garnet, Lectrochemistry Communications, 2011, Volume 13 (12), pages 1373-1375
7. Li Y, Han J, et.al., Optimizing the Li+ Conductivity in a Garnet Framework, Journal of Materials Chemistry, 2012, volume 22 (30), pages 15357-15361
8. Gupta A, Murugan r, et.al., Optimum Lithium-ion Conductivity in Cubic Li7-xLa3Hf2-xTaxO12, Journalof Power Sources, 2012, Volume 209, pages 184-188
9. Murugan R, Thangdurai V, et.al., Lithium ion conductivity of Li5+xBaxLa3-xTa2O12 (x=0-2) with Garnet-Related Structure in Dependence of the Barium content, Ionics, 2007, volume 13 94), pages 195-203
10. Ohta S, Kobayashi t, et.al., High Lithium ionic Conductivity in the Garnet-Type Oxide Li7-xLa3(Zr2-x, Nbx)O12 (x=0-2), Journal of Power Sources, 2011, volume 196 (6), pages 3342-3345
11. Deviannapoorani, Dhivya, et.al., "Lithium Ion Transport Properties of High Conductive Tellurium Substituted $Li_7La_3Zr_2O_{12}$ Cubic Lithium Garnets", Journal of Power Sources, 2013, Volume 240, pp 18-25
12. Bauerle J, Study of Solid Electrolyte Polarization by a Complex Admittance Method, Journal of Physics and Chemistry of Solids, volume 30 (12) December 1969, pages 2657-2670
13. Barsoukov E, Macdonald R, et al., Impedance Spectroscopy: Theory, Experiment and Applications, John Wiley and Sons, 2005, ISBN 0-471-64749-7, pages 80-128, 238-263
14. Orazem M and Tribollet B, Electrochemical Impedance Spectroscopy, John Wiley and Sons, 2008, ISBN 978-0-470-04140-6, pages 68-95, 183-235, 309-348
15. *Raleigh D, Polarization Capacitance in Ionic Solids, Physica Status A, 1971, Volume 4 (1), pages 215+

16. Conway, B, Electrochemical Supercapacitors: Scientific Fundamentals and Technological Applications, Kluwer Academic/Plenum Publisher, 1999, ISBN 0-306-45736-9, pages 105-114, 479-556
17. *Miller J, Second International Symposium on electrochemical Capacitors and Similar Energy Storage Devices, 1992, Florida Educational Seminars, Boca Raton FL
18. Zubieta L, Bonert R, Characterization of Double-Layer Capacitors for Power Electronics Applications, IEEE Transactions on Industry Applications, 2000, Volume 36 (1), pages 199-205
19. New D, Double Layer Capacitors: Automotive Applications and Modeling, Master of Science Thesis for Massachusetts Institute of Technology, 2004, pages 53-92
20. Arruda T, Kumar A, et.al., The partially reversible formation of Li-metal particles on a Solid Li Electrolyte: applications Towards Nanobatteries, Nanotechnology, 2012, Volume 23 (32) 325402
21. Arruda T, Kumar A, et.al., In-Situ Formation of Micron Scale Li Metal Anodes with High Cyclability, ECS Electrochemistry Letters, 2014, Volume 3 (1), pages A4-A7
22. Kumar A, Chen C, et.al., Frequency Spectroscopy of Irreversible Electrochemical Nucleation Kinetics on the Nanoscale, Nanoscale, 2013, volume 5 (23), pages 11964-11970
23. Li Y, Wang Z, et.al., Densification and Ionic-Conduction Improvement of Lithium Garnet Solid Electrolytes by Flowing Oxygen Sintering, Journal of Power Sources, 2014, Volume 248, pages 642-646
24. Allen J, Wolfenstine J, et.al., effect of substitution (Ta, Al, Ga) on the Conductivity of Li7La3Zr2O12, Journal of Power sources, volume 206, pages 315-319
25. Whittingham S, Lithium Batteries and Cathode Materials, Chemical Reviews, 2004, Volume 104, pages 4271-4301
26. Fergus J, Ceramic and Polymeric Solid Electrolytes for Lithium-Ion Batteries, Journal of Power Sources, 2010, volume 195, pages 4554-4569
27. Ayrbach D, Zinigrad E, et.al., A short Review of Failure Mechanisms of Lithium Metal and Lithiated Graphite Anodes in Liquid Electrolyte Solutions, Solid State Ionics, 2002, Volume 148(3-4), pages 405-416
28. Xu W, Wang J, et.al., Lithium Metal Anodes for Rechargeable Batteries, Energy and Environmental Science, 2014, Volume 7 (2), pages 513-537
29. Cussen E, Structure and Ionic Conductivity in Lithium Garnets, Journal of Materials Chemistry, 2010, Volume 20, pages 5167-5173
30. Kamaya N, Homma K, et.al., A Lithium Superionic Conductor, Nature Materials, 2011, Volume 10, pages 682-686
31. Tatsumisago M, Nagao M, et.al., Recent Development of Sulfide Solid Electrolytes and Interfacial Modification for All-Solid-State Rechargeable Batteries, Journal of Asian Ceramic Societies, 2013, Volume 1(1), pages 17-25
32. Takada K, Ohta N, et.al., Interfacial Phenomena in solid-State Lithium Battery with Sulfide Solid Electrolyte, Sold State Ionics, 2012, volume 225, pages 594-597

33. Mazza D, Remarks on a ternary Phase in the La2O3-Nb2O5-Li2O, La2)3-Ta2O5-Li2) System, Materials Letters, 1988, Volume 7 (5-6), pages 205-207
34. Thangdurai V, Weppner W, Li(6)ALa(2)Ta(2)O(12) (A=Sr,Ba): Novel Garnet-Like Oxides for Fast Lithium Conduction, Advanced Functional Materials, 2005, Volume 15 (1), pages 107-112
35. Awaka J, Kijma N, et.al., Synthesis and Structure Analysis of Tetragonal Li7La3Zr2O12 with the Garnet-Related Type Structure, Journal of Solid Satte Chemistry, 2009, Volume 182 (8), pages 2046-2052
36. Xu M, Park M, et.al., Mechanisms of Li+ Transport in Garnet-Type Cubic Li3+xLa3M2O12 (M=Te, Nb, Zr), Physical Review B, 2012, Volume 85, 053201
37. Kumar P and Yashonath S, Ionic Conduction in the Solid State, *J. Chem. Sci.*, Vol. 118, No. 1, January 2006, pp. 135–154
38. *Faraday M , Philosophical Transactions Royal Society, London, 1838
39. Funke, K, Solid State Ionics: from Michael Faraday to green energy-the European dimension, Science and Technology of Advanced Materials, 2013, Volume 14
40. *Nernst W, Wild W, Some Points on the Behaviors of Electrolytic Mantles, Zeitschrift Fur Elektrochemie, 1900, volume 7, pages 373-376
41. *C. Tubandt, Electricity Conduction in Solid Crystalized Compounds, Zeitschrift Fur Anorganische Und Allgemeine Chemie, 1920, Volume 110 (3) pages 196-236
42. Read P, Katz E, Ionic Hall Effect in Sodium Chloride, 1960, Physical Review Letters, Volume 5(10), pages 466-468
43. Kaneda T, Mizuki E, Hall Effect of Silver ions in RbAg4I5 Single Crystals, Physical Review Letters, 1972, Volume 29 (14) pages 937-939
44. *Newman D, Frank C, et.al., The Ionic Hall Effect in solid Electrolyte C5H6NAg5I6, Electrochemical Acta, 1977, Volume 22 (8), pages 811-814
45. Clement V, Ravaine D, et.al., Measurement of Hall Mobilities in AgPO3-AgI Glasses, Solid State Ionics, 1988, Volume 28-30, pages 1572-1578
46. Kiukkola K, Wagner C, Measurements on Galvanic Cells Involving Solid Electrolytes, Journal of the Electrochemical Society, 1957, Volume 104(6) pages 379-387
47. Hebb M, Electrical Conductivity of Silver Sulfide, Journal of Chemical Physics, 1952, Volume 20(1) pages 185-190
48. Ure R, Ionic Conductivity of Calcium Fluoride Crystals, The Journal of Chemical Physics, 1957, Volume 26 (6) pages 1363-1374
49. Lynch D, Diffusion and Ionic Conductivity in Cesium Bromide and Cesium Iodide, Physical Review, 1960, Volume 118 (2) pages 468-473
50. Mrguhdich J, Conductivity of Silver Iodide Pellets for Solid-Electrolyte Batteries, Journal of the Electrochemical Society, 1960, Volume 107 (6) pages 475-479
51. Huggins R, Simple Method to Determine Electronic and Ionic Components of the Conductivity in Mixed Conductors: A Review, Ionics, 2002, Volume 8, pages 300-313
52. Gabrielli C, Identification of Electrochemical Processes by Frequency Response Analysis, Solartron Anaytical Technical Report Number 004/83, 1998, pages 1-14

53. Brug G, Vandeneeden A, et.al., The Analysis of Electrode Impedances Complicated by the Presence of a Constant Phase Element, Journal of Electroanalytical Chemistry, 1984, Volume 176 (1-2), pages 275-295
54. *Jacquelin, J, A number of models for CPA impedances of conductors and for relaxation in non-Debye dielectrics, Journal of Non-Crystalline Solids, 1991, Volumes 131-133 (2), pages 1080-1083
55. Arruda T, Kumar A, et.al., Supplementary Material for The Partially Reversible Formation of Li-metal Particles on a Solid Electrolyte: Applications Towards NanoBatteries, Nanotechnology, 2012, Volume 23 325402
56. Kumar A, Arruda T, et.al., Nanometer-scale mapping of irreversible electrochemical nucleation processes on solid Li-ion electrolytes, Scientific Reports, 2013, volume 3, 1621
57. Marriappan C, Gnanasekar K, et.al., Lithium ion conduction in Li5La3Ta2O12 and Li7La3Ta2O12 garnet-type materials, journal of Electroceramics, 2013, Volume 30 (4) pages 258-265
58. Horcas I, Fernandez R, et.al. WxSM: A Software for Scanning Probe Microscopy and a Tool for Nanotechnology, Review Scientific Instruments, 2007, Volume 78, 013705
59. Jesse S, Maksymovych P, et.al., Rapid Multidimensional Data Acquisition in Scanning Probe Microscopy Applied to Local Polarization Dynamics and Voltage Dependent Contact Mechanics, Applied Physics Letters, 2008, volume 93 112903

Vita

Brian M. Ray

Education:

Johns Hopkins University

Master's Degree in Applied Physics

May, 2005

University of Florida

Bachelor's Degree in Mechanical Engineering

December, 2000

Professional Positions:

University of Kentucky

Lexington, KY

August, 2005 to May, 2013

Northrop Grumman

Baltimore, MD

March, 2001 to April, 2005